Numerical Study of Reservoir Geomechanical Pressuremeter Testing under Anisotropic In-situ Stresses

by

Lang Liu

A thesis submitted in partial fulfillment of the requirements for the degree of

Master of Science

In Geotechnical Engineering

Department of Civil and Environmental Engineering
University of Alberta

ABSTRACT

The anisotropy of horizontal stresses in the saturated medium presents tremendous difficulties to the determination of in-situ rock properties especially when the formation is poorly overconsolidated. The application of reservoir geomechanical pressuremeter designed to pressurize the borehole at considerable depth has been numerically assessed and has shown considerable promise for capturing the key in-situ geomechanical parameters. This research has two primary objectives: (1) to investigate the mechanical behavior of borehole during the sequence of drilling, relaxation, expansion and contraction in the testing pockets and (2) to develop an interpretation methodology to invert for horizontal anisotropy and other in-situ parameters from the downhole pressuremeter testing in soft rock.

The formation drainage condition was examined considering factors such as pressuremeter loading rate and formation permeability by evaluating both the excess pore pressure generation and void ratio variation within the formation. The finding shows that the cavity expansion in most soft sedimentary formations is very likely occurring under partially drained conditions and the in-situ permeability is only minimally affected by loading. Yielding, if any, which is triggered by drilling and developed in the relaxation, can soften the materials

and thus lead to a remarkable rise for both pore pressure and radial displacement if the borehole is subsequently expanded.

The possible stress regimes for the deep formations were analyzed based on the yielding criterion of Cam Clay model. The short term and long term borehole deformation and damages induced by drilling were both investigated. The time-dependent convergences were correlated with the initial horizontal stress anisotropies, which makes the inversion possible by matching the convergence rate in the chart of characteristic curve.

The influences of initial stress anisotropy and drilling-induced modulus heterogeneity on the resultant stress profile after expansion were discussed. The possible shear failure regions under different loading regimes were compared. It is necessary to extend the study into the relatively high permeability formation that exhibits the behavior of partial drainage to the outer boundary. The variation trend of excess pore pressure under such an environment was analyzed.

The pressuremeter membrane was calibrated first and its constitutive parameters were obtained as the input for the FEM model. An entire cycle of loading and unloading was tracked under varying stress anisotropies. The simulation provides an insight into the soil-structure interaction between probe

membrane and cavity wall, with the emphasis of the pore pressure response at borehole surface that differs over the in-situ stresses and stiffness of the mediums. Two indices - critical expansion pressure and critical excess pore pressure were introduced to interpret the in-situ properties. By understanding the possible responses at each step of downhole instrumentation, a new interpretation method was suggested to better evaluate the in-situ stresses.

ACKNOWLEDGEMENT

I would like to thank my parents.

I would like to thank my supervisor, Dr. Rick Chalaturnyk and all the students and staffs in the reservoir geomechanical research group at University of Alberta for their generous support and encouragement.

I would also like to acknowledge Robert Whittle from Cambridge In-situ LTD. in UK and Hang Zhou from Hohai university in China and other dedicated researchers for their insightful view and valuable suggestions on my work.

Table of Contents

List of Figures

List of Tables

1 Introduction

A good management of the underground resources relies on the accurate estimation of the in-situ conditions of reserves and surrounding rock strata in every step of production. The development of the geomechanical model allows the variation of the material properties to be predicted in a certain time span.

A key factor in a geomechanical model is the knowledge of the original state of stress. An operation with poor estimation of the boundary stresses would cause both short-term and long-term problems with unnecessary costs for remediation, including the wellbore failure, the excessive deformation of tunnel and the instability of the underground cavern. More importantly, in the oil and gas field, understanding the change in the stresses in the formations helps put the disastrous events under the control, such as the activation of the pre-existing fault and the surface subsidence due to the reservoir depletion.

In Alberta, SAGD (steam-assisted gravity drainage) is one of the primary methods to produce bitumen from the oil sands reservoirs. With the constant steam being injected into the formation via the horizontal well, a high temperature chamber forms up where oil becomes less viscous and flows back to the production well (Figure 1-1). However, the excessive injection would severely pressurized the confined chamber and eventually displace overburden with the consequence of surface heave (Figure 1-2). The extreme high pressure would even breach the overburden and shear the caprock up to the surface. In the Jocelyn Creek incident, the steam was released to the atmosphere rapidly via the induced fractures, causing a catastrophic explosion that disturbed a large subsurface volume (ERCB, 2010).

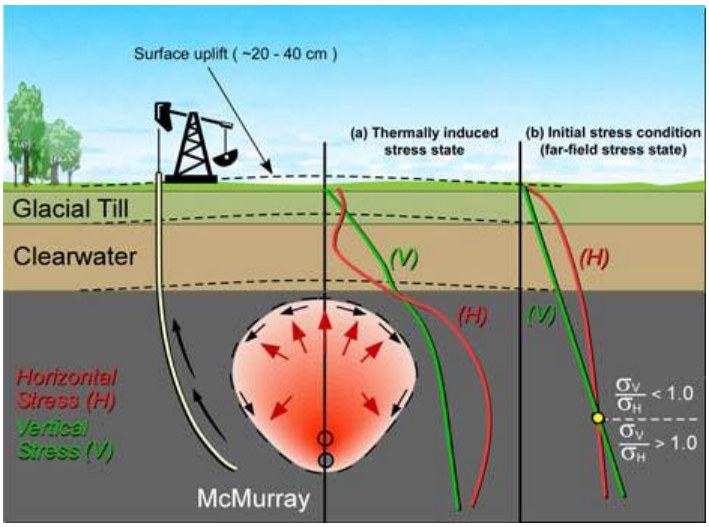

Figure 1-1. The schematic of SAGD production and the stress variation as a result of steam injection (Haug et al., 2013)

In order to protect the integrity of the overlying strata (known as caprock), the injection of steam has to be under a minimum operating pressure (MOP), which is only dependent of the minimum principal stress at the base of the caprock (Alberta Energy Regulator, 2014):

$$\text{MOP} = 0.8 \times \text{Minimum Principal Stress} \tag{1.1}$$

This minimum principal stress within the caprock, however, evolves with the entire life of the SAGD operation, as a result of the hydro-thermal coupling with the processes of steam injection and reservoir depletion (Walters et al., 2012). Thus, a periodical monitoring of the stress change is equally important as the initial subsurface investigation and a desirable downhole testing tool should be able to survive the high pressure and high temperature environment without sacrificing the measurement accuracy.

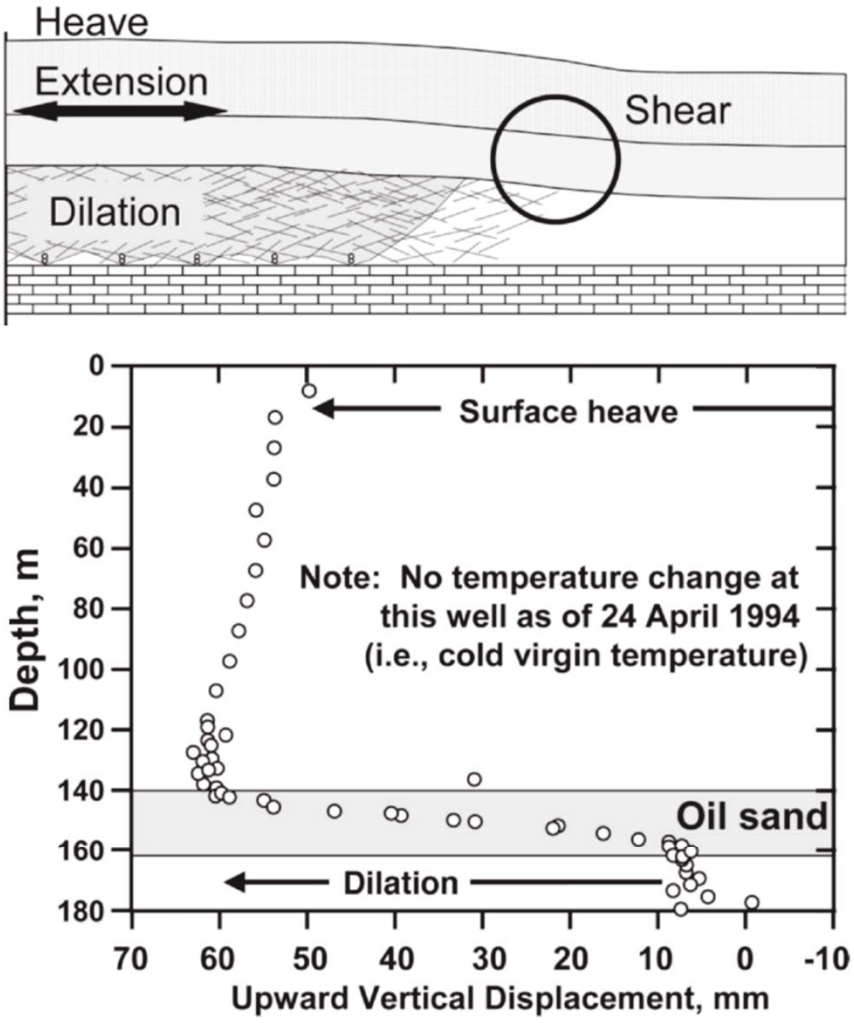

Figure 1-2. The mechanical failure of caprock (top) and the surface heave due to the excessive dilation of oil sands under high injection pressure (bottom(Collins, 2007)).

1.1 Techniques to Determine In-situ Stresses

The in-situ stresses are generated and transformed by geological sedimentation, erosion, thermal excursions, pore fluid diffusion, tectonic deformation in its geological history. In most case, it is reasonably assumed that the vertical stress is one of the principal stress and the other two are orthogonal in the horizontal plane.

The measurements of stress magnitude and their orientations are both possible by various testing methods done in the laboratory and/or field. However, hardly a single technique could allow for complete determination of the stress tensor (Figure 1-3). Consequently, a number of different but complementary techniques are recommended to cross validate the measurement with the geomechanical model and allow the stress states of maximum likelihood to be determined (Ask, 2006; Ledesma et al., 1996; Mckinnon, 2001).

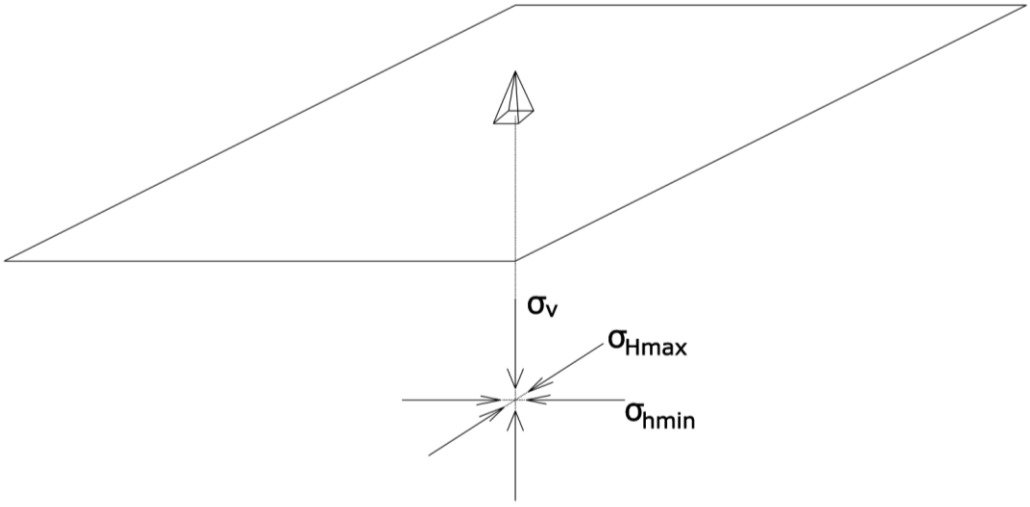

Figure 1-3. The assumed oretiation of orthogonal principal stresses

More than 10 approaches are available to measure the in-situ horizontal stresses in the deep ground (Ljunggren, et al., 2003; Schmitt, et al., 2012). Stress states could be inverted by knowing the regional tectonics and geologic history. Downhole tool string have been commonly employed in the oil industry to measure the initial stresses and formation pressure by characterizing the stress-induced fractures, recovering a deformed rock cores or transmitting and receiving the sounding through the medium, which nevertheless introduce disturbance to the virgin state (Hill and Peterson, 1994). Table 1-1 categorizes

the techniques for interpreting the magnitudes and/or orientations of in-situ stresses.

Compared to the deep space, the stress state has more variations and uncertainties at the shallow subsurface (<500m), even in the same formations and areas (Brown and Hoek, 1978). One of the reasons is that materials in this level are primarily fresh sedimentary deposits, which are relatively weak and unstable. Most materials exhibits considerable plasticity and are sensitive to the tectonic activities and manmade disturbance due to underground construction. This creates difficulties to the construction of most underground facilities. Thus, an accurate and fast measurement of in-situ stresses is necessary to help geologists and engineers understand the local ground response.

Table 1-1. The existing techniques for determining subsurface stress state

Determination Methods		Interpreted Parameters
Core Based Analysis	Anelastic Strain Recovery (ASR)	Stress orientations and magnitudes
	Acoustic Emission and Wave Velocity Analysis	Stress orientations and magnitudes
	Differential Strain Curve Analysis	Stress orientations and magnitudes
	Petrographic Examination of microcracks	Stress orientations
	Overcoring of archived core	Stress orientations
	Drilling-induced Fractures in Core	Stress orientations
Borehole Based Analysis	Hydraulic Fracturing	Stresses orientations and the magnitude of the minimum principle stress
	Borehole Breakouts	Stress orientations and the magnitude of maximum principle stress
	Borehole Expansions	Stress orientations and the magnitude of minimum horizontal stress; medium modulus
Near-Borehole Survey	Microseismic Logging	Stress orientations
	Earth Tilt	Stress orientations
Regional Geological Survey	Earthquake Focal Mechanisms	Stress orientations
	Fault Slip Data	Stress orientations

1.1.1 Core Based Analysis

Core based analysis proved to be a straightforward and inexpensive way to invert the in-situ stress state by reproducing the observed deformation after the in-situ stress is relieved after the core recovery. The non-elastic behavior (primarily the anisotropic viscoelastic strain) and the features of the induced fractures on the core in the long period of relaxation in a well-controlled

environment could be used to indicate the anisotropy of the in-situ stresses (Figure 1-4).

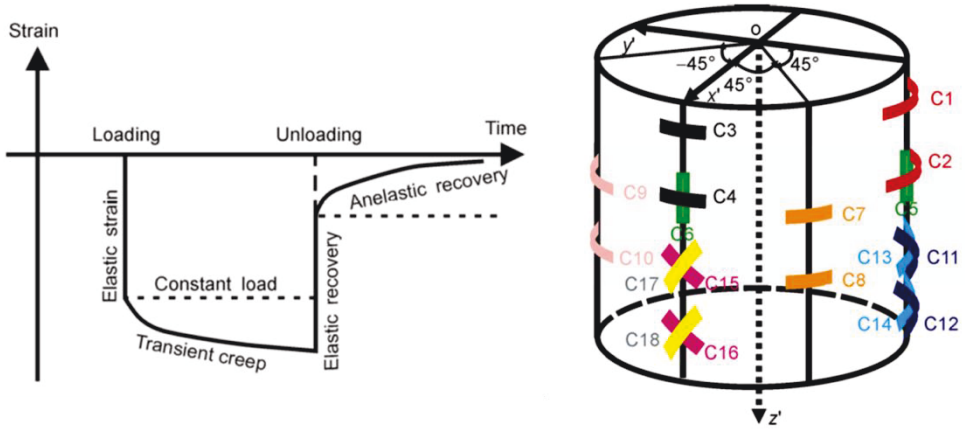

Figure 1-4. The schematic of anelastic strain recovery and the strain gauge installation in a three dimensional measurement (Sun et al., 2014)

However, the quality of inversion relies on the rheological properties of the materials and the magnitude of the original stresses at the depth where the sample is recovered. In general, the strain recovery method works better for great rather than shallow depth. Another issue is that the core sample is usually affected by the stress concentration near the core stub which might not be characterised as the axisymmetric stresses as the inversion model assumes. Thus, it brings more complexity to describe the stress state around the borehole by modelling it asymmetrically and three dimensionally (Lin et al., 2006). Thus, it is challenging to have an accurate and unambiguous measurement of the recovered anelastic strain on the soft rock obtained from the shallow subsurface is challenging.

1.1.2 Borehole Based Analysis

The in-situ testing can reflect the stress conditions more realistically because it avoids the processes of coring and handling of the sample and therefore

minimizes the possible disturbances. It has been widely employed by oil industry for detecting the virgin stress state. Among all the borehole testing techniques, the fracturing methods have been most widely used to determine the in-situ stresses. There are principally two types of fracturing – Hydraulic fracturing and Borehole-jack fracturing.

The techniques of hydraulic fracturing are principally based on the assumption that tensile fractures would be initiated in the direction perpendicular to the minimum in-situ stress by the fluid continuously pumped into the isolated borehole interval (Zoback, 2010). Hydraulic fracturing test allows minimum in-situ stress measurement at a high quality, and the complementary analysis of the drilling-induced borehole breakouts gives the magnitude of the maximum horizontal stress.

The principle of borehole-jack fracturing is to expand the borehole wall with the pressure applied on single or multiple jacking shells, or even a full-circular sleeve. The technique has been fundamentally described by Goodman (1989) in the application of determining the modulus of rock. It avoids the issues of water penetrating into the formations; also it improves the capture of fracturing opening with strain gauges installed on the shell.

Combined with both sleeve fracturing and hydraulic (or micro) fracturing modules, the Modular Dynamics Tester from Schlumberger provides the maximum efficiency by completing two tests in a single downhole trip. A number of MDT tests have been successfully performed in Alberta for the determination of the in-situ stresses in the caprock. Two straddle packers are jacked up sequentially to the maximum allowable pressure and the fracturing fluid is

pumped into the interval between packers. The breakdown and leak-off pressure can be observed in both steps whenever the fracture is initiated under the inflation pressure. It provides small two independent measurements of the minimum in-situ stress in the target zone.

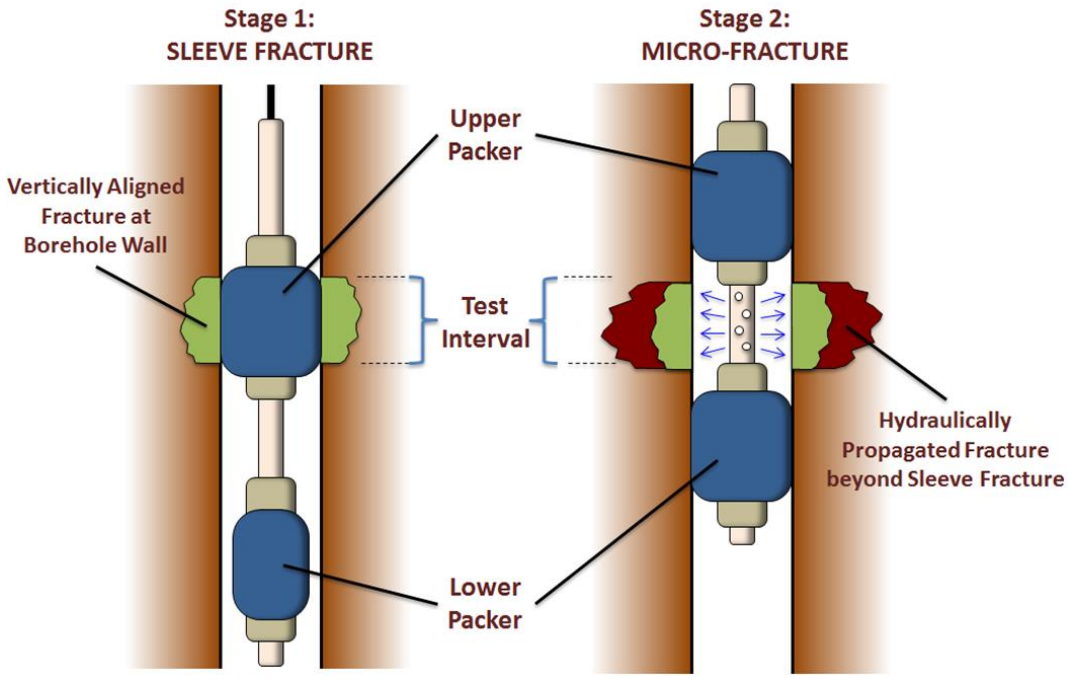

Figure 1-5. Two separate fracturing steps in the MDT testing

However, the accuracy of such method would be significantly reduced in the soft or medium stiff formations such as clayshale, because inelastic deformation including plastic yielding and grain compaction often takes place before fracturing in such formations. Also, the assumption in the hydraulic fracturing testing that the host rock is impermeable is always insufficient under the fact that injecting water partially infiltrates into and dissipates through the porous medium and. Additional error would be introduced if the expandable packer is not accurately calibrated, as the orientation at which the fracture initiates is very

sensitive to the subtle difference between curvatures of friction shell and borehole well.

The uncertainty of the fracturing methods conducted in the soft rock formations is addressed with a wide variability of in-situ stresses measured from the MDT testing in the shallow SAGD pilot project at Fort McMurray, Alberta (Figure 1-6, ShafieZadeh and Chalaturnyk, 2014). The observed minimum principal stress gradients are unreasonably higher than the vertical stress gradients. The assessment of the caprock integrity based on those results is therefore unreliable and risky.

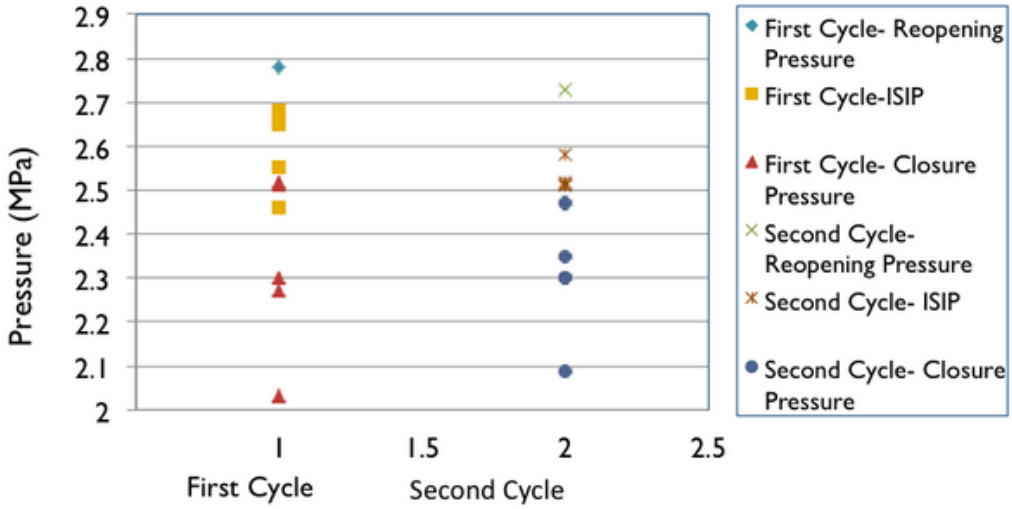

Figure 1-6. The interpreted minimum in-situ stress from the MDT testing

A variety of methods enable the in-situ stress anisotropy to be successfully captured in the hard rock formation. However, an accurate interpretation of stress anisotropy in the stiff soils or soft rocks is still absent because the drainage conditions are hard to predict in those boreholes and the induced inelastic deformation is intrinsically inexplicable for the interpretation. In this work, a new

methodology of interpreting the in-situ stress anisotropy by implementing pre-bored pressuremeter testing in the shallow unconsolidated formations is suggested and its feasibility is investigated by numerical analysis.

1.2 Pressuremeter Test and Its Interpretation Methods

Pressuremeter, also named elatometer or dilatometer, has been widely used in the site investigation for describing ground properties such as strength, deformation characteristics, in-situ horizontal stress and even permeability (Rangeard et al., 2003). In-situ pressuremeter testing was first introduced by Louis Menard (Menard, 1955). Considering the different installation methods, pressuremeter testing has been mainly classified into pre-bored pressuremeter test (PBPT) and self-boring pressuremeter test (SBPT). The advantage of the latter is that the instrument bores its own way into the ground and locks the probe in place allowing minimum stress relief of borehole. The disturbance caused by borehole drilling that PBPT applies is thus minimized in SBPT.

Throughout the 50 years development of pressuremeter, two perspectives of research have been frequently revisited:

1. How to characterize the behavior of different types of materials under an ideal cavity expansion condition.

2. With the interpretation model, how to account for and minimize the errors the test results might have due to the factors including drilling disturbance and unknown drainage conditions.

In order to reduce the uncertainty induced from the instrumentation, some improvements have been made on the testing devices over the years. Wroth and Hughes (1973) developed Camkometer assembled with pore pressure cell at the mid-height of the probe by which the excess pore pressure variation during the loading could be monitored. Huang et al., (2002) added a base plate beneath the pressuremeter probe to perform the borehole shear test and plate loading test by a single device so that the stiffness and strength of the soil could be measured independently and used for pressuremeter test interpretation. A compass sensor is equipped with the pressuremeter assembly for an offshore investigation to the 1000m deep seabed and the difference between the caliper measurements in the horizontal plane could be measured (Brucy and Letirant, 1986).

By modifying parts of the instruments and selecting different installation and inflation approaches, the pressuremeter system has been successfully applied to various test environments, such as offshore (Fyffe et al., 1985; Hughes et al., 1984), rock foundations (Failmezger et al., 2005; Huang et al., 1999), underground tunnels (Bocabarteille et al., 2000.), etc.

1.2.1 Cavity Expansion Theory

The pressuremeter test is commonly depicted as a cylindrical cavity expansion under the plane strain conditions with deformation in the axial direction constrained (Figure 1-7). Under the isotropic boundary condition, the radial stress σ_r, circumferential stress σ_ϑ are two principal stresses in the plane and satisfy the stress equilibrium at radius, *r*:

$$\frac{d\sigma_r}{dr} + \frac{\sigma_r - \sigma_\theta}{r} = 0 \qquad (1.2)$$

The strains at the directions of these two principal stresses are expressed as a function of the radial displacement at *r*, compression positive:

$$\varepsilon_r = -\frac{\partial \delta_r}{\partial r}$$
$$\varepsilon_\theta = -\frac{\delta_r}{r} \tag{1.3}$$

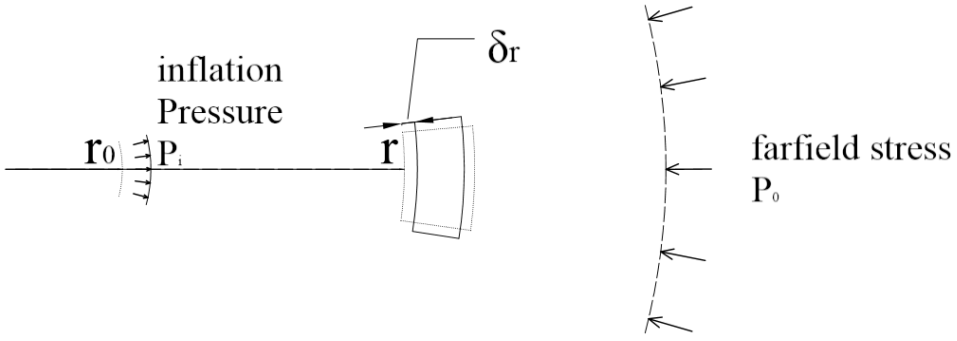

Figure 1-7. The boundary stress condition

By establishing the stress-strain relation using an appropriate elasto-plastic constitutive model, Equations (1.2) and (1.3) could be linked and solved together analytically or numerically in the entire axisymmetric domain. The following constitutive models have been employed for predicting the response of different types of soils under cavity expansions,

a. Linear elastic (Mair and Wood, 1987);

b. Rigid plastic (Hughes et al., 1977);

c. Linear elastic perfectly plastic (Carter et al., 1986; Houlsby and Withers, 1988; Jefferies, 1988; Vesic, 1972)

d. Nonlinear elastic perfectly plastic (Bolton and Whittle, 1999); and

e. Elasto-plastic with strain hardening or strain softening (Collins and Yu, 1996; Prevost and Hoeg, 1975).

While a more developed constitutive model can capture more realistic behavior of soil, it is sometimes difficult to be applied in engineering practice as extra parameters are introduced for the interpretation and some of them are unlikely to be determined by conventional test.

For the cavity expansion in the saturated medium in a certain time span, another continuum equation relating the volumetric change with pore fluid flow must be introduced,

$$\frac{\partial}{\partial t}\left(\varepsilon_r + \varepsilon_\theta\right) = \frac{1}{r}\frac{\partial}{\partial r}\left(r v_f\right) \tag{1.4}$$

where v_f is the velocity of the pore fluid at *r* within the soil and,

$$v_f = \frac{-k}{\gamma_w}\frac{\partial u}{\partial r} \tag{1.5}$$

where *u* is the pore fluid pressure and links the effective stresses with the total stress (Terzaghi, 1943),

$$\begin{aligned} \Delta\sigma_r &= \Delta\sigma_r' + \Delta u \\ \Delta\sigma_\theta &= \Delta\sigma_\theta' + \Delta u \end{aligned} \tag{1.6}$$

In this case, the degree of freedom becomes 2 as the excess pore pressure is treated as another variable to be solved other than the radial displacement. There are no close-formed solutions for a fluid-stress coupling cavity expansion problem, and the drainage boundary conditions must be defined for the numerical integration (Randolph and Wroth, 1979).

The test results are generally expressed as a plot of the cavity expansion pressure against the cavity strain, from which the cavity expansion theory are employed to make an interpretation. Gibson and Anderson (1961) has firstly proposed a method to interpret the undrained soil parameters for the pressuremeter test. The solution is based on the assumptions including: (1) soil is homogeneous and isotropic; (2) it deforms under plain strain and axisymmetric condition; (3) no volumetric strain occurs; (4) soil behaves as an ideal elastic-perfectly plastic material. It is recommended as a primary method to determine the undrained properties of cohesive soil, due to its simplicity and straightforwardness, even some findings showed the undrained shear strengths determined by this method were overestimated (Wroth, 1984). The mathematical development of Gibson and Anderson method will be discussed later for its incapability of estimating soil parameters under anisotropic initial stress condition.

Ladanyi (1972) and Palmer (1972) continued a further study of theoretical analysis suggested by Gibson and Anderson, and removed the restrictions to infinitesimal strain and elastic perfect-plasticity of soils. A full picture of shear stress: strain relation could be recovered by reinterpreting the expansion curve.

Vesic (1972) extended the solution outside of the undrained condition; by introducing the factor of reduced rigid index, the volumetric strain in the cavity vicinity was taken into account and the friction angle and the yielding pressure could be determined after an iterative process. This method is capable to find the Mohr Coulomb parameters regardless of the type of soils, but the determination of this new factor as mentioned above is highly subject to the

relative density, stress path and the confining pressure of the soil, which adds additional uncertainty to the interpretation.

Prevost and Hoeg (1975) considered both volumetric strain and shear distortion for the plastic deformation of material when yielded. Volumetric yield surface and shear yield surface respectively described by a linear function and a hyperbolic function were incorporated into a single model and the undrained behavior for strain hardening and strain softening was separately discussed by choosing different experimental parameters in their suppositions. The hypothesized model and its application to the cavity expansion problem depicted the inelastic soil deformation in a more realistic sense, but the cumbersomeness of the solving procedure as well as those parameters that are not usually physically defined limited its practice in the actual test.

The most widely applied interpretation methodology for granular materials was proposed by Hughes et al. (1977). In the assumption of constant volumetric change rate during the shear process, the friction angle (φ) and dilation angle (ψ) could be obtained by calculating the slope of the pressure-expansion plot in a bi-logarithmic space. The critical state value of the friction angle is required for the calculation beforehand.

The recent development of the cavity expansion model focused on the quick engineering application and the handling of initial drilling disturbance in the interpretation. Carter et al. (1986) derived an explicit solution for the drained cavity expansion of cohesive frictional materials. Houlsby and Withers (1988) relied on the information obtained from the unloading section of the cone pressuremeter expansion curve to reconstruct the true response of the

undisturbed soil by performing the graphical procedure. Following the Houlsby and Withers's methodology, Jefferies (1988) described the unloading process of pressuremeter testing mathematically and developed a program to best fit the contraction curve by checking and matching with analytical solutions. The formulation has then been extended to the large strain problems (Ferreira, 1993). The proposed mathematic expression has many advantages of being modified to investigate the sensitivity of the parameters it contains (the paper has given an example regarding to the strength anisotropy). However, the model is still restricted to the elastic-perfectly plastic constitutive behavior, which is not able to characterise the real response of natural soils.

1.2.2 Pre-bored Pressuremeter Test

The basic pre-bored pressuremeter setup is shown in Figure 1-8. The probe is dropped into a pocket drilled in advance. The fluid or compressed is injected into the probe through hoses for a pressure-controlled inflation. It can be lowered down as deep as the borehole can be drilled and the wireline is strong enough to deliver and retrieve the tool. However, the major defect in this method is the complete unloading of the cavity that occurs in the interim between removing the boring tool and pressurizing the pocket. The ground must be capable of standing open so the method is preferably applicable to the stiff materials. The comparison among the curves made by self-bored, push-in and pre-bored pressuremeter tests indicates a big influence of disturbance that causes a great amount of initial expansion and contraction of cavity before the test starts (Figure 1-9). The disturbance induced error dependent of the initial ground conditions is discussed later in the following chapters.

The pre-bored pressuremeter testing also allows the rock or soil samples to be recovered by coring at the same depth where the pocket is created. Thus the laboratory evaluation can be performed to obtain the geomechanical properties that could not only provide the necessary input for the interpretation of the materials being tested but also validate against interpreted results.

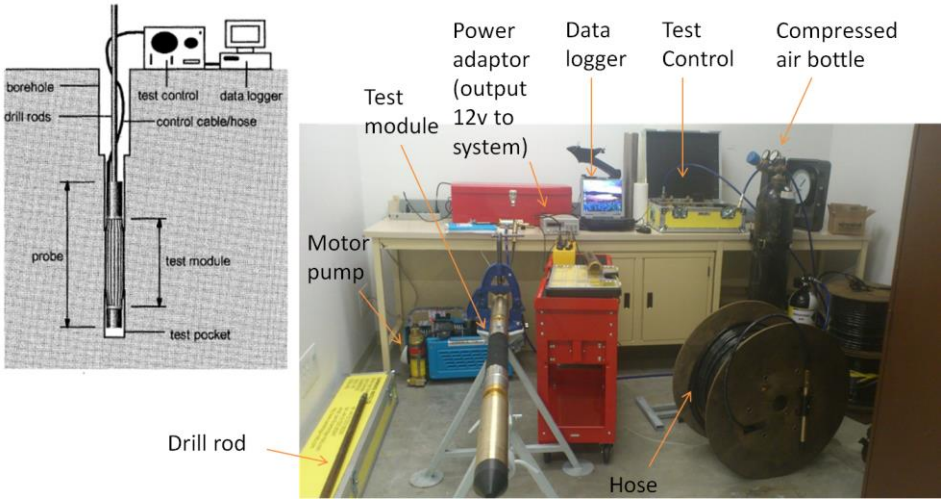

Figure 1-8. The basic setup of conventional pre-bored pressuremter/dilatometer

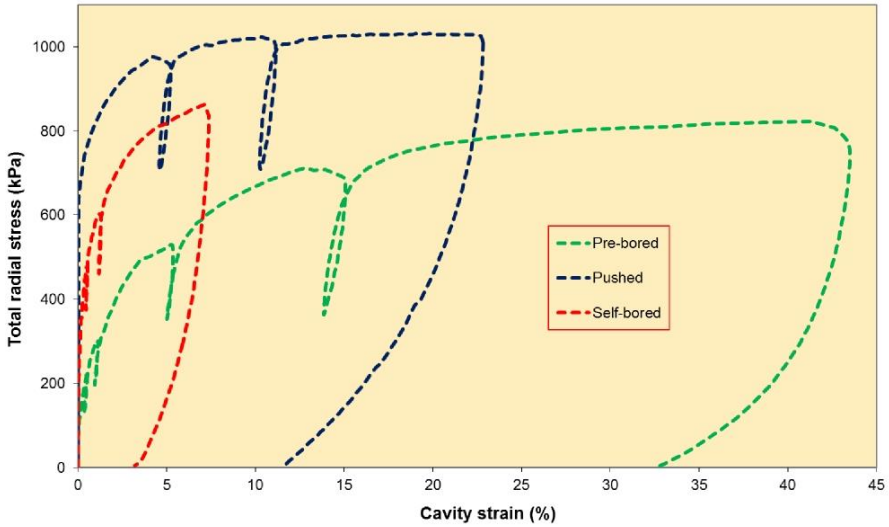

Figure 1-9. The expansion curves for three types of pressuremeter tests in Gault Clay (Cambridge Insitu Ltd)

The response of borehole can be separated into following steps for a pre-bored pressuremeter test in the saturated medium (the stress states in the bracket are at the expansion surface):

1. Drilling - Immediate unloading of the ground at the instance of drilling ($\sigma_r' < \sigma_\theta'$).

2. Borehole Relaxation - The deformation continues as the consolidation occurs after drilling ($\sigma_r' < \sigma_\theta'$).

3. Elastic Expansion - Probe pushes against the soil and the initial stress state is recovered at some point ($\sigma_r' < \sigma_\theta' \rightarrow \sigma_r' > \sigma_\theta'$).

4. Plastic Expansion - The further expansion shears the borehole wall and ultimately reach the critical state (a state where no further volumetric change takes place) ($\sigma_r' > \sigma_\theta'$)

5. Elastic Contraction - The borehole stops expanding and starts contracting as the probe is unloaded; the material returns into elastic phase but the expansion-induced plasticity permanently remains ($\sigma_r' > \sigma_\theta' \rightarrow \sigma_r' < \sigma_\theta'$).

6. Plastic Contraction - The plastic contraction initiates at the borehole wall and the zone that is plastically deformed keeps increasing until the probe is completely unloaded. ($\sigma_r' < \sigma_\theta'$).

It's worth noting that the state (elastic, plastic and critical state) changes in both loading and unloading outlined above makes the interpretation for the pre-bored pressuremeter testing complicated. A few assumptions underlying a group of existing interpretation approaches simplify the problem and have been widely accepted. However the controversy still exists especially for the step 2 about whether the soil would really come back to its undisturbed condition, i.e., is the stress relief reversible? The answer for the plastic unloading is clearly no, but how about if only elastic unloading occurs? Palmer (1971) assumed the elastic deformation would be recovered as the pressure applied reaches the horizontal stress σ_{h0}. However, several findings (Silvestri, 2004; Prevost, 1979) showed that this assumption would lead to the overestimation of shear strength and correction should be applied to the apparent stress-strain relationship.

For this class of problem, an analytical solution was derived by an Wang and Dusseault (1994) who evaluated the stress paths at the vicinity of circular opening from active loading ($\sigma_r' < \sigma_\theta'$) to passive loading ($\sigma_r' > \sigma_\theta'$) on a Mohr-Coulomb material. The stability of the borehole is quite sensitive to the high stress field; either the excavation or the subsequent hydraulic loading may cause damage or irrecoverable deformation to the materials. Thereby, there would not be a universal stress path for soil elements in the entire radius and the similarity solution in the Euler domain is no long valid in this case. The unloading and loading processes should be sequentially investigated on each individual material particle. This conception is illustrated in a plane strain circular opening under a uniform boundary loading (Figure 1-10); the strain weakening or strain hardening is possible as the yielding initiates (drilling unloading), retreats (elastic expansion) and renews (plastic expansion).

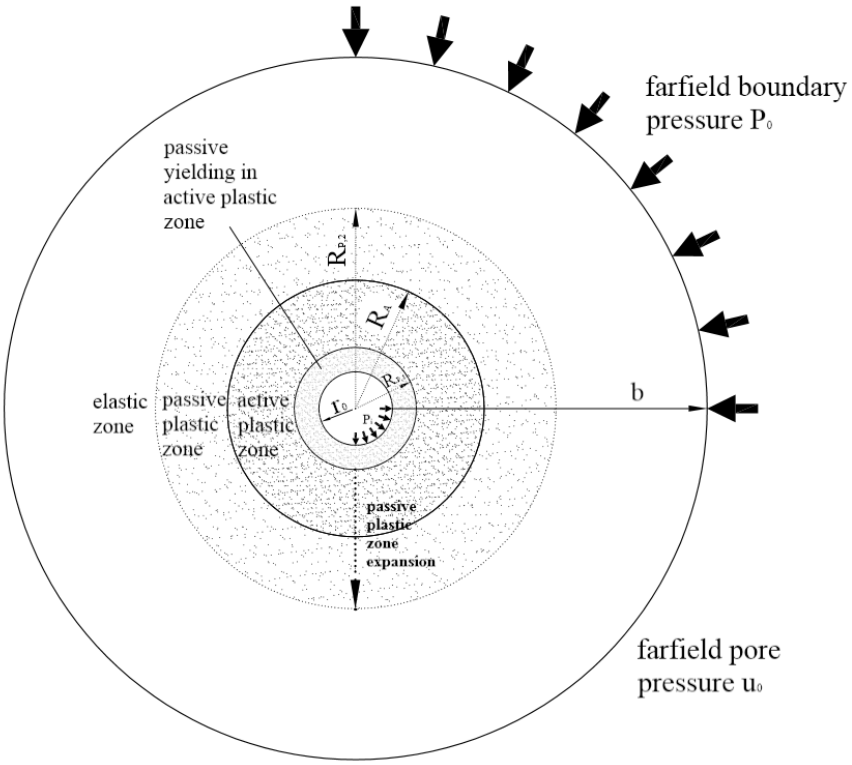

Figure 1-10. The change of plastic zones responding to different loading modes (active and passive) in pre-bored pressuremeter testing

1.2.3 Cavity Expansion in Cam Clay Materials

Weak shale which constitutes many of the caprocks within Alberta oil field formations (Hamilton and Babet, 1975). Such formations display hysteresis in their deformation response to external loading and stress histories may significantly alter the linear relation between loading and deformation.

The concept of critical state has been firstly introduced by (Roscoe and Burland, 1968) to describe the intrinsic soil behavior by defining stress-path dependent nonlinearity in both elastic and inelastic phases. It was originally named as "Modified" Cam Clay model to distinguished from an earlier Cam Clay model which had been found discontinuous when calculating the plastic potential under

an isotropic pressure increment (Wood, 1990). The Modified Cam Clay model is also suitable for application to numerical modeling. In this thesis, the Modified Cam Clay model will be abbreviated as MCC.

The yield function of the MCC is expressed as

$$f(q, p', p'_c) = q^2 - M^2 \left[p'(p'_c - p') \right] \tag{1.7}$$

where q is the deviatoric stress, written as a function of principal stresses σ_1, σ_2 and σ_3:

$$q = \sqrt{\frac{1}{2}\left[(\sigma_1 - \sigma_2)^2 + (\sigma_2 - \sigma_3)^2 + (\sigma_1 - \sigma_3)^2 \right]} \tag{1.8}$$

p' is the mean effective pressure,

$$p' = \frac{\sigma'_1 + \sigma'_2 + \sigma'_3}{3} \tag{1.9}$$

p_c' is the pre-consolidation pressure under the isotropic compression and M is the slope of critical state line in the q:p space (Figure 1-11).

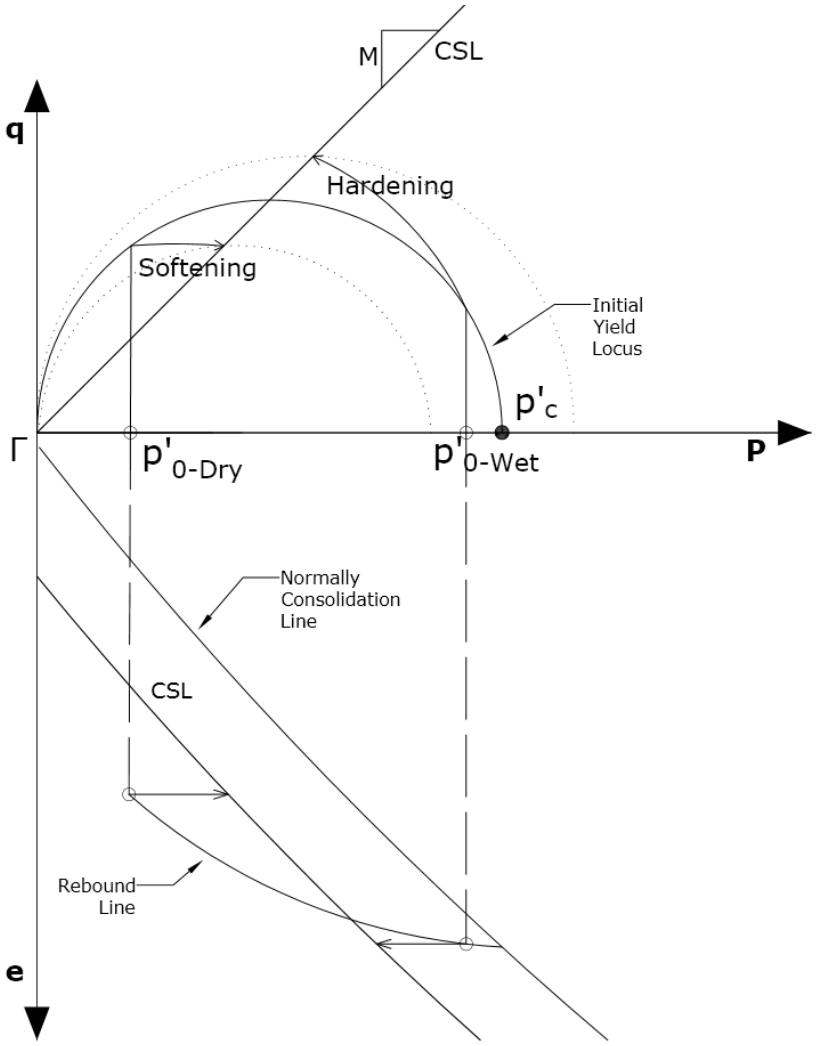

Figure 1-11. Stress paths of MCC mateirals in the space of *q(deviatoric stsress)-p(mean stress)-e (void ratio)* under undrained loading condtions

The stress: stain response can be decomposed into two parts with respect to the volumetric ($d\varepsilon_p$) and deviatoric ($d\varepsilon_q$) increments:

1) The elastic term:

$$\begin{bmatrix} d\varepsilon_p^e \\ d\varepsilon_q^e \end{bmatrix} = \begin{bmatrix} \kappa/\nu p' & 0 \\ 0 & 1/3G \end{bmatrix} \begin{bmatrix} dp' \\ dq \end{bmatrix} \tag{1.10}$$

2) The plastic term:

$$\begin{bmatrix} d\varepsilon_p^p \\ d\varepsilon_q^p \end{bmatrix} = \frac{\lambda - k}{p'(1+e)(M^2+\chi^2)} \begin{bmatrix} (M^2-\chi^2) & 2\chi \\ 2\chi & 4\chi^2/(\mathrm{M}^2-\chi^2) \end{bmatrix} \begin{bmatrix} dp' \\ dq \end{bmatrix} \quad (1.11)$$

where λ and κ are the slopes of normal consolidation line and swelling line respectively; $\chi = q/p'$; and G is the shear modulus, which is also the function of the p' and the specific volume υ :

$$G = \frac{3(1-2\nu)\upsilon p'}{2(1+\nu)\kappa} \quad [1] \quad (1.12)$$

The hardening or softening behavior of Cam Clay materials can be characterized by an exponential function of volumetric plastic strain increment:

$$p_c^{i+1} = p_c^i \exp\left[\frac{-d\varepsilon_p^p}{\lambda - \kappa}\right] \quad (1.13)$$

where p_c^{i+1} is the current yield preconsolidation pressure and p_c^i is the preconsolidation pressure in the last step.

The similarities in the mechanical behavior between soils and shales reveal that the critical state soil models have the possibility of being developed and applied to better describing the mechanical behavior of shales (Steiger and Leung, 1991). It also simplifies the computations by incorporating the compaction model and the yield model, which are separately considered in the traditional petroleum geomechanics analysis (Timothy, 1980), into a single model. The emergence of

[1] It should be noted, the assumption that the Poisson's Ratio ν remains constant as the material deforms is made through the thesis. An alternative to this is keeping G constant and calculating the Poisson's ratio. The benefits and short comings of these two assumptions are discussed by Zytynski and Randolph. (1978)

the various new techniques for the measurement of the shale properties such as volume compressibility and the preconsolidation pressure (Gutierrez et al., 2008) enables critical state parameters to be accurately identified.

The Cam Clay Model was employed by Carter (1979) and Randolph et al.(1979) on the undrained cylindrical expansion problem to investigate the ground behavior around installed piles. Collins (1994) studied the cavity expansion under both the drained and undrained conditions by applying similarity solutions technique. Collins and Yu (1996) found the more general solutions based on both the original and the modified Cam Clay models towards the large-strain undrained expansion problem. An exact closed-form solution was provided by Cao et al.,(2001) and validated the numerical solution of Collins and Yu (1996). The out-of-plane stress was also considered in a semi-analytical solution for predicting the expansion behavior under K_0 conditions (Abousleiman and Chen, 2012).

While various theories were developed to predict the soil behaviors dependent on critical state parameters, none of them have been applied to interpret the results from pressuremeter testing (only a solution-based interpretation of the piezocone test in clay was published (Chang et al., 2001)). The complexity of constitutive model as well as the sophisticated solving process contributes to the difficulties of inverting the soil parameters efficiently.

1.3 The Fluid-Stress Coupled Simulation in Abaqus

The numerical analyses conducted for most of the studies in this thesis are done by a general-purpose finite element program, Abaqus (v6.12). The expansions

under isotropic initial stress and anisotropic stress are treated differently with two model configurations for the minimum computation expense without sacrificing the computational accuracy. The expansion medium is treated as Modified Cam Clay materials with the Darcy flow coupled inside of the calculation.

1.3.1 Fundamentals of the Stress-fluid Coupling

The porous medium is modeled by the traditional approach that adopts an effective stress principle, defined by

$$\boldsymbol{\sigma}' = \boldsymbol{\sigma} - su_{pore}\mathbf{I} \tag{1.14}$$

where $\boldsymbol{\sigma}$ is the total stress tensor; u_{pore} is the liquid pore pressure and s is a saturation factor, being 1 when the medium is full saturation.

The stress-strain relation can be described using effect stress term based on any constitutive models, and its decomposition for Cam Clay model has been given in Eqns (1.10) and (1.11).

The stress equilibrium for the solid phase is expressed by configuring the virtual volumetric work at time t in the case of full saturation:

$$\int_V \boldsymbol{\sigma}' : \delta\varepsilon dV = \int_S \mathbf{t_n} \cdot \delta\mathbf{v} dS + \int_V \mathbf{f} \cdot \delta\mathbf{v} dV + \int_V (n\rho_w) g \cdot \delta\mathbf{v} dV \tag{1.15}$$

where $\delta\varepsilon = \mathrm{sym}(\partial\delta\mathbf{v} / \partial\mathbf{x})$ is the virtual rate of deformation, $\delta\mathbf{v}$ is a virtual velocity field, $\mathbf{t_n}$ are surface tractions, $\mathbf{f}$ are body forces of solid part and ρ_w is the density of the fluid, g is the gravitational acceleration and n is the porosity.

The continuity of fluid flowing through the porous medium is expressed as at each time increment:

$$\frac{d}{dt}\left(\int_V \frac{\rho_w}{\rho_w^0} n dV\right) = -\int_S \frac{\rho_W}{\rho_W^0} n\mathbf{n}\cdot\mathbf{v}_w dS \tag{1.16}$$

where $\mathbf{v_w}$ are the seepage velocities, given by $\mathbf{v}_w = -k\frac{\partial u_{pore}}{\partial \mathbf{x}}$ and k the permeability of medium, $\mathbf{n}$ is the outward normal to the medium ρ_w^0 is the reference density of the fluid.

Eqn (1.16) are discretized with finite elements and integrated using the backward Euler approximation with the variable of pore pressure computed from Eqn (1.15).

It would be noted that, in the transient fluid-stress coupled modeling, there is no upper limit step on the time step while the lower limit is present especially for the problem in which the pressure-sensitive plasticity is concerned. Small time increments may cause spurious oscillations if the corresponding model is coarsely meshed. For saturated Darcy flow in the medium of incompressible grains, there is a guideline for the modeller to define the minimum time step:

$$\Delta t > \frac{\gamma_w}{6Ek}(\Delta l)^2 \tag{1.17}$$

where γ_w is the unit weight of the fluid; k is the permeability; and Δl is the dimension of the largest element, E is the Young's modulus for elastic deformation or equivalent modulus for plastic flow.

1.3.2 Basic Assumptions for the Cavity Expansion Simulations

1. The borehole is parallel to the vertical stress, which constitutes the principal stresses with another two stresses in the horizontal plane.
2. The deformation is under plane-strain condition.
3. The initial material properties in the unexcavated region are uniform and isotropic.
4. The porous medium is fully saturated and Darcy's law describes the liquid flow.
5. No discontinuum behavior such as borehole breakout or fracturing is considered in the simulation.
6. The sign convention used in this thesis specifies that the tensile stress is taken negative while the compressive stress is positive; the inward radial displacement (or convergence) is considered as negative while the outward radial displacement (or divergence) is positive.

1.4 Outline of the Thesis

The objective of the research is to evaluate the borehole response based on the critical state soil model under the operational condition of the pressuremeter testing. The pore pressure change and deformation are two primary characteristics to be predicted with the numerical models and to be investigated for the sensitivity of a variety of in-situ geomechanical parameters, including soil stiffness, strength and boundary stress ratios, to the consequent soil behavior. According to the results of the parametric study, a workflow of interpretation for

RGP (Reservoir Geomechanical Pressuremeter) testing is proposed with the details of back-calculating each individual in-situ geomechanical parameter from a sequence of independent measurements.

The general outline of thesis is presented in Figure 1-12.

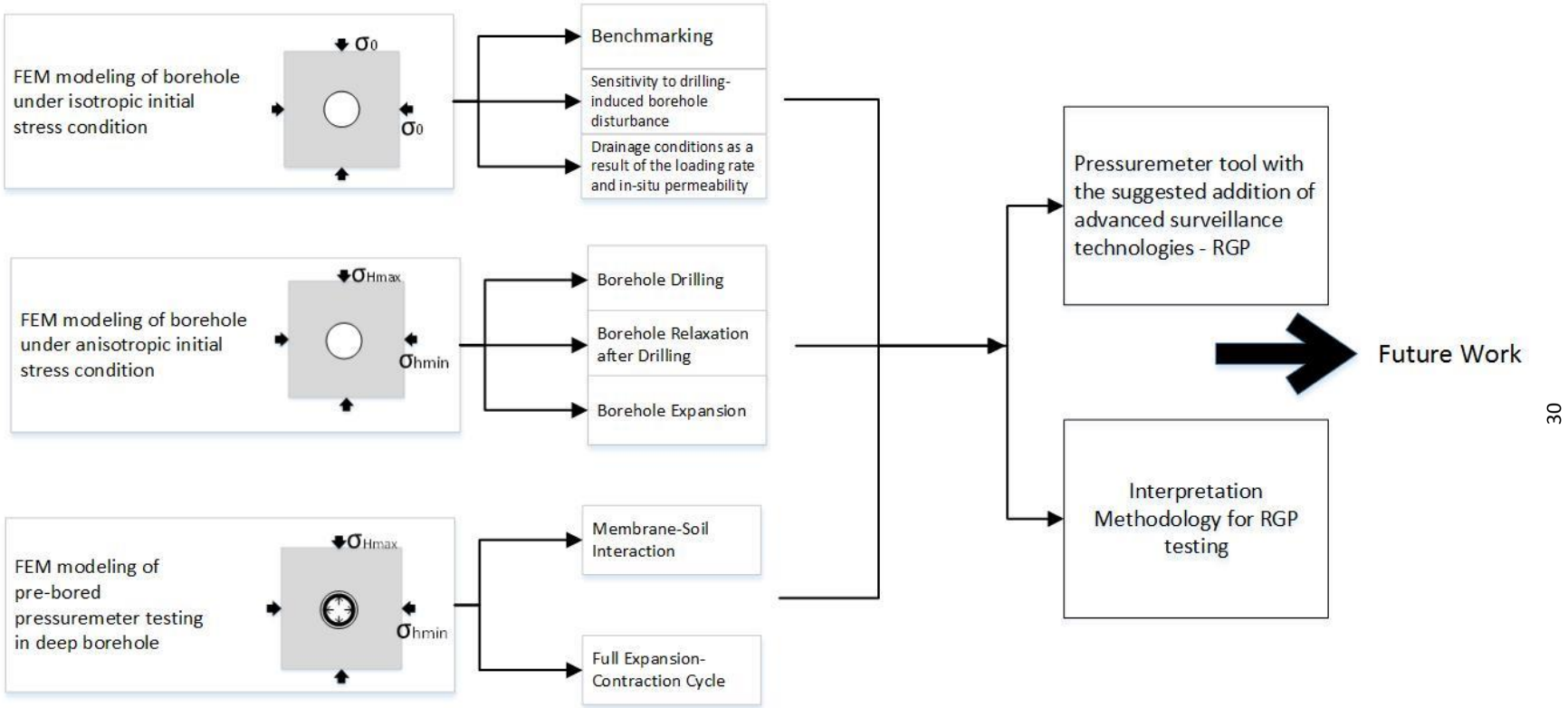

Figure 1-12. Outline of the thesis

2 Cylindrical Cavity Expansion under Hydrostatic Boundary Stress

Various approaches to interpret the cavity expansion curve have been developed. The interpretation methods can be categorized based on the types of constitutive model, the installation and testing techniques, and most importantly, the drainage condition during the test. For the granular materials, drainage is allowed due to their high permeability and Hughes method (Hughes et al., 1977) is generally accepted for the test interpretation by assuming completely drained conditions. For clayey materials, drainage depends on the loading rate and soil permeability and the Gibson and Anderson (1961) method could be applied to determine the undrained properties and initial horizontal stress from the expansion curve. However, if soil is only partially drained, there is no unambiguous way to invert the drained or undrained properties since the excess pore pressure is not predictable by existing approaches.

Thus, it becomes important to understand the drainage condition before the test is implemented. The formation of interest, clay shales in the case of this research, has permeability varying from 10^{-3} mD to 0.1 mD. Loading on such a material at a normal rate is not able to secure an undrained expansion. Herein, a parametric study is conducted by modeling the cavity expansion to categorize the drainage conditions for pre-bored pressuremeter testing.

2.1 Pore Pressure Response of Cavity Expansion

Ideally, if the cavity expansion takes place instantaneously, such as pile driving and pipeline installation, the initial status of soils will be considered intact and the pore pressure dissipation is prohibited over such a short time. This class of

problems is called the Quick Insertion Problem. The formulation of the Quick Insertion Problem provides the theoretical basis for the self-bored pressuremeter test in the impermeable and undisturbed soils.

2.1.1 Analytical Expression of Excess Pore Pressure for Quick Insertion Problem

A closed form solution for the pore pressure distribution due to an expansion from r=0 to r_0 has been suggested by Randolph et al. (1979) and Carter (1979):

$$\Delta u(r)^1 = \begin{cases} 2Su\ln(R/r) & r_0 \le r \le R \\ 0 & r > R \end{cases} \tag{2.1}$$

where the elastic-plastic boundary R is given by

$$(R/r_0)^2 = G/Su \tag{2.2}$$

Since the excess pore pressure due to pure shear is not taken account, only the mean stress influences its variation. Collins & Yu (1996) improved the solutions by introducing the factor of deviatoric stress to the pore pressure change

$$\Delta u(r)^2 = \begin{cases} \Delta u_R - (p' - p_0') - \dfrac{1}{2}(q - q_0 - (J(\gamma) - J(\gamma_R))) & r_0 < r < R \\ -\dfrac{G_0}{2}\Upsilon^2 & r > R \end{cases} \tag{2.3}$$

where Y and Y_R are the shear strain during the expansion and at the plastic annulus, respectively and Δu_R is the excess pore pressure at plastic annulus. The integral J could be evaluated numerically:

$$J(\gamma) = \int^{\gamma} \frac{q}{(\exp(\gamma) - 1)} d\gamma \tag{2.4}$$

Chen and Abousleiman (2012) improved the solution by removing the limitation on the initial conditions of isotropic stresses and including the influence of axial

stress on the plastic deformation. The excess pore pressure variation at a specific annulus *r* could be given as

$$\Delta u(r)^3 = \begin{cases} \sigma'_R - \sigma'_r(r) - \int_R^r \frac{\sigma'_r - \sigma'_\theta}{r} & r_0 < r < R \\ 0 & r > R \end{cases} \quad (2.5)$$

In this study, the expansion of cylindrical cavity has been simulated by a 1D axisymmetric model using Abaqus(v6.12). The results were benchmarked with the analytical solutions, and the advantage of numerical approach is worth noting by knowing the limitations of uncoupled calculations.

2.1.2 Benchmarking for Numerical Model

The model is meshed with 100 elements and 503 nodes, graded by a factor of 1/25(Figure 2-1). The ratio of b/r_0 equal to 40 is sufficient to model the condition of infinite medium (Rangeard et al., 2003). The far field pressure is kept as 120kPa and the internal pressure P_i increases from 120kPa to 480kPa at predefined rates, which allows different time for pore pressure dissipation. The only permeable boundary in this model is at the far field end. The displacement in the axial direction is constrained provided that the axis of wellbore is considerably longer than the thickness of model slice. Since the initial pore pressure could be arbitrarily defined without influencing the effective stress path in undrained case, only the excess pore pressure has been considered.

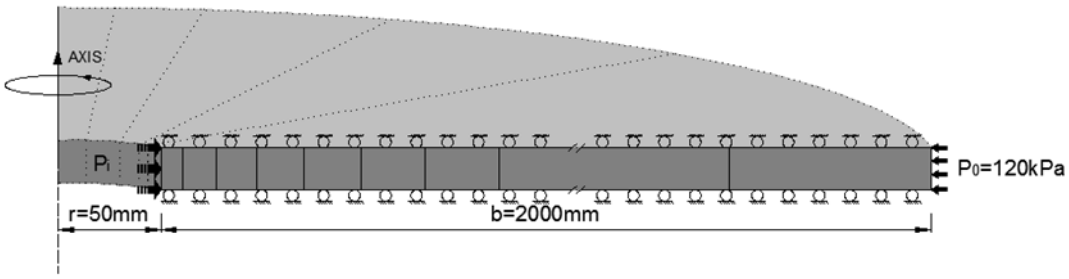

Figure 2-1. 1D axisymmetric model for cavity expansion

Two important parameters to classify the drainage conditions are permeability and loading/straining rate (Sheng et al., 2000). If a very fast straining rate is applied with a set a low permeability, soil will deform under an undrained condition, which results in a non-uniform distribution of excess pore pressure along the wellbore radius. In this study, a porosity-independent permeability of 10^{-12} m/s and a loading rate of 3kPa/s were assigned for the benchmark model as decreasing permeability further or increasing loading rate further would result in insignificant change of excess pore pressure. However, the determination of drainage condition requires a parametric study with finely specified variations of permeability and loading rate, which will be discussed in Chapter 3.

The comparison of the results from different approaches (Figure 2-2) shows that the numerical computation gives a good approximation to the analytical findings by Abousleiman & Chen (2012) and Collins & Yu (1996). However, error arises in the elastic zone when compared to the Abousleiman & Chen's analysis since they haven't taken into account the pore pressure generated due to pure shear. It presents a close match with Collins & Yu's result in each deformation zone, but it should be also mentioned that the their analysis is based on the assumption that the deviatoric and mean effective stress are independent of the axial stress, i.e., $q = \sigma_r - \sigma_\theta, p' = \frac{\sigma'_r + \sigma'_\theta}{2}$, which is not valid for the condition of anisotropic stresses.

The FEM model has been also validated with the Aboulesiman & Chen's results in the condition of anisotropic axial and transverse stresses (Figure 2-3). The pore pressure variation at the cavity wall responding to the wellbore straining matches very well with the analytical solution.

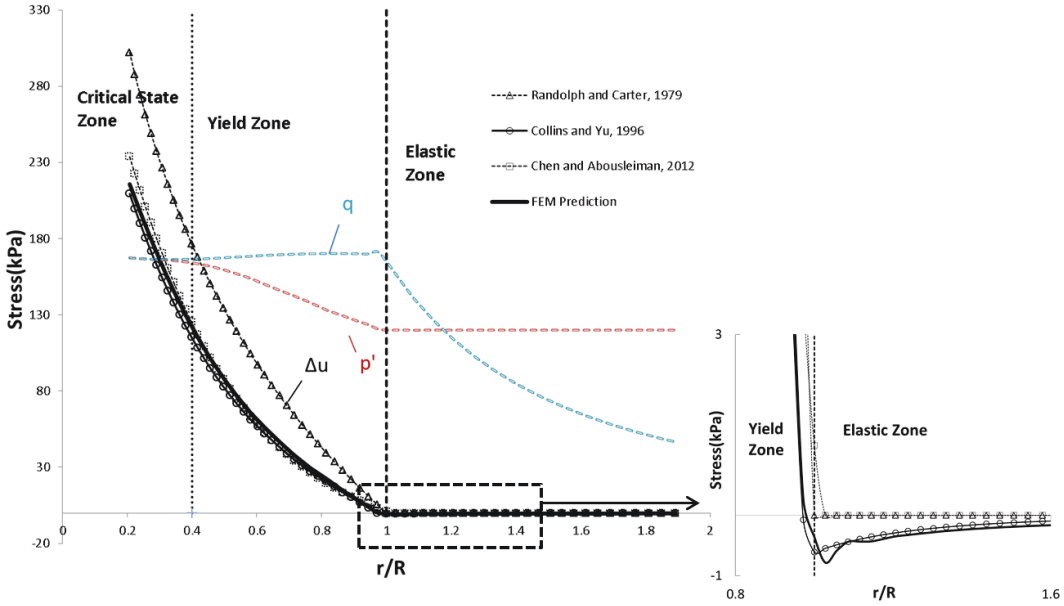

Figure 2-2. Comparison between the numerical results and analytical results for undrain expansion in the condition of isotropic stresses. The OCR is 3 and G0 is 4111kPa.

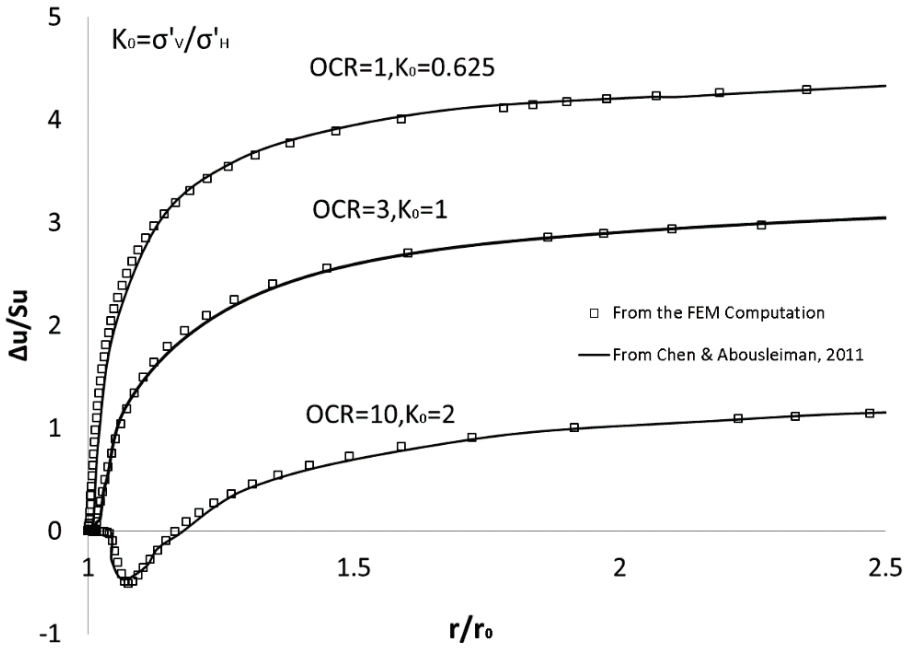

Figure 2-3. Pore pressure variation at cavity wall for soils with different initial stress anisotropies and overconsolidation ratio $OCR = P_c^{'} / P_0^{'}$

2.1.3 Classification of Drainage Conditions

Rangeard et al. (2003) defined the undrained, drained and partially drained conditions for pressuremeter testing based on a parametric study on the strain rate and permeability. However, the classification for their test results was not that clear and reasonable, and the samples they tested are not enough (only four) to be categorized for a general criterion. Also, the permeability for a particular sample was assumed constant during the test, which might not be true if a large deformation induces a significant permeability change in the actual condition.

In this study, the numerical model outlined above was employed for investigating the drainage condition caused by varying loading rate and permeability. Interest was placed on the void ratio change since it not only reflects the pore pressure dissipation in the poroelastic medium but also makes it possible to further discuss how the permeability change is interacting with subequent loading.

Figure 2-4 and Figure 2-5 show the stress trajectories under both undrained and drained conditions. For the convenience of comparison, the total stress here is defined by subtracting the ambient pore pressure, i.e., p-u_0. Unlike the undrained expansion, the drained expansion path will pass through the yield surface and approach the critical state line (CSL) ending up at a considerably high deviatoric stress. The effective mean stress, which increases simultaneously, compresses the skeleton of material and reduces the void ratio of medium (even though the heavily overconsolidated material shows dilation behavior at the beginning of yielding). By contrast, the response of the soil skeleton to the instantaneous pore pressure buildup has been delayed in the undrained condition, so the void ratio remains constant, even though the total stress path

has a sharp turn after yielding. Thus, it is reasonable to classify the drainage conditions by evaluating the void ratio change from the simulation results.

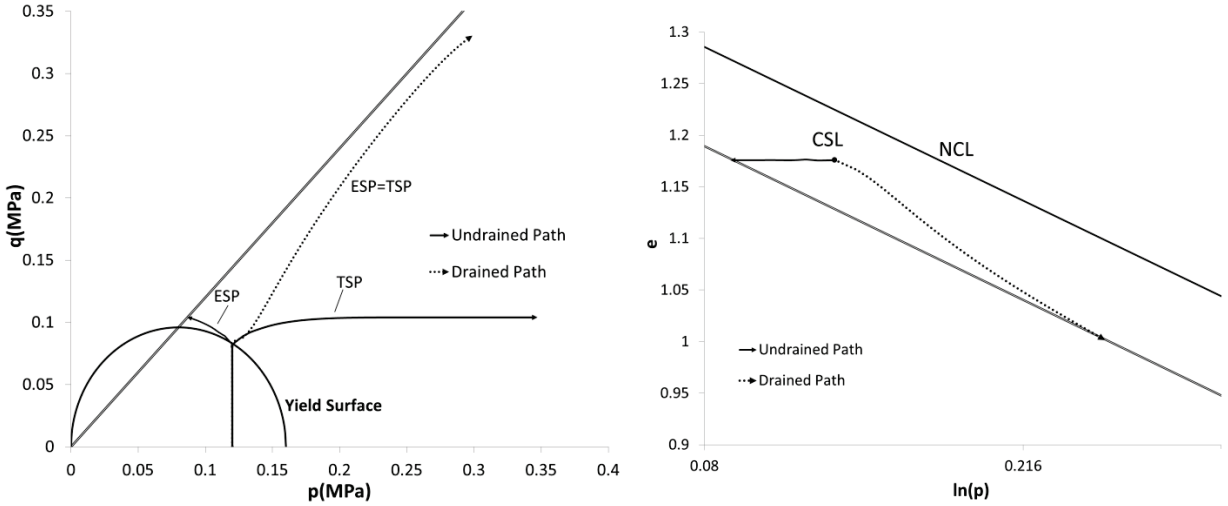

Figure 2-4. Stress paths and void ratio evolution of cavity expansion at $r=r_0$ for lightly overconsolidated formations (OCR=1.5) in two different drainage conditions. [2]

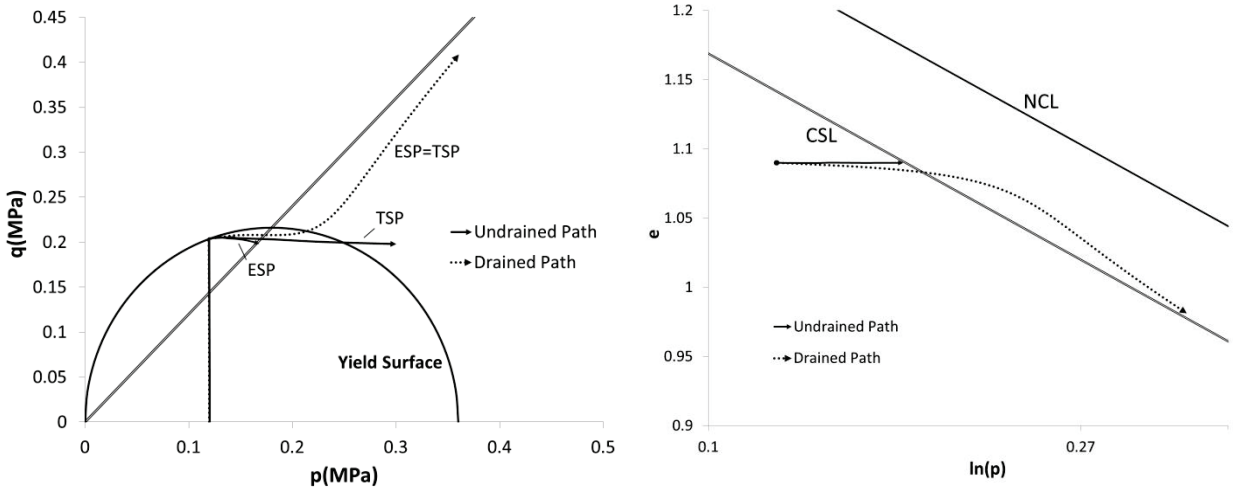

Figure 2-5. Stress paths and void ratio evolution of cavity expansion at $r=r_0$ for moderately overconsolidated formations (OCR=3) in two different drainage conditions.

[2] The MCC constants for this study are: Γ=2.86, λ=0.15, κ=0.03, μ=0.278 and M=1.2.

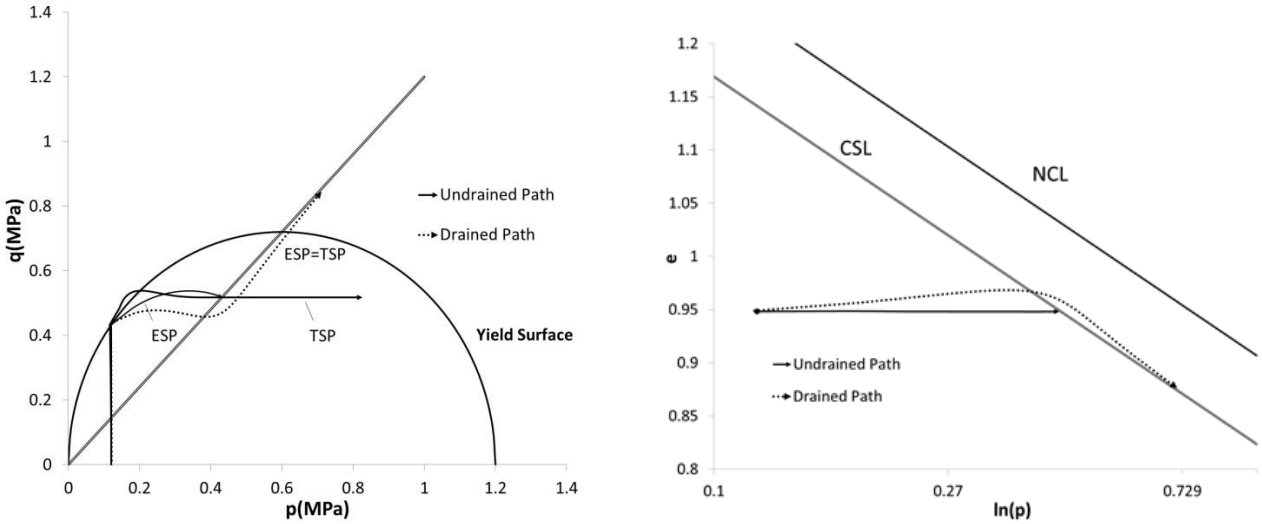

Figure 2-6. Stress paths and void ratio evolution of cavity expansion at $r=r_0$ for heavily overconsolidated formations (OCR=10) in two different drainage conditions.

Fast loading and low permeability are both likely to create undrained conditions. Figure 2-7 shows the resultant void ratio change under different loading rates and medium permeabilities. It should be noted that the permeability of shales is generally much lower than other geological formations, ranging widely from 10^{-16} m^2 to 10^{-24} m^2 (approximately 10^{-6}mm/s to 10^{-14}mm/s) (Mesri, 1982; Kwon, 2004). Also, the pumping capacity in pressuremeter testing allows loading rate of 100 kPa/s at most and 0.1kPa/s at least if the relaxation time of 30s to 1min after each step of pressure increment is considered in the calculation. The possible test conditions are located in the shadowed area in Figure 2-8. The pore water of most shale materials can only partially dissipate. Only when the initial permeability varies from 10^{-14} mm/s to 10^{-10} mm/s, could the undrained condition be possibly achieved by increasing the loading rate. Drained expansion is unlikely to take place. If, however, fracturing or collapse occurs when the material goes beyond the elastic deformation, abrupt change of permeability will result in the local drainage, which is not discussed in this study.

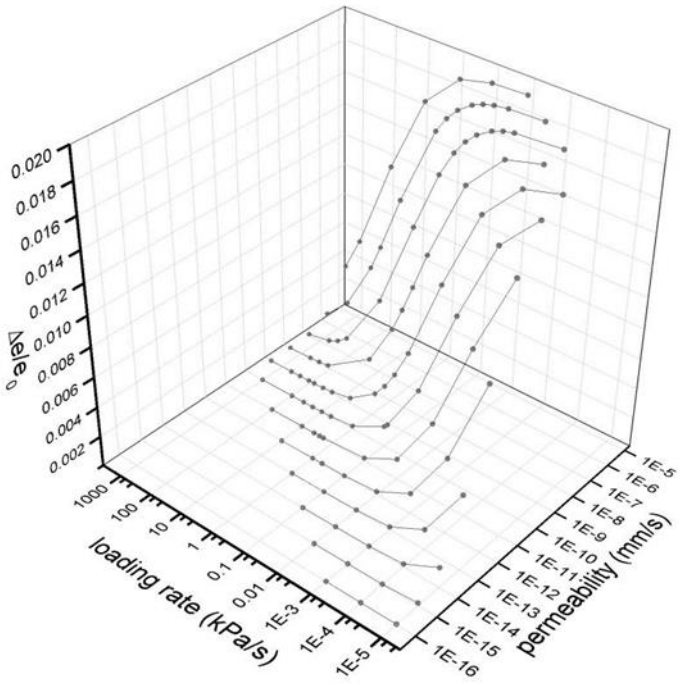

Figure 2-7. The change of void ratio responding to the different combinations of loading rate and permeability.

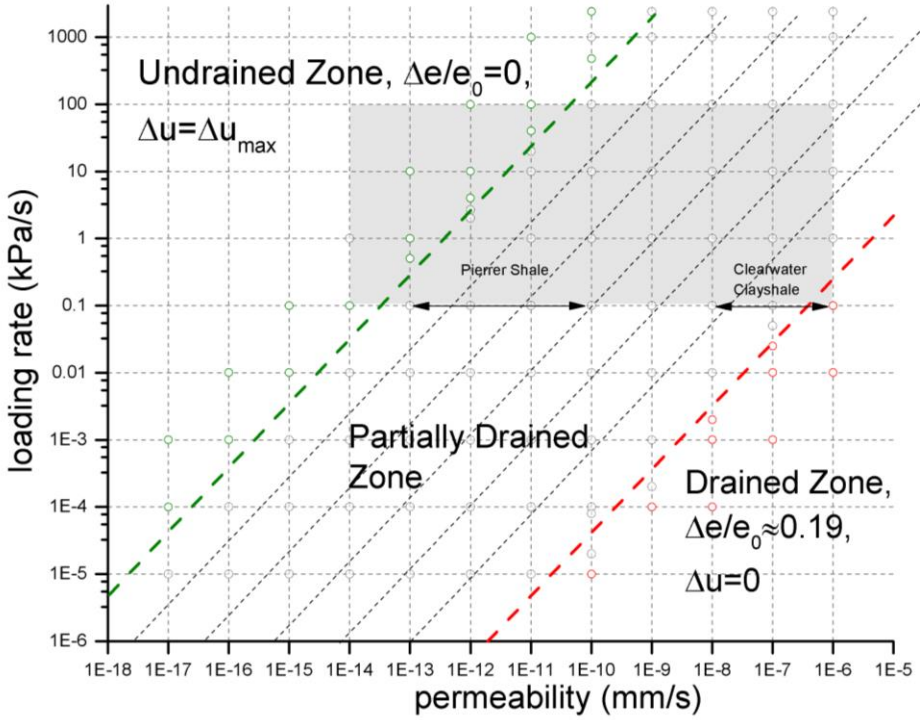

Figure 2-8. Undrained, partially drained and drained zones defined by loading rate and permeability.

It is worth noting that the permeability *k* was assumed constant throughout each expansion. Ideally, *k* should be presented as a specific function of dilation and shear distortion, or, for a computation convenience, a void ratio/porosity dependent function.

The relationship between permeability and void ratio has been widely investigated for shales and other argillaceous rocks at both core scale and regional scale, but it is still not well established. The laboratory permeabilities at similar porosities can vary by a factor of 10^3, since the tortuosity and the size of pores both contribute to the conductivity of fluid channel inside the medium. Also, the structural anisotropy induced by the stratification of argillaceous sediments may heavily influence the permeability measured (Neuzil, 1994). However, based some laboratory results, some empirical functions have been suggested for a rough estimation.

A general function for cohesive material was given by Samarasinghe, (1982) as $k = C_k \left[e^n / (1+e) \right]$. Mesri (1982) suggested that void ratio e is proportional to the logarithm of permeability *k*, i.e, $\Delta \log k = \Delta e / C_k$, in which C_k ranges from 0.5 to 4 for clays and from 0.02 to 0.5 for shales. Cao et al. (1986) and Dutta (1987) refined the relation between permeability *k* and void ratio *e* for shales, written in the form of

$$k = k_0 (e / e_0)^{\beta} \tag{2.6}$$

where β is usually of order 3 ± 3.

For a specific material, it is of interest to know how significantly the value of β in the k-e relationship influences the pore pressure variation and borehole deformation as a consequence of the permeability changes.

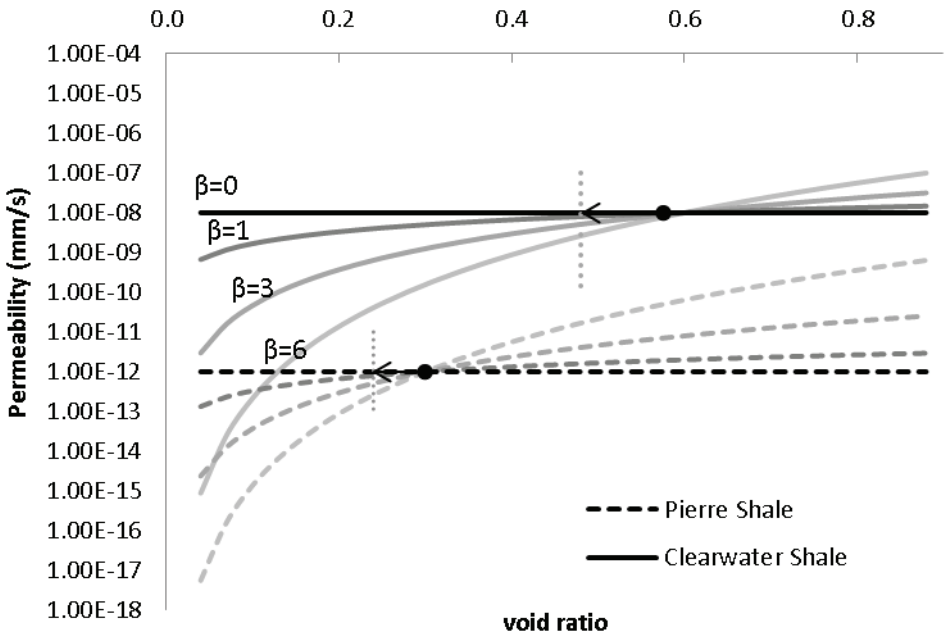

Figure 2-9. Permeability variation as a function of void ratio for two types of shales. e_0=0.3 and $k_0=10^{-12}$ mm/s for Pierre Shale; e_0=0.6 and $k_0=10^{-8}$ mm/s for Clearwater Shale.

According to Figure 2-7, the maximum volumetric change ($\Delta e/e_0 \approx 0.19$) occurs under drained conditions. Assuming that the void ratios of both materials in Figure 2-9 are reduced 19%, permeability will decrease approximately an order of magnitude for the worst case of β =6. However, it is shown in Figure 2-8 that pore water is not likely to fully dissipate in a medium of initial permeability less than 10^{-6} mm/s. Furthermore, loading on a more heavily overconsolidated shale (*OCR*>3) would also attenuate the variation of void ratio and thus the variation of permeability would likely be unnoticeable during the expansion.

Therefore, parameter β has insignificant influence on the expansion behavior and the permeability function can be excluded from the simulation in this case.

2.2 Influence of Borehole Disturbance on Cavity Expansion

In practice, it is not possible to maintain a "perfect" borehole with smooth sides and uniform radius by drilling. Even if the test is with self-bored pressuremeter, the surrounding material would be overpushed and the interpreted properties would not be the true values (Jefferies, 1988). Five errors are usually caused by the borehole imperfections (Fragaszy and Cheney, 1977):

1. finite length of loading;
2. out-of-roundness;
3. variation in radius along the length of the hole;
4. wall-surface roughness; and
5. inhomogeneity of materials near the borehole.

The larger the length-to-radius ratio is the deformation is more approximate to the plain-strain solution. Out of roundness will cause non-uniform convergence and expansion. Wall smoothness is extremely influenced by the mud flushing and borehole washout and different shapes of circumferential notches will form. Fragaszy and Cheney's (1977) study showed that the maximum error of radial displacement caused by the wall roughness is approximately 10% for the general wellbores.

Silvestri (2004) also investigated both overpushing and overcutting effects in pressuremeter testing based on a model to characterize the unloading and reloading behavior. He found that the undrained shear strength might be 100% overestimated for overcutting case while it was underestimated if the borehole is overpushed.

In this paper, an undisturbed shape of borehole is assumed but initial convergence taking place during the unloading of borehole before the

pressuremeter testing is considered. The effect that the drilling-induced deformation has on the interpretation of ground properties will be discussed, which was not within the scope of the study by Fragaszy and Cheney (1977).

2.2.1 Expansion of Yielded Borehole in Differently Consolidated Media

Yielding is likely to occur after the borehole is drilled if the resultant deviatoric stress is high enough to reach the yield surface, i.e.,

$$q_y = M\sqrt{p_0'(p_c' - p_0')} < q = \sqrt{\frac{1}{2}\left[(\sigma_\theta' - \sigma_r')^2 + (\sigma_z' - \sigma_r')^2 + (\sigma_\theta' - \sigma_z')^2\right]} \tag{2.7}$$

where σ_ϑ=2p_0, σ_r=0 and σ_z=p_0 for the rapid excavation of circular opening. Thus, borehole is pre-yielded in the condition that

$$p_c' < \left(\frac{3+M^2}{M^2}\right)p_0' \tag{2.8}$$

In this section M and p_0 are selected as 1.3 and 120kPa respectively for the formulations outlined above, and two scenarios regarding the pre-yielding issues are discussed in the four examples with different overconsolidation ratios ($OCR = \frac{p_c'}{p_0'}$) considered.

A brehole has a slight convergence if the excavation is made in heavily/moderately overconsolidated formations (Figure 2-10). Elastic deformation during the unloading of the borehole produces little change of pore pressure. Thus, the total stress path and effective stress path will have nearly the same trajectory. As the radial stress at borehole wall is totally removed, the tangential stress increases to double initial stress, so the mean stress will remain constant inside the yield surface. The subsequent relaxation after drilling completion allows the drainage of pore water towards the far field boundary.

However, it will have unnoticeable effect on the stress path due to the small amount of excess pore pressure remaining after drilling.

The quick expansion of the packer against the wall increases the radial stress and decreases tangential stress in the same magnitude. As the deviatoric stress keeps reducing, the stresses will be reversed in the order from $\sigma'_r > \sigma'_\vartheta$ to $\sigma'_\vartheta > \sigma'_r$ (σ'_z remains as intermediate stress in the whole process) at some point of expansion. The stress trajectory will hit the yield surface and plastic deformation occurs in the way defined by the associated flow rules until it ultimately reaches the critical state line. The stress distribution gives the same pattern found by Collins and Yu (1996), Cao et al., (2001) and Abousleiman and Chen (2012) regarding the different overconsolidation ratios of materials.

Drilling in the lightly consolidated formations or unconsolidated formations will result in the same deviatoric stress if the initial stress condition is constant (Figure 2-11). However, the material will exhibit strain-hardening behavior after stress trajectory reaches the yield surface. Significant excess pore pressure is generated after yielding, but will dissipate completely in the relaxation period. At the cavity wall, negative pore pressure has been diminished due to the drainage, which leads to the decrease of mean stress and the increase of void volume, and the stress trajectory moves inward to a smaller yield surface. This not only moves the front stress locus from the wet side to the dry side of critical, but also rearranges the stress path for all elements, and will end up at different critical states. The radial displacement of cavity is the integral of deformations at finite points in the radial direction. Thus, there is no unambiguous way to calculate the wall convergence if all the points undergo the different stress paths.

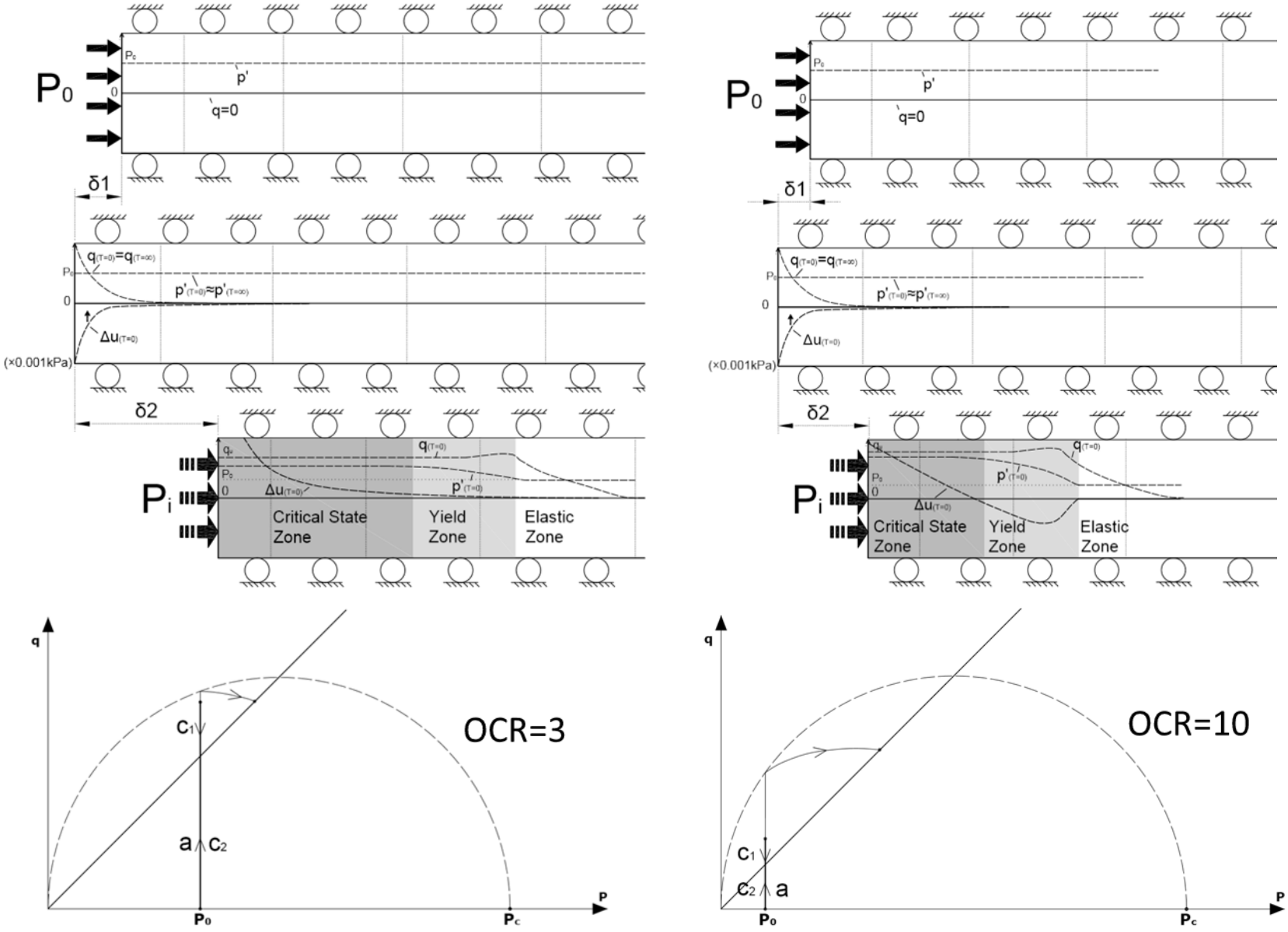

Figure 2-10. The effective mean stress and excess pore pressure profile during the cavity expansion in the unyielded elements of the heavily consolidated soils. The effective stress path at r=0 is shown below.

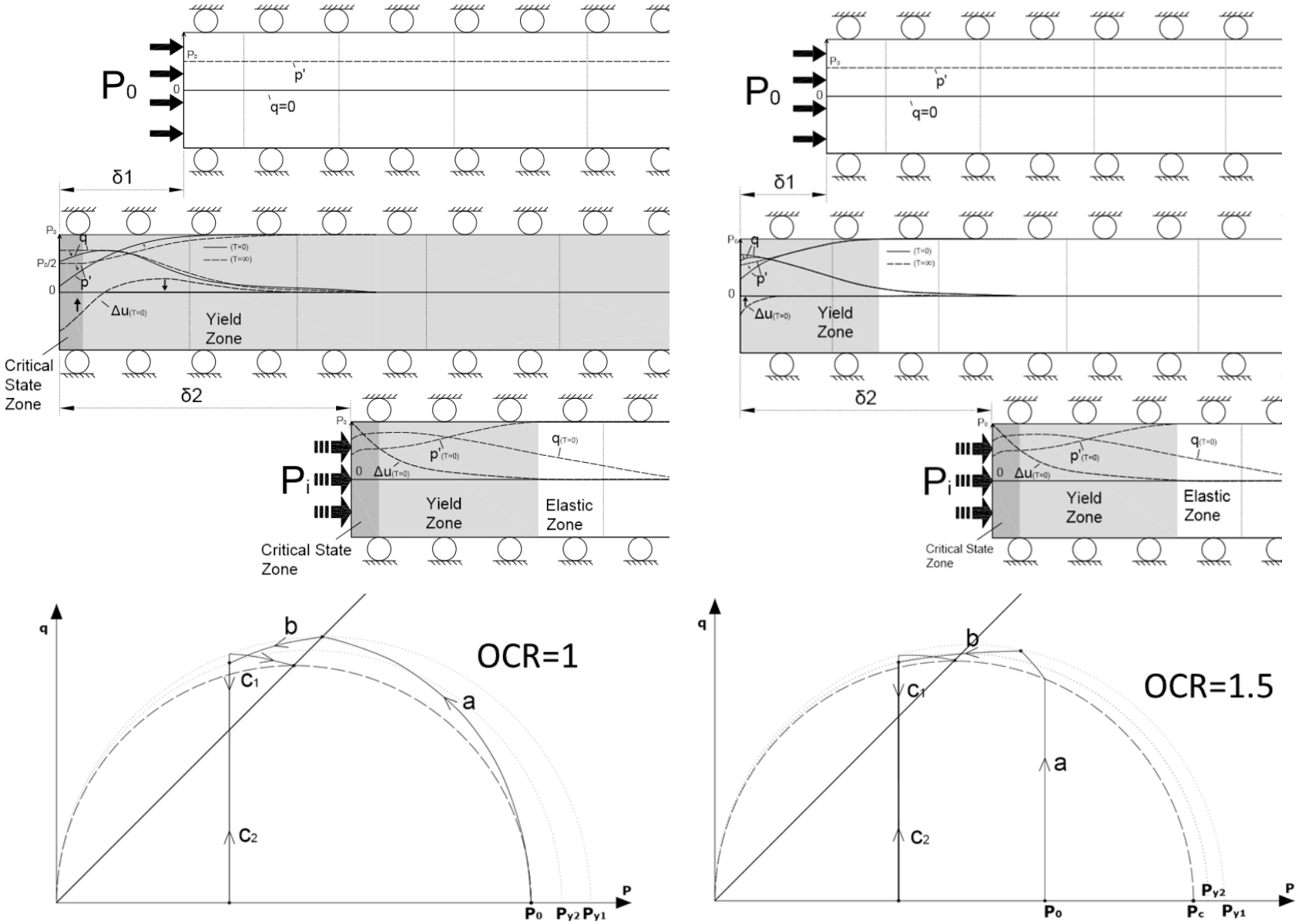

Figure 2-11. The effective stress and excess pore pressure profiles during the cavity expansion in the yielded elements of the lightly consolidated or normally consolidated soils. The effective stress path at r=0 is shown below.

The excess pore pressure at a specific location is independent of that at other points, but it is still hard to predict its final response as drainage induces the uncertainty of stress loci for the undrained expansion followed. Also, it should be mentioned here that the pre-yielding and relaxation for the poorly consolidated materials lead to the non-homogeneous fields of stress, which will possibly cause locally high hydraulic gradients and partial consolidation even in what is supposed to be, or interpreted to be an undrained expansion (Wroth, 1984).

2.2.2 Response at Borehole Surface

The unloading of the formation would affect the properties of borehole materials if yielding has been triggered. The pore pressure and radial displacement both increase with the increase of expansion pressure P_i in the yielded element (Figure 2-12). This response is more remarkable in the less consolidated formations while it is insensitive to the OCR in the intact formation. The dotted line in Figure 2-12 shows the response of excess pore pressure and deformation for the materials under the active loading ($\sigma'_r \leq \sigma'_\vartheta$). When $P_i/P_0 \leq 1$, the mean effective stress remains constant, and according to Eqn(1.12) the shear modulus is independent of P_i. Thus, in this case, Δu_{pore} is predictable if the radial displacement of borehole wall is measured. Examination of this behavior is outside the scope of this research and will not be discussed.

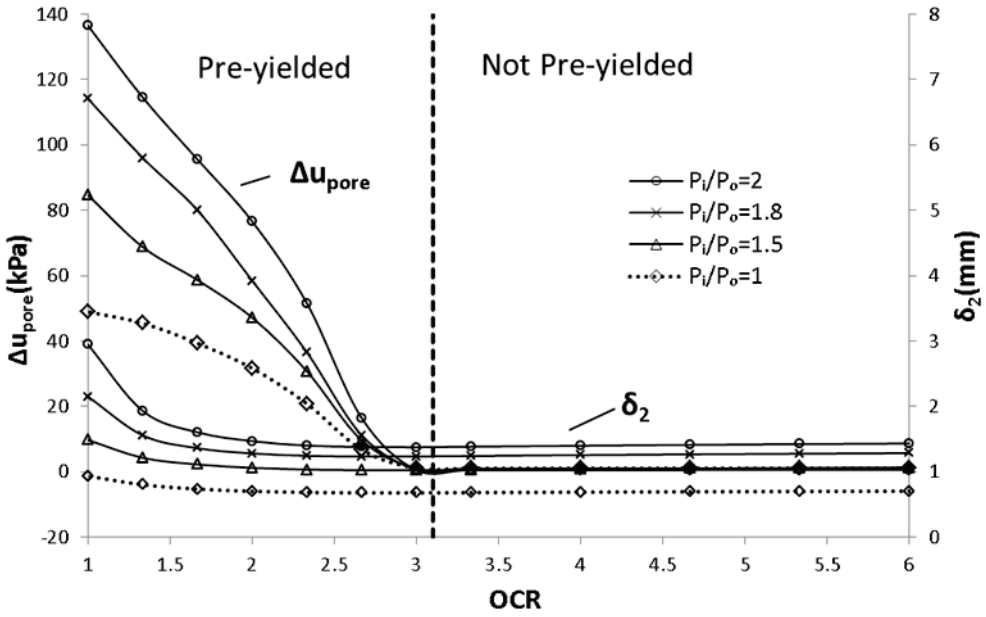

Figure 2-12. The excess pore pressure and radial displacement as a result of given loading after borehole relaxation for formations of different OCRs.

3 Deep Borehole Convergence under Non-uniform Horizontal Loadings

3.1 Theoretical Basis

3.1.1 Mathematical Formulation for Stress and Deformation in Polar Coordinate

The elastic solution for the circular opening has been widely applied to assessing borehole stability with a specified strength criterion by drilling engineers. It has been derived by defining radial and tangential stresses as a function of angle ϑ and radius r in a polar coordinate system in the plain strain condition (Kirsch, 1988)(Figure 3-1).

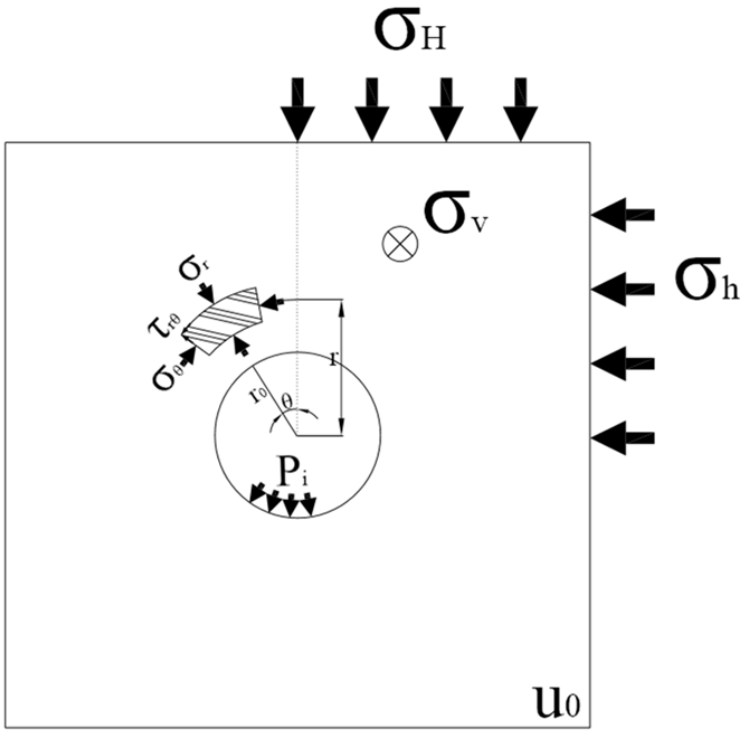

Figure 3-1. Geometry of Kirsch's solution for the stress concentration around a circular opening under anisotropic stress condition.

The fundamental governing equations are

$$\frac{\partial \sigma_{rr}}{\partial r}+\frac{1}{r}\frac{\partial \sigma_{r\theta}}{\partial \theta}+\frac{\sigma_{rr}-\sigma_{\theta\theta}}{r}=0$$
$$\frac{\partial \sigma_{r\theta}}{\partial r}+\frac{1}{r}\frac{\partial \sigma_{\theta\theta}}{\partial \theta}+2\frac{\sigma_{r\theta}}{r}=0 \qquad (3.1)$$

Considering the pore fluid effect, the Kirsch's solution could be expressed in the form of (Zoback, 2010):

$$\sigma'_{rr}=\frac{\sigma_H+\sigma_h-2u_0}{2}\left(1-\frac{r_0^2}{r^2}\right)+\frac{\sigma_H-\sigma_h}{2}\left(1-\frac{4r_0^2}{r^2}+\frac{3r_0^4}{r^4}\right)\cos 2\theta+\Delta \mathrm{P}_i\frac{r_0^2}{r^2}-\Delta u(r)$$
$$\sigma'_{\theta\theta}=\frac{\sigma_H+\sigma_h-2u_0}{2}\left(1+\frac{r_0^2}{r^2}\right)-\frac{\sigma_H-\sigma_h}{2}\left(1+\frac{3r_0^4}{r^4}\right)\cos 2\theta-\Delta \mathrm{P}_i\frac{r_0^2}{r^2}-\Delta u(r) \qquad (3.2)$$
$$\sigma'_{zz}=\sigma_v-u_0-\Delta u(r)-\nu\frac{4r_0^2}{r^2}\frac{\sigma_H-\sigma_h}{2}\cos 2\theta$$

where ΔP_i is the difference pressure between mud and the pore water on the cavity wall and u_0 is the initial pore pressure. If it is undrained, the generated excess pore pressure is expressed as

$$\Delta u(r)=B\frac{\Delta\sigma_{kk}(r)}{3}=-\frac{2}{3}(\sigma_H-\sigma_h)B\cos(2\theta)\frac{r_0^2}{r^2}(1+\nu) \qquad (3.3)$$

where B could be determined either theoretically (Rice and Cleary, 1976) or experimentally (Skempton, 1954) and the Poisson's ratio ν is equal to 0.5 for the incompressible soils . Δu and the change of polar principal stresses ($\Delta\sigma_r$, $\Delta\sigma_\vartheta$ and $\Delta\sigma_z$) are rigorously coupled; by applying numeric approach, the poroelastic response of borehole either under drained or undrained conditions could be found (Detournay and Cheng, 1988).

Eqn(3.3) implies that excess pore pressure may significantly influence the effect stress paths if drainage occurs. Figure 3-2 shows that the high deviatoric stress at the azimuth of σ_h ($\vartheta=0$) may trigger the shear failure immediately after the

drilling. At the azimuth of σ_H *(ϑ=π/2),* the reduced mean effect stress may also induce the shearing during the consolidation at the borehole wall.

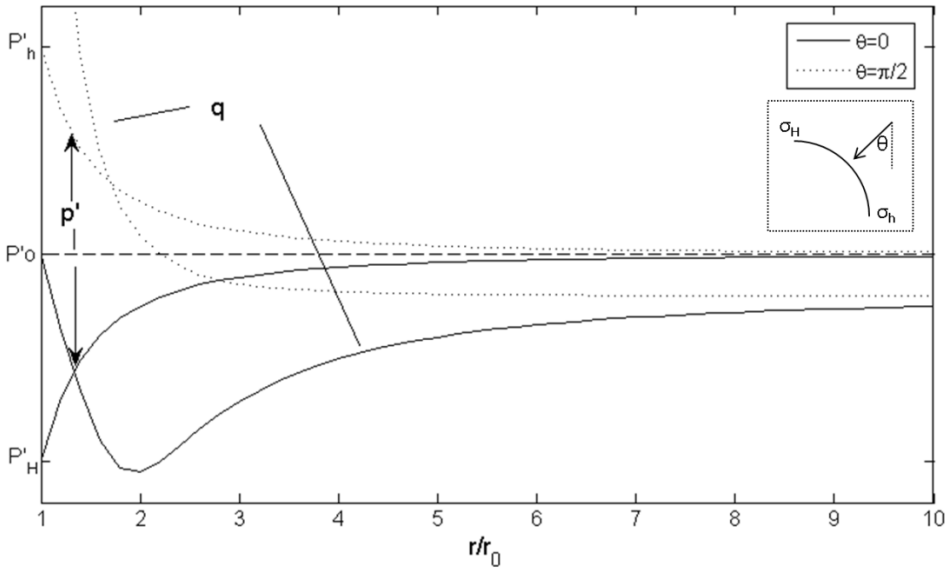

Figure 3-2. Variations of effective stresses for pore water dissipation. p'_0 is the initial effective mean stress and p'_h and P'_H are the mean effective stress at the orientations of σ_h and σ_H respectively.

p'_h and p'_H are the functions of virgin stresses

$$p'_h = (p_0 - u_0) + 2(1+\upsilon)(\sigma_H - \sigma_h)$$
$$p'_H = (p_0 - u_0) - 2(1+\upsilon)(\sigma_H - \sigma_h) \quad (3.4)$$

Figure 3-3 gives stress paths at two azimuths around the wellbore. Although shear failure is most likely to occur at the azimuth of σ_h, the risk would be reduced after the pore water dissipates. The stress trajectory gets closer to the yield surface ***"a"*** and strain hardening may take place especially for poorly consolidated material. If the formation is heavily consolidated, stress trajectory at the azimuth of σ_h may hit the yield surface ***"b"*** and it has the potential of softening afterwards.

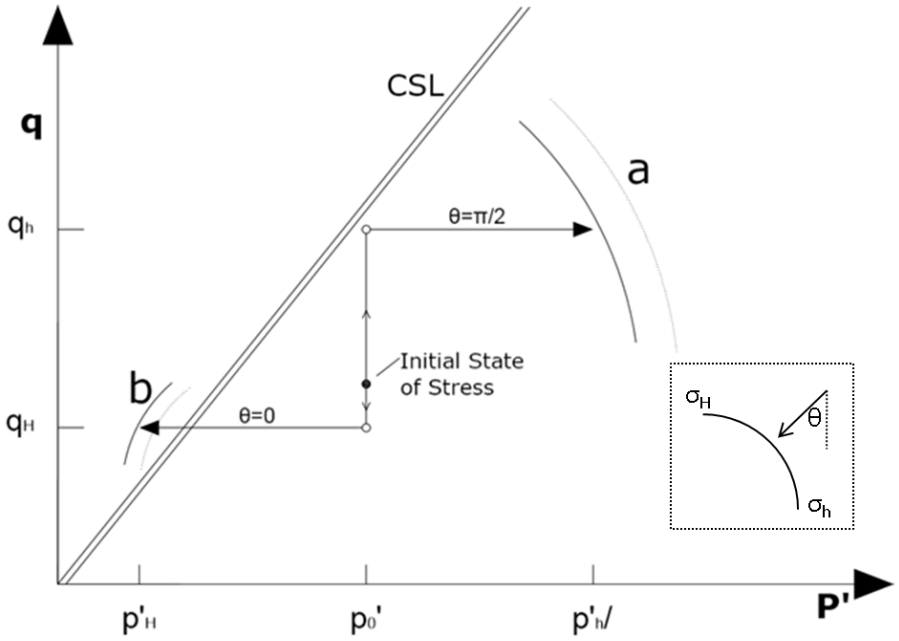

Figure 3-3. Effective stress paths during elastic consolidation after drilling

The strains are also in the form of polar coordinates,

$$\begin{aligned}\varepsilon_{rr} &= \partial\delta_r/\partial r \\ \varepsilon_{\theta\theta} &= \delta_r/r + (1/r)(\partial\delta_\theta/\partial\theta) \\ \varepsilon_{\theta r} &= \partial\delta_r/\partial r + (1/r)(\partial\delta_r/\partial\theta) - \delta_\theta/r\end{aligned} \tag{3.5}$$

where δ_r and δ_ϑ are the displacements in the radial and circumferential direction and the volumetric strain $\varepsilon_v = \varepsilon_{rr} + \varepsilon_{\theta\theta}$. The constitutive relations between the stress and strain are

$$\begin{aligned}\sigma_{rr} - (\Delta u + u_0) &= -\frac{2G\nu}{1-2\nu}\varepsilon_v - 2G\varepsilon_{rr} \\ \sigma_{\theta\theta} - (\Delta u + u_0) &= -\frac{2G\nu}{1-2\nu}\varepsilon_v - 2G\varepsilon_{\theta\theta} \\ \sigma_{r\theta} &= -G\varepsilon_{r\theta}\end{aligned} \tag{3.6}$$

Rewriting Eqn(3.1) with the expression of stress tensors in Eqn(3.6) and substituting them with the strain tensors given by Eqn(3.5), we arrive at

$$\frac{2G(\nu-1)}{2\nu-1}\left(\frac{1}{r}\frac{\partial^2\delta_r}{\partial r\partial\theta}+\frac{\partial^2\delta_r}{\partial r^2}+\frac{1}{r}\frac{\partial\delta_r}{\partial r}-\frac{1}{r^2}\frac{\partial\delta_\theta}{\partial\theta}-\frac{\delta_r}{r^2}\right)-\frac{G}{r^2}\left(r\frac{\partial^2\delta_\theta}{\partial r\partial\theta}+\frac{\partial^2\delta_r}{\partial\theta^2}+\frac{\partial\delta_\theta}{\partial\theta}\right)=\frac{\partial(\Delta u)}{\partial r}$$
$$\frac{2G(\nu-1)}{r^2(2\nu-1)}\left(r\frac{\partial^2\delta_r}{\partial r\partial\theta}+\frac{\partial^2\delta_\theta}{\partial\theta^2}+\frac{\partial\delta_r}{\partial\theta}\right)+\frac{G}{r^2}\left(r\frac{\partial^2\delta_r}{\partial r\partial\theta}+r^2\frac{\partial^2\delta_\theta}{\partial r^2}+r\frac{\partial\delta_\theta}{\partial r}-\frac{\partial\delta_r}{\partial\theta}-\delta_\theta\right)=\frac{\partial(\Delta u)}{\partial r} \quad (3.7)$$

It would be concluded from Eqn(3.3) and Eqn(3.7) that both the responses of wall displacements and pore pressure variation of borehole are independent of the initial vertical stresses if the constitutive properties G and μ both remain constant. However, as shown in Eqn(1.6), G and μ are interrelated with mean stress p' and specific volume v according to the Cam Clay postulate. Thus, σ_v changes the initial shear modulus G_0 via changing p' and v for the same kind of formations. As a result, σ_v has the impact on the borehole convergence while pore pressure is the function only of σ_H and σ_h.

3.1.2 Influence of Mud Pressure

For a vertically oriented borehole in a fluid saturated medium, an optimum drilling fluid density is required to balance the formation pressure and prevent borehole yielding. The filter cake usually forms in the mud circulation with a considerable permeability which allows excess pore pressure to be dissipated. The filter efficiency is given by the ratio of pore pressure inside the borehole wall p_a and the drilling fluid or mud pressure p_i, i.e., $\eta=\frac{p_a}{p_i}$. The comparison of near-well pore pressure profiles with respect to η is shown in Figure 3-4. High mud density leads to the overbalanced radial pressure $p_{i,ob}$ on the borehole wall while low mud density has weak resistance towards the inward flow and erosion may take place at borehole wall. In this research, an optimum mud density is assumed and the in-balance internal pressure presents no hazard to the borehole stability. It should be noted that for the results shown in Figure 3-4 pore pressure equilibrium will occur only after long term borehole pressurization

or depressurization, while the short-term transition of pore pressure when the loading P_i is immediately applied will be discussed later.

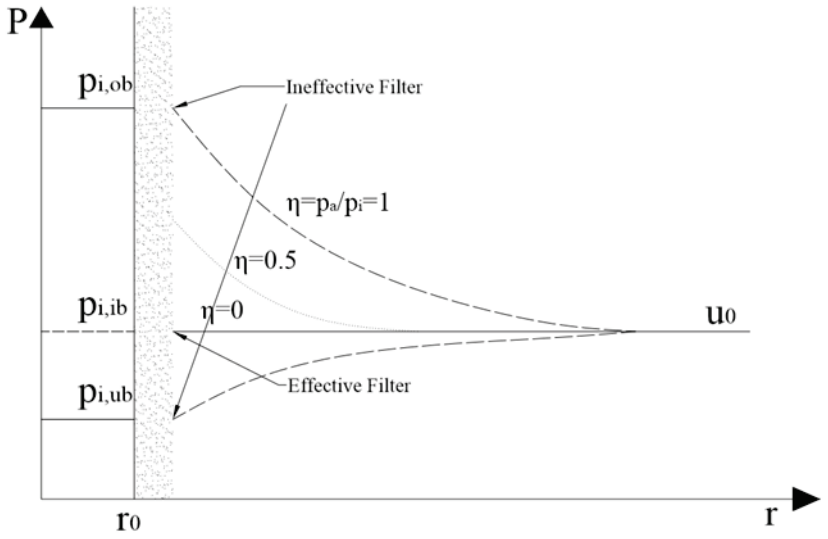

Figure 3-4. The pore pressure profile when different types of filter cakes are present.

3.1.3 Geostatic Stresses

Eqn(3.2) can be rewritten in the form of effective pressure with the dimensionless variable of $\bar{K} = (\sigma'_h + \sigma'_H)/2\sigma'_V$ and $N = (\sigma'_H/\sigma'_h)$ after a long term consolidation under the in-balanced wellbore pressure:

$$\begin{aligned}
\sigma'_r &= \bar{K}\sigma'_V\left(1-\frac{r_0^2}{r^2}\right)+\left(\frac{N-1}{N+1}\right)\bar{K}\sigma'_V\left(1-\frac{4r_0^2}{r^2}+\frac{3r_0^4}{r^4}\right)\cos 2\theta \\
\sigma'_\theta &= \bar{K}\sigma'_V\left(1+\frac{r_0^2}{r^2}\right)-\left(\frac{N-1}{N+1}\right)\bar{K}\sigma'_V\left(1+\frac{3r_0^4}{r^4}\right)\cos 2\theta \\
\sigma'_z &= \sigma'_V\left[1-\nu\,\frac{4r_0^2}{r^2}\left(\frac{N-1}{N+1}\right)\bar{K}\cos 2\theta\right]
\end{aligned} \tag{3.8}$$

Theoretically, the value of *N* can be very high if the material is strong enough, and the range of possible values of $\bar{K}$ is also quite wide (Goodman, 1989). Based

on a large number of datasets, a relation between $\overline{K}$ and depth *Z* was empirically defined by Brown and Hoek (1978), Since the scope of this study is limited to clayshale at shallow surface layer (100<*Z*<500), according to Eqn(3.9) let $\overline{K}$ be in the range from 0.5 to 2.

$$0.3+\frac{100}{Z}<\overline{K}<0.5+\frac{1500}{Z} \tag{3.9}$$

The critical state line in p-q domain could be also expressed in terms of friction angle ϕ specified in the Mohr-Coulomb theory if the cohesion is negligible, written as

$$M=\frac{6\tan\varphi}{3\sqrt{\tan\varphi^2+1}-\tan\varphi} \tag{3.10}$$

The magnitudes of initial stresses could be further restricted by stress polygon introduced by Moos and Zoback (1990) and it provides a good estimate of the possible range if one of the stresses is known. Figure 3-5 shows the possible stress regimes in this study within different constraints. It is observed from the case of *M*=1 (ϕ ≈25°), the stress polygon limits the stress magnitudes into a small range (Figure 3-5, right). Whereas, it may not be applicable to the argillaceous sediments like clayshale in which cohesive bonding is present. The stress anisotropy can increase significantly for those sediments as long as they have been considerably consolidated or undergone the process of diagenesis, (e.g.cementation) in their geologic history (Bjerrum and Wu, 1960). For most soft rock at shallow depths, the stress states are located inside the yield surface defined by overconsolidation ratio ranging up to 6 (Gutierrez et al., 2008). Thus, a reasonable range of the horizontal stress anisotropy *N* is from 1 to 3 in accordance with 0.5<$\overline{K}$<2 (Figure 3-5, left).

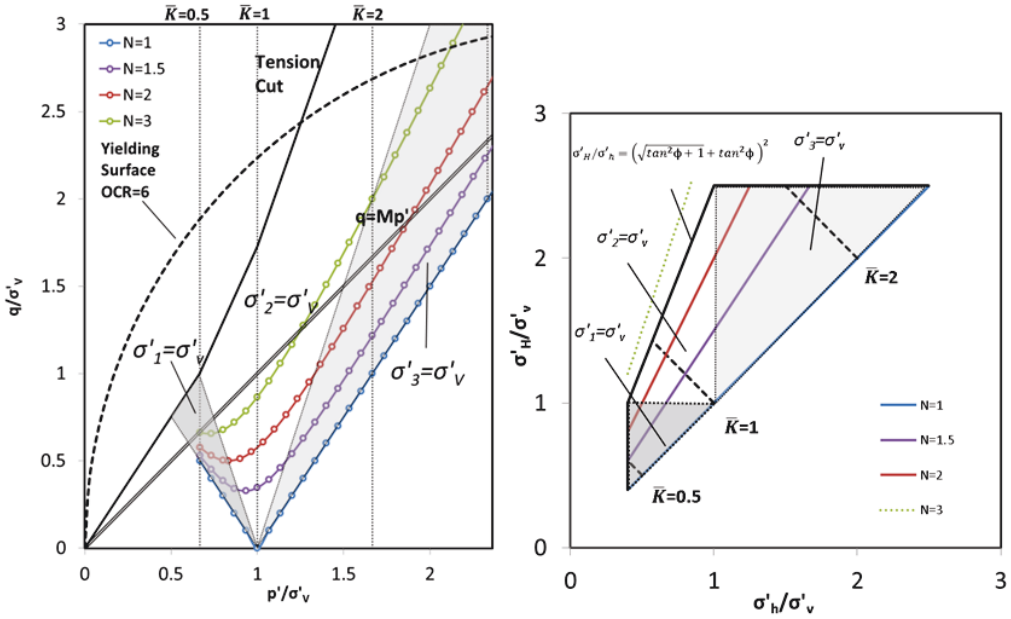

Figure 3-5. The distribution of initial stresses in the p-q space and stress polygon

An important assumption inherent in the solution for the plastic deformation in the cavity problem is that the out-plane stress always remains as intermediate stress and thus is not excluded in the yielding criteria that only takes into account two in-plane stresses. Figure 3-6 shows the principal stresses vary over different azimuths. Clearly, the vertical stress may become the maximum principal stress (shaded area in Figure 3-6) near the azimuth of θ=0° or θ=180° especially for low Poisson's ratio material or in the condition of $\sigma_H \approx \sigma_v >> \sigma_h$. In this case, two different functions of plastic potential should be employed to calculate the plastic deformations, if the yielding criterion is dominated by two principal stresses, e.g., Mohr Coulomb or Hoek Brown criterion (Reed, 1988). This, inevitably, increase the difficulties of finding the post-yielding solution whether by analytical or numerical methods. The MCC model mentioned above which takes into account the magnitudes of all the principal stresses with a single yield function becomes more suitable to this case of problem.

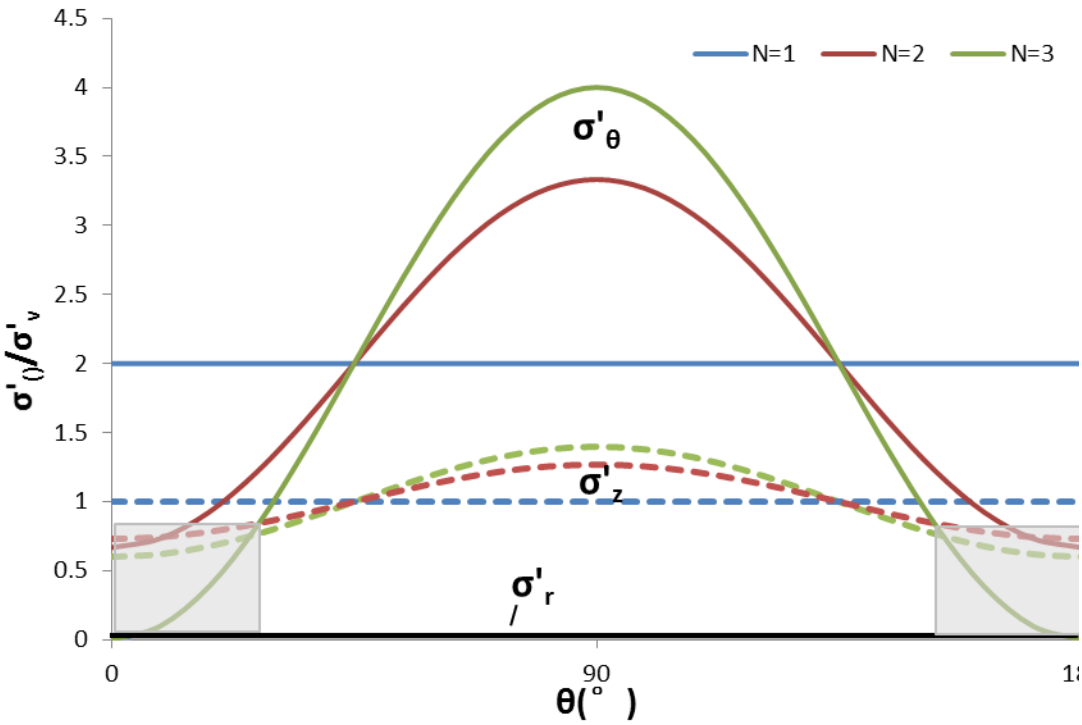

Figure 3-6. The distribution of stresses around the unsupported cylindrical cavity in the elastic medium. $\bar{K}$=1, v=0.2.

Let the yield function $f(q, p, p_c)$ be equal to 0 and find the equivalent isotropic preconsolidation pressure p'_{c0} for the virgin stress state,

$$p'_{c0} = q'^2_0 / M^2 p'_0 + p'_0 \tag{3.11}$$

Also, if the preconsolidation pressure p'_c is known, the corresponding yield stress could be calculated by yield function,

$$q_y(\theta) = \sqrt{M^2 p'(p'_c - p_0)} \tag{3.12}$$

Then an isotropic overconsolidation ratio can be defined with the maximum isotropic preconsolidation pressure in the loading history (Wood, 1990),

$$n_p = \frac{p'_c}{p'_{c0}} \tag{3.13}$$

Figure 3-7 shows the change of mean stress and deviatoric stress as a consequence of drilling. Almost in all the stress regimes, the resultant deviatoric stress has a significant increase and exceeds the allowable value defined by the yield function in the case of normally consolidation ($n_p=1$). For the soils which have a considerable strength or moderately consolidated ($n_p>1$), drilling may not cause the instability at the cavity vicinity and it becomes important to determine the threshold of n_p (designated as $n_I=p'_y/p'_{c0}$) at which borehole yielding is prevented (shown by red dotted curve). In all the cases, the wellbore has the highest risk of yielding at the azimuth of minimum horizontal stress.

Eqn (3.8) indicates that as N increases, the deviatoric stress increases and borehole is sheared at the azimuth of σ'_h. However, Figure 3-8 shows materials with the same overconsolidation ratio n_p may not necessarily fail under the condition of the highest initial horizontal stress anisotropy. Also, the comparison of the values of n_I in different stress regimes shows that borehole will be more stable when σ'_v is the maximum principal stress than when it is the minimum principal stress for the same horizontal stress anisotropy. This also suggests that wells drilled normal to maximum principal stress orientation should be generally avoided. The deviatoric stress q for the case of $\sigma'_H \geq \sigma'_v \geq \sigma'_h$ varies slightly at different azimuths. This can also be problematic especially for poorly consolidated materials because a wide arc of failed zone may form as a result.

The isotropic preconsolidation pressure p'_y at yield is plotted as a contour of N and $\overline{K}$ in Figure 3-8. If the general stress anisotropy $\overline{K}$, horizontal stress anisotropy N and the preconsolidation pressure p'_c are given, then the possibility of borehole yielding can be predicted by finding the corresponding point in Figure 3-8. In the other way around, if we are able to estimate the borehole

conditions based on the well log (yielded or unyielded), we are able to constrain the estimation of $\overline{K}$ and *N* and find the stress regimes in the same figure.

It's worth noting that Figure 3-8 is only applicable to the material with known value of *M.* A stochastic study on the constants *M* and *v* shows that the magnitude of M has a considerable influence on the distribution of the contour while *v* has a negligible effect.

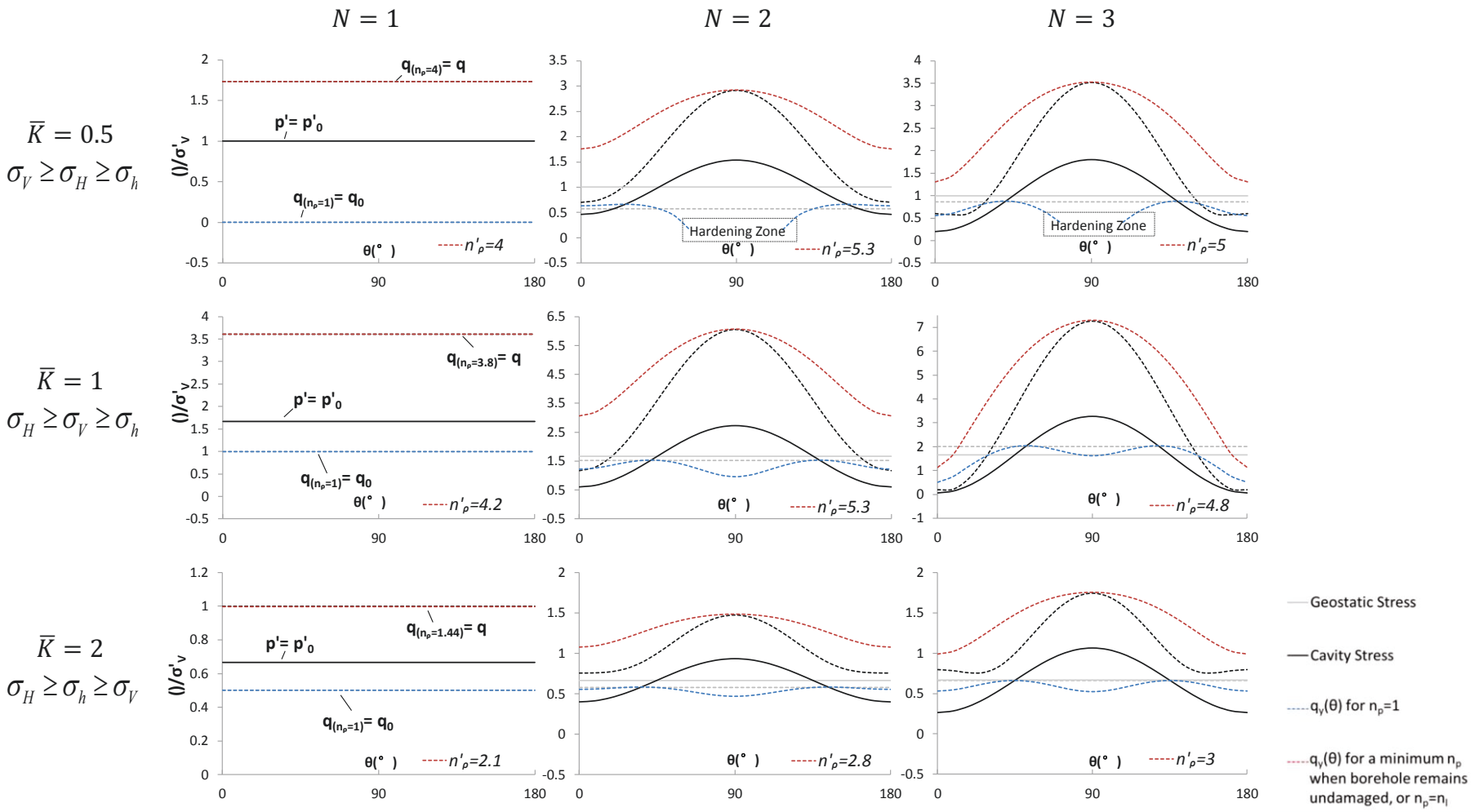

Figure 3-7. Azimuthal variations of mean stress p' (solid line) and deviatoric stress q (dotted line) at cavity wall compared with yield strengths calculated from the hypothesized isotropic overconsolidation ratio n_p. Hardening zone indicates $p' > p'_{c0}$ and the yield surface is enlarged by certain amount

.

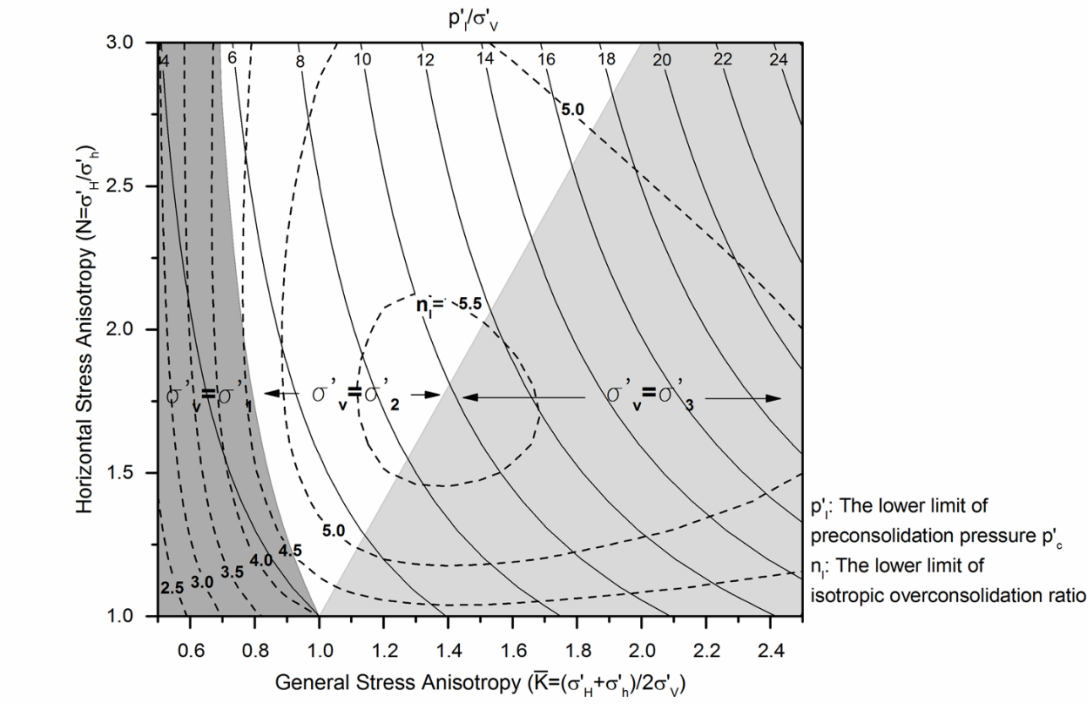

Figure 3-8. The drilling-induced yielding/damage constrained by boundary stress magnitude and preconsolidation pressure of insitu material.

3.2 Deformation of Borehole after Drilling

A numerical model was developed to simulate the instantaneous and long-term deformation of borehole after the drilling. Due to symmetry in the horizontal plane, a model of the quarter geometry of a 101 mm (4 in.) borehole was established for the computational efficiency (Figure 3-9).

The ratio of the radius of borehole to the length of the model is 1:40 so that the excavation minimally influences the far field boundary. The formation property constants used in this study are listed in the Table 3-1, where Γ is the special volume at the Critical State Line (CSL) when p=1kpa.

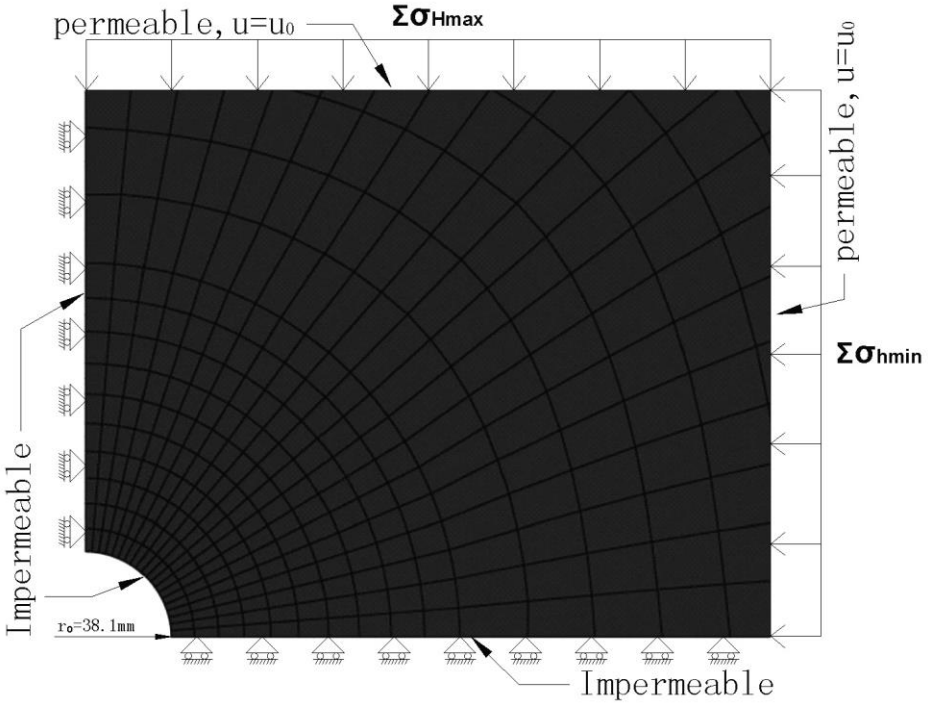

Figure 3-9. The plane strain model for the pocket excavation with the balanced mud pressure (The outside boundaries are partially present)

The elastic deformation and plastic deformation after the yielding have been separately evaluated by investigating the radial displacement and pore pressure changes at the cavity annulus as a function of the relaxation time.

Table 3-1. The Cam Clay constants of Clearwater clayshale

Γ	λ	κ	M	Y'(kN/m3)	ν
2.19	0.075	0.03	1.0	17.0	0.22

3.2.1 Elastic Deformation of Borehole

Purely elastic deformation takes place if the formation has considerable strength compared to the ground stress. Figure 3-10 presents the evolution of cavity shapes when the drainage occurs for four horizontal stress anisotropies.

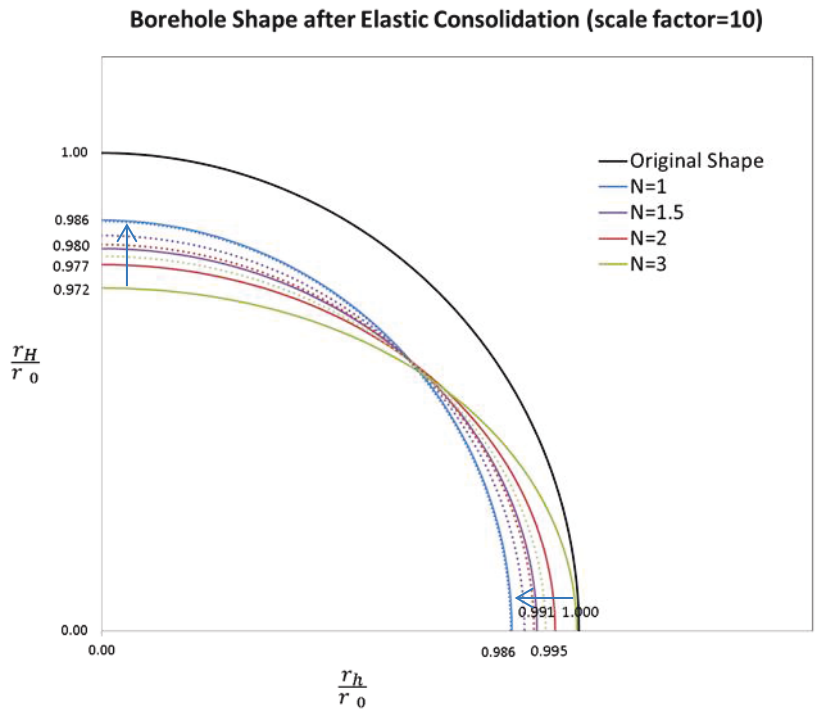

Figure 3-10. Elastic deformation of borehole at the depth of 200m. The solid lines and dotted lines distinguish the borehole shapes at the instance of drilling and after a sufficient time of consolidation.

The cavity continues deforming after drilling because a great amount of excess pore pressure are generated and the consequent dissipation of pore water leads to the effective stress changes of soil matrix over the course of time. This time-dependent deformation could also take place "chemically" but in the assumption of chemically inert drilling fluids, only the mechanical behavior is considered in this research.

In order to generalize the solution regardless of the material properties and elapsed time, the radial displacement changes during consolidation are plotted as the dimensionless form $\hat{\delta}_r$ against the dimensionless form of time $\hat{t}$, as suggested by Carter (1982) (Figure 3-11). The variation of pore pressure is also shown in the dimensionless form with time in Figure 3-12. The dimensionless expressions are given in Eqn (3.14). Excess pore water pressure is generated non-uniformly at the cavity circumference. The dissipation of positive pore pressure

results in the increase of the mean effective stress, and consequently, the formation becomes more compacted in the direction of the minimum horizontal stress. By contrast, along the maximum horizontal stress, materials which have been initially unloaded at the onset of drilling continue dilating until steady state is reached.

$$\begin{aligned} \Delta\hat{u}_{pore} &= \frac{\Delta u}{\bar{K}\sigma'_V} \\ \hat{\delta}_r &= \frac{G_0\delta_r}{\bar{K}\sigma'_V r_0} \\ \hat{t} &= \frac{C_h t}{r_0^2} = \frac{2G_0 kt}{r_0^2\gamma_w}\left(\frac{1-\nu}{1-2\nu}\right) \end{aligned} \tag{3.14}$$

where C_h is the consolidation coefficient. It is worth noting that the equivalent time t at the end of consolidation is also a function of initial shear modulus and permeability of formations. The soft shale with low permeability may have an extremely long consolidation time (e.g., it takes approximately 2 days for a 3 inches borehole under the same conditions to sufficiently consolidate in the formation of Pierrer Shale ($k_{h,max}\approx10^{-13}$ m/s), and it would take months for those with bigger borehole diameters and lower permeability). In this case, sufficient time should be allocated to let the excess pore pressure dissipate. The residual excess pore pressure within the medium from an incomplete consolidation would complicate boundary conditions for a subsequent pressuremeter test.

The cavity becomes non-circular under the non-uniform boundary loadings. Figure 3-11 also shows that with the increase of the initial horizontal stress anisotropy, the borehole is severely distorted at two major horizontal axes (θ=0°and 90°). Steady state is reached at approximately $\hat{t}$=4.

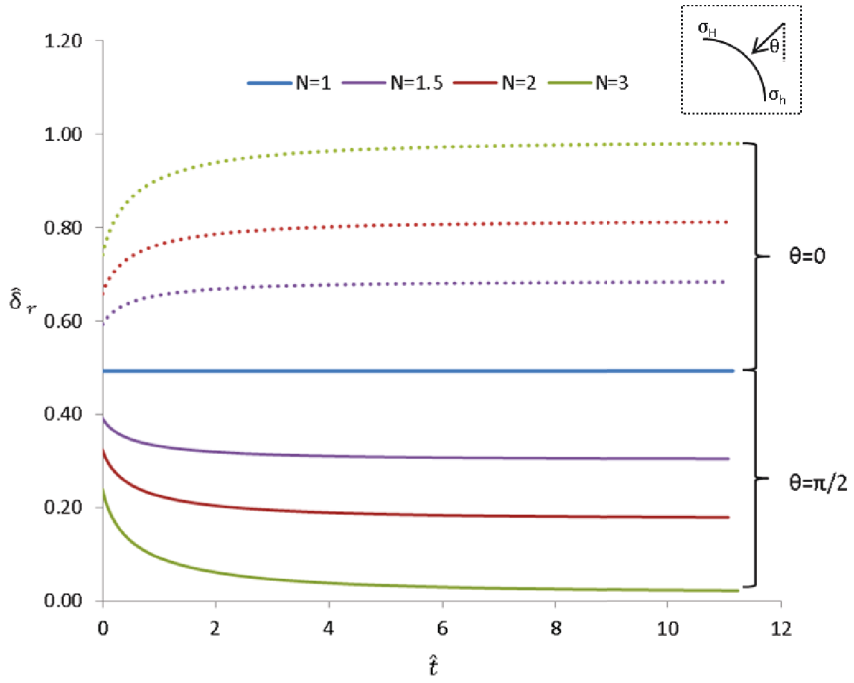

Figure 3-11. The variation of radial displacement during the elastic consolidation at azimuths of σ_H and σ_h

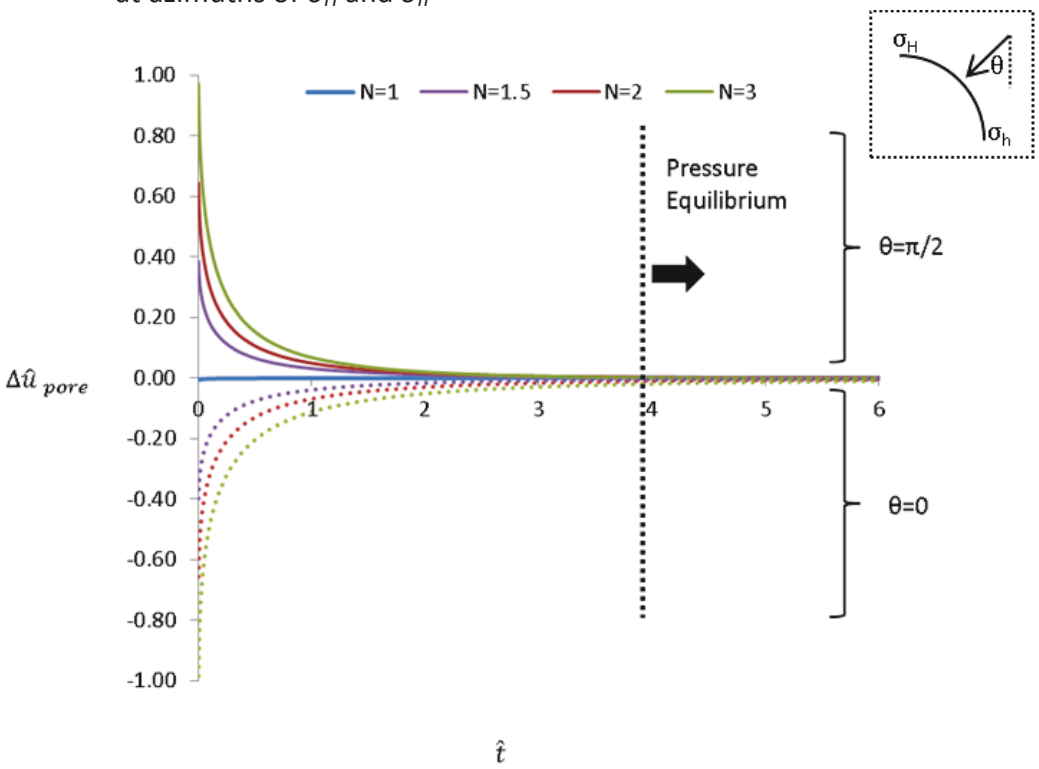

Figure 3-12. The variation of pore pressure during the elastic consolidation at azimuths of σ_H and σ_h

3.2.2 *Plastic Deformation of Borehole*

According to Figure 3-8, for the case of $\overline{K}$=0.5, if $p'_c < 2\sigma'_V$, plastic deformation will take place after the wellbore is drilled regardless of the horizontal stress anisotropy.

The same numerical model was employed to investigate the plastic deformation with a lower value of p'_c equal to 5 MPa. The deformed borehole shape is shown in Figure 3-13. Unlike the elastic deformation, the convergence of borehole will be more irregular especially for higher value of N, as the post-peak dilation takes place after high tangential stress shears the borehole at the orientation of minimum horizontal stress.

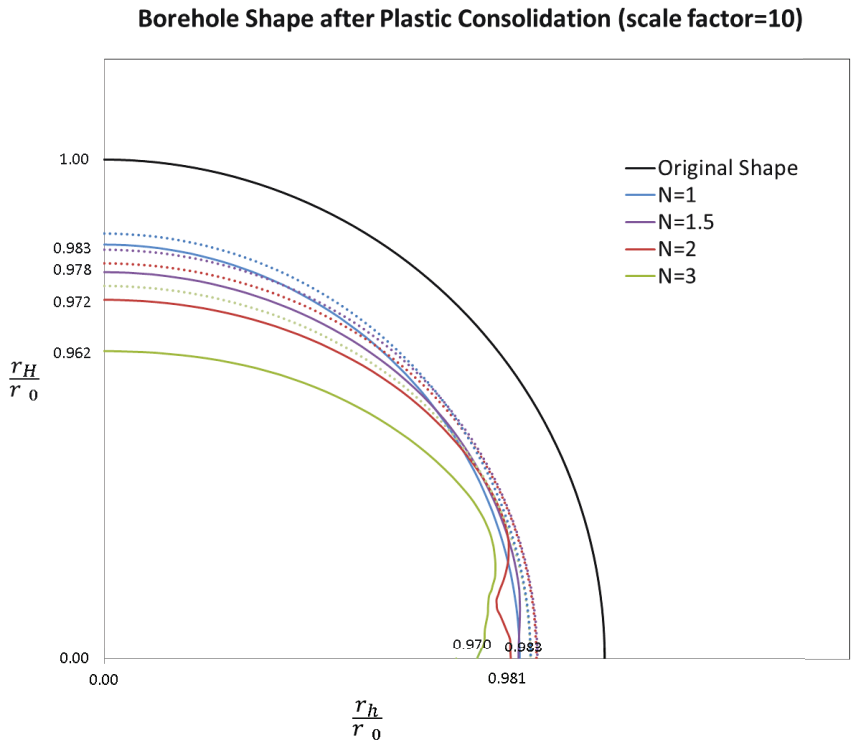

Figure 3-13. Elasto-Plastic deformation of borehole at the depth of 200m with the average earth coefficient $\overline{K}$=0.5. The solid lines and dotted lines distinguish the borehole shapes at the instance of drilling and after a sufficient time of consolidation.

In Figure 3-14, the induced plastic zones in this study are compared with three categories of typical excavation-damaged zones proposed by Detournay and St. John (1988) (Figure 3-14, lower left). The simulation results are consistent with plastic zone development along the bisectrix between two principal horizontal stresses under high initial stress anisotropy.

Figure 3-5 shows whether for cases of $\overline{K} \leq 1$ or OCR>3, the initial stress state is located on the "dry" side of the yield loci, where the dilation is most likely to occur once the material is sheared. An alternative shearing mode is the compaction or "pore collapse" (Schutjens and Hanssen, 2004) which takes place on the "wet" side for most low OCR materials under the high initial horizontal loadings.

Significant volumetric change was found in the case of large initial stress anisotropy (Figure 3-15). Unlike the elastic compression, shearing at the "dry side" generates negative pressure and soils will deform nonlinearly when it yields. The subsequent dissipation of negative pore pressure further shears the cavity wall which keeps it dilating until a maximum convergence is reached. Utilizing a nonlinear relationship between permeability and void ratio, Figure 3-16 gives the ultimate permeability change in the weakening zones. A maximum of threefold increase of permeability is found corresponding to the 20% increase of void volumes. Thus the permeability would not significantly change in a long-term consolidation of surrounding medium. This was also confirmed by the similar results from the permeability tests carried out in the supported and unsupported cavities in heavily overconsolidated materials (Ratnam et al., 2005).

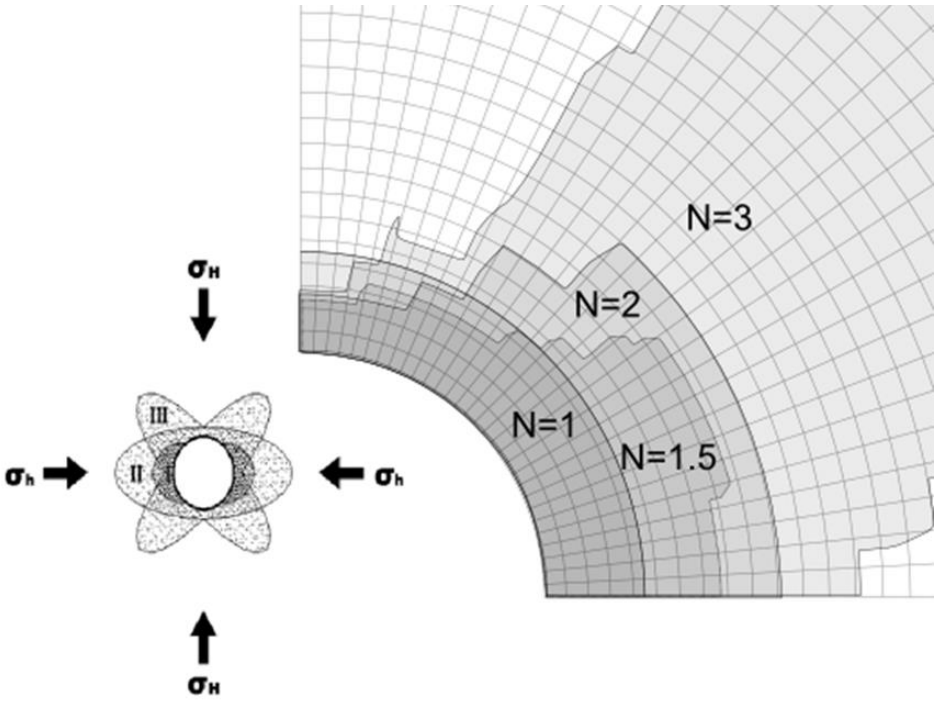

Figure 3-14. Drilling induced deformation of borehole and three types of shearing modes for the circular opening under non-uniform stresses. Plastic deformed borehole shape under N=1.5 and N=2 correspond to the mode II and N=3 is equivalent to the mode III. The missing example for mode I might be achieved by having relatively large OCR for the high anisotropic stress conditions.

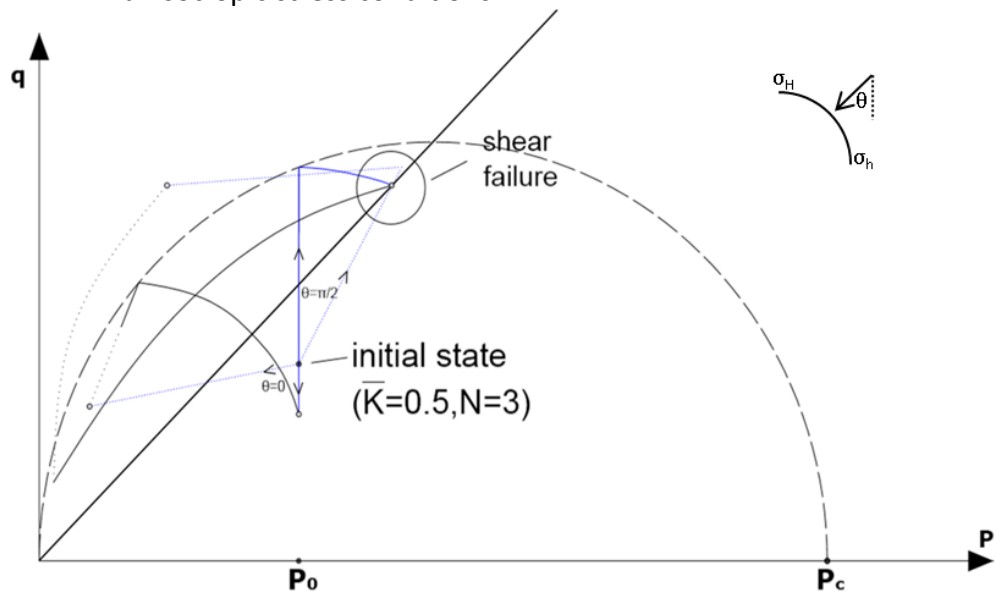

Figure 3-15.The stress paths of yielded borehole in the q-p space (dotted line shows total stress path and solid line shows effective stress path) under anisotropic loadings.

However, volumetric change may not be primarily responsible for the permeability change once the material yields (Schutjens and Hanssen, 2004). In highly cemented sediments, the clay content is the most important factor that controls the internal conductivity in the pore network (Cade et al., 1994), so rather than the void ratio, permeability may be more sensitive to the microstructures that formed during diagenesis. At the instance of shearing the material could not sustain the high deviatoric stress at relatively low mean stress and a catastrophic failure takes place until the residual state or critical state is reached. This is always accompanied with the rearrangement of microstructure and damage of the cementation mentioned above, which may also lead to a considerable increase of the permeability. More severely, the failure zone (e.g., as shown in Figure 3-16) in soft medium is at risk of collapsing and being washed out eventually.

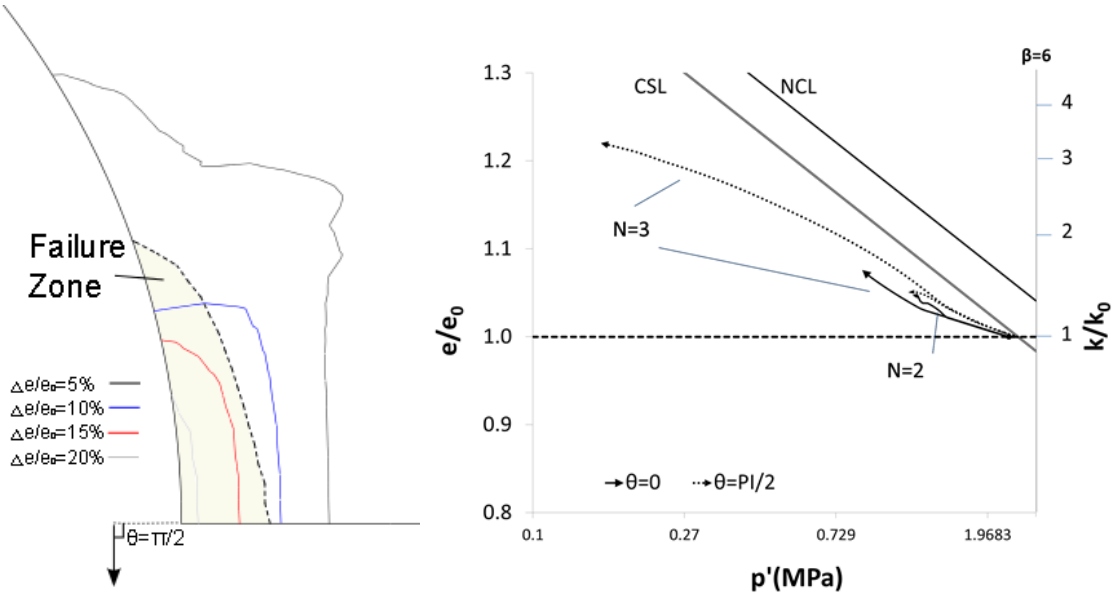

Figure 3-16. The volumetric changes and permeability changes after relaxation in the vicinity of the cavity (left); the expansion paths at two azimuths of cavity wall (right).

Figure 3-17 and Figure 3-18 show the convergence of borehole wall at two azimuths as a result of dissipation of excess negative pore pressure.

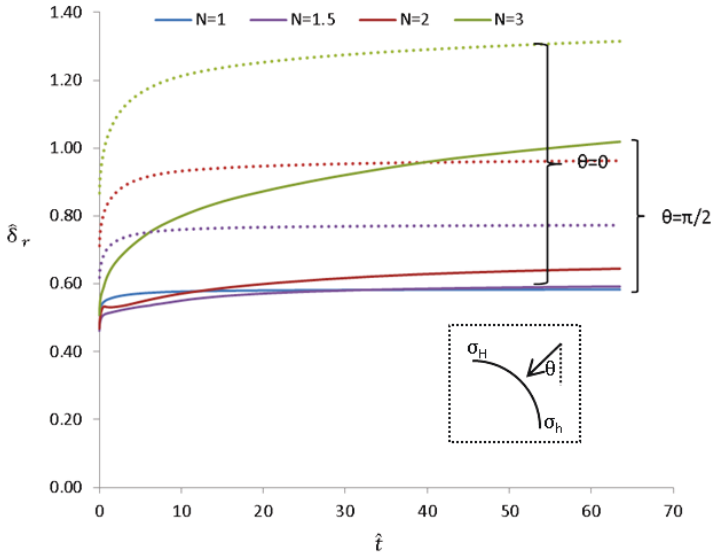

Figure 3-17. The variation of radial displacement during the consolidation for the yielding materials at azimuths of σ_H and σ_h

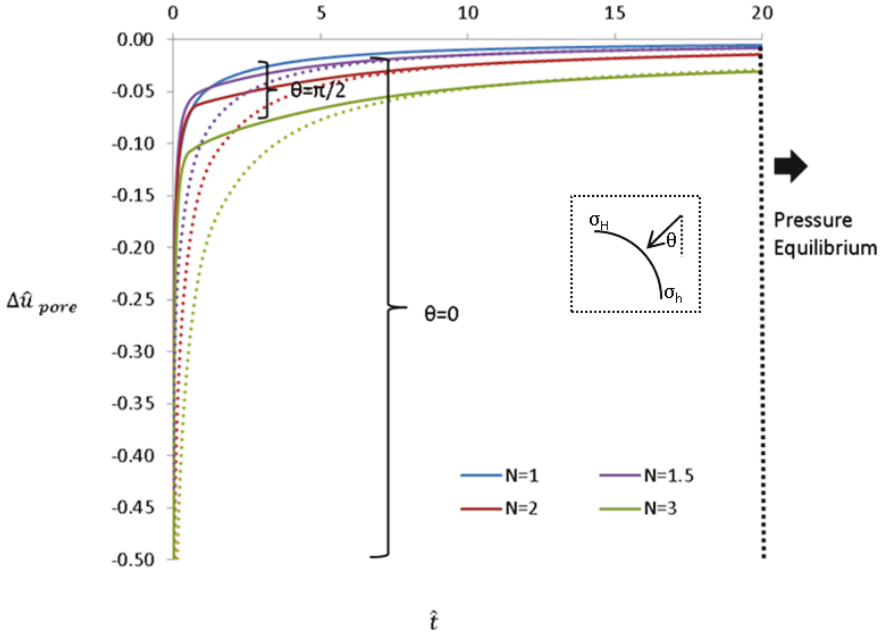

Figure 3-18. The variation of pore pressure during the consolidation for the yielding materials at azimuths of σ_H and σ_h.

3.3 Borehole Consolidation and Its Implications

3.3.1 In-situ Stress Orientations

Leeman (1971) has successfully determined the orientaions of princial stresses by applying the strain gauge rosettes on the flattened end of a borehole to measure the in-plane stresses. The same principle has been employed by Martin (1996) who measured the convergence of a shaft excavated in granite and then interpreted the insitu stresses. To find the direction of principal strains, at least three pairs of gauges in the symetrical alignment are required. The measurement could be also achieved by streching the calipers radially with their end pads evenly spaced on the wall (Figure 3-19).

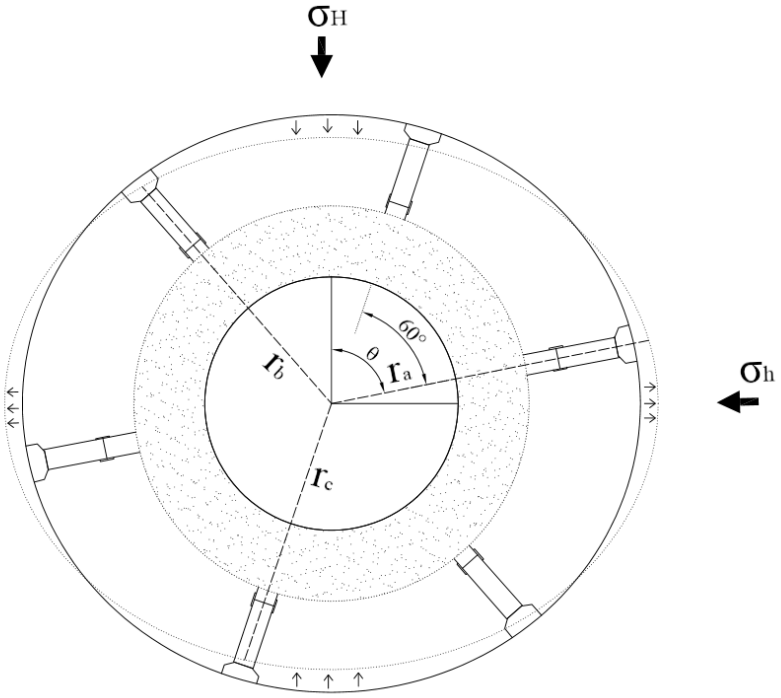

Figure 3-19. The caliper measurement of the deforming borehole

Increasing the number of arm pairs includes more points to be measured on the periphery and minimize the error from the inaccurate measurement affected by the possible surface roughness or the notches of borehole. Mohr's cricle could be constructed to determine the displacements at the orientations of two

principal stresses. In this paper, the displacement interpretation based on such a set is exemplifed by a model with three pairs of arms, 60° apart adjacently. The radii of borehole can be measured at three abitrary orientations, a,b and c. The displacements from time *t* to *t+1* are given accordingly,

$$\begin{aligned} \delta_a &= r_a^{t+1} - r_a^t \\ \delta_b &= r_b^{t+1} - r_b^t \\ \delta_c &= r_c^{t+1} - r_c^t \end{aligned} \tag{3.15}$$

For the circular opening, the radial displacement at an arbitrary position *a,* which is ϑ clockwise to the orientation of σ_H (Figure 3-19) could be expressed in the form of

$$\delta_a = \frac{\delta_H + \delta_h}{2} - \frac{\delta_H - \delta_h}{2}\cos(2\theta) \tag{3.16}$$

where δ_H and δ_h are radial displacement aligned with σ_H and σ_h respectively. The Eqn(3.16) is illustrated as Mohr's circle in Figure 3-20.

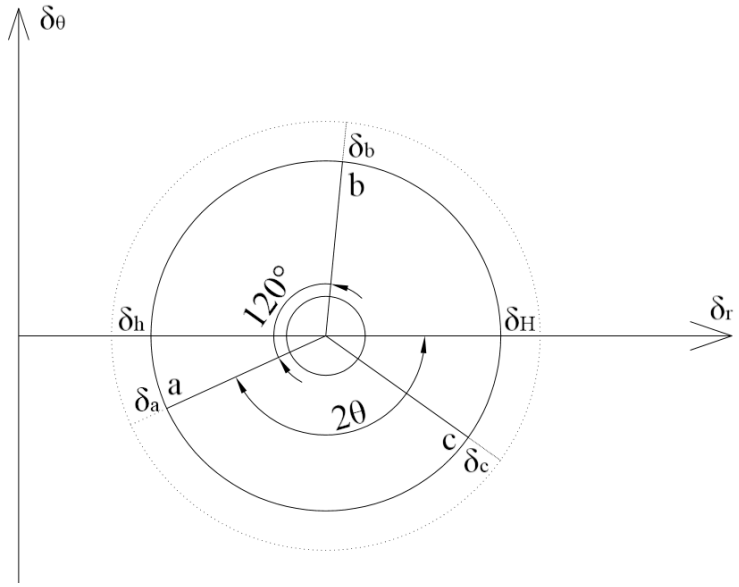

Figure 3-20. Mohr's circle in the displacement domain

Knowing the three radial displacements δ_a, δ_b, and δ_c, one can find δ_H and δ_h, and their angles to the orientation of calipers by

$$\begin{aligned}
\delta_H &= \frac{1}{3}\left(\delta_a+\delta_b+\delta_c+\sqrt{2\left[(\delta_a-\delta_b)^2+(\delta_a-\delta_c)^2+(\delta_c-\delta_b)^2\right]}\right)\\
\delta_h &= \frac{1}{3}\left(\delta_a+\delta_b+\delta_c-\sqrt{2\left[(\delta_a-\delta_b)^2+(\delta_a-\delta_c)^2+(\delta_c-\delta_b)^2\right]}\right)\\
\cos(2\theta) &= (2\delta_a+\delta_b+\delta_c)\Big/\sqrt{2\left[(\delta_a-\delta_b)^2+(\delta_a-\delta_c)^2+(\delta_c-\delta_b)^2\right]}
\end{aligned} \tag{3.17}$$

3.3.2 Convergence Rate

It is always difficult to estimate how much the borehole has already consolidated ahead the time of instrumentation. The calculation of initial displacement based on the outside diameter of drill collar may not be accurate, because drilling heavily disturbs the initial shape of borehole. One way to avoid this is to find the convergence rate by calculating the change of displacement over a certain period of time. The difference between the maximum displacement δ_H and minimum displacement δ_h are used as indices to minimize the error (Figure 3-21). The coefficient *D* could be found from Eqn(3.14): $D=\frac{r_0\gamma_w}{2k\overline{K}\sigma'_V}\frac{(1-2\nu)}{(1-\nu)}$.

Figure 3-21 also reveals that as $\hat{t}$ increases, the displacement rate would reduce in a hyperbolic fashion and ultimately decay to zero. Thus, to ensure a good resolution of the rate difference, a fast implementation of the instrument is preferred especially for highly permeable formations. One should be careful in evaluating the time when the measurement starts relative to the time when the borehole is drilled. An incorrect estimation of $\hat{t}_0$ will shift the data horizontally and makes it match to the wrong characteristic curve. If the pore pressure measurement is accessible in the same period of time, Figure 3-12 could be used to rectify and optimize the inversion. However, this will not be discussed in this paper.

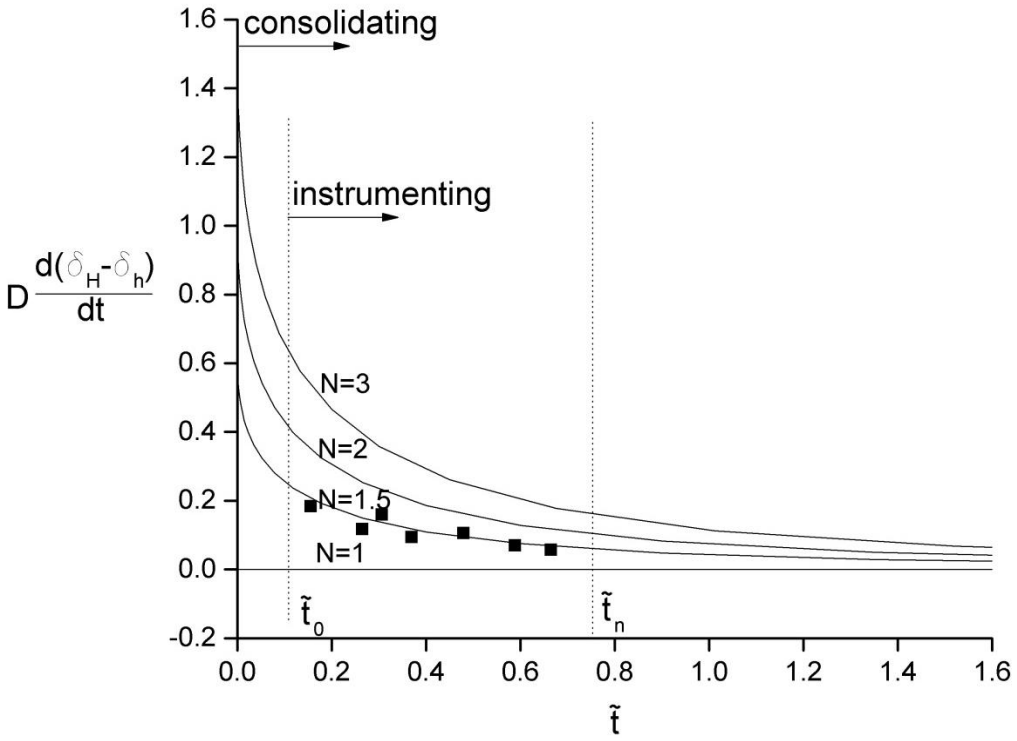

Figure 3-21. The convergence rate of borehole during the elastic consolidation. The scattered data points mimics the ones obtained from the field test.

Analysis above investigates the feasibility of applying caliper tools to intepret the horizontal stress anisotropy in the unyielded boreholes. As discussed above, if the inner boundary continues squeezing in at all the positions of annulus, it indicates that borehole is under trenmendous shearing. In this case, not only at the orientation of σ_H, the cavity may also deform plastically at the orientation of σ_h.

In this case, only the displacement measurement in the direction of σ_H is reliable, as the shear failure at the other side may have failures with both compression and dilation. The convergence rates are plotted with δ_H doubled to be compared with the ones under purely elastic consolidation (Figure 3-22). A major difference is found for the case of low stress anisotropy where the borehole consolidates much faster than the elastic case. Whereas, the curve for high stress anisotropy (e.g., N=3) is similar to that of unyielded elements at the early consolidation

stage. Thus, care should be taken if borehole yields after drilling; inversion based on the assumption of purely elastic consolidation may overestimate the initial horizontal stress anisotropy *N*.

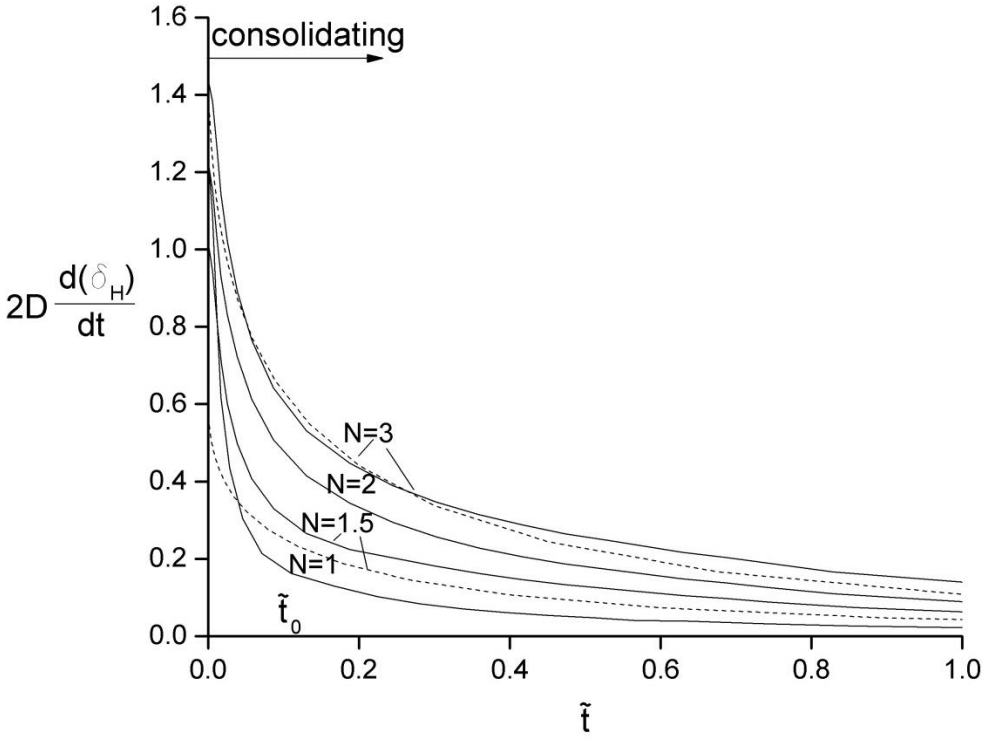

Figure 3-22. The convergence rate of borehole during the elasto-plastic consolidation. The dashed curves are under the elastic consolidation.

4 Cavity Expansion in the Pre-bored Opening under Non-Uniform Loadings

The linear elastic/perfectly plastic model has been firstly introduced to the interpretation of pressuremeter testing by Gibson & Anderson (1961). The approach assumes that the in-plane far field stress is isotropic and materials yield as the undrained shear strength is reached when

$$P_i = P_0 + S_u \tag{4.1}$$

It can be seen in Figure 4-1 that if the borehole has passively sheared during drilling, shearing is the only possible failure mechanism as the cavity expands in the cohesive materials; an analytical solution for such cases is given by Wang & Dusseault (1994) who considered the strength reduction and volume changes after failure. Whereas, if the stress limit has not been reached in the stage of passive loading, tension failure is likely to take place during active loading prior to shearing.

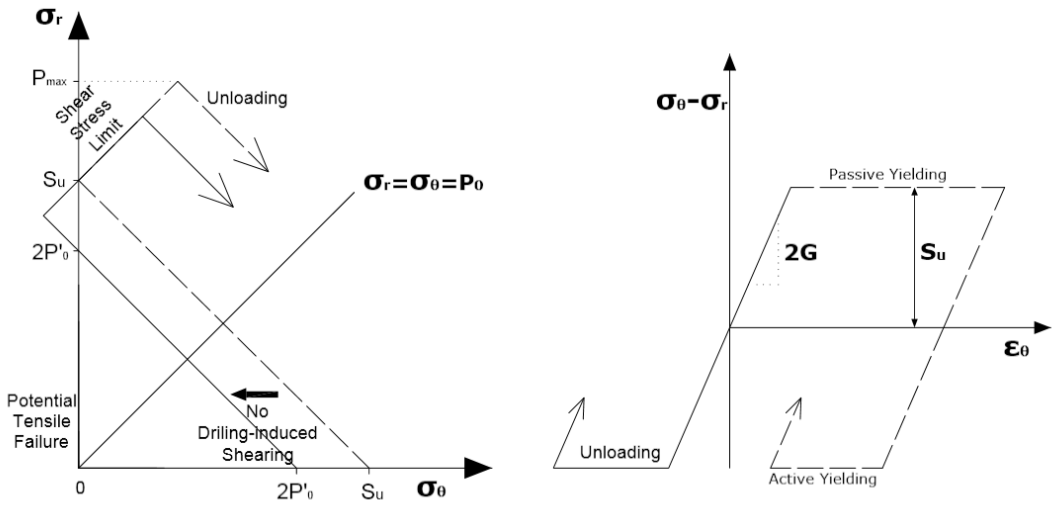

Figure 4-1. The undrained response of cavity stresses of linear elastic/perfectly plastic materials under isotropic horizontal loading. The dashed line presents the behavior of materials which have been sheared by passive loading.

4.1 Undrained Expansion

If the borehole is under non-uniform boundary loadings, the total mean stresses are different along the cavity periphery and is no longer equal to the initial mean stress. However, for undrained elastic expansion, the mean effective stress will still remain constant, according to

$$\Delta\varepsilon_v = \frac{(1-2\nu)}{3E}\Delta P' = 0 \tag{4.2}$$

and as inferred by the plane strain condition,

$$\Delta\sigma'_z = \nu(\Delta\sigma'_r + \Delta\sigma'_\theta) = 0 \tag{4.3}$$

Thus, like the expansion under hydrostatic pressure, the effective tangential stress and radial stress also changes equally but inversely when under anisotropic loadings. The stress paths for an unyielded element at the two azimuths of inner boundary are illustrated in Figure 4-2. The generated excess pore pressure could be calculated based on the increment of the total mean stress.

The order of the principal stresses has been reversed as the loading regimes changes from active state to passive state. σ'_ϑ will reduce to zero before the passive yielding occurs. Generally, argillaceous sediments have some tensile strength, *T*, based on their degree of cementation, so tensile failure may not necessarily be triggered before material yields (Figure 4-2, left).

If *T* is known, the initiation of tension cracks could be predicted by

$$\begin{aligned} \sigma'_r(H) &> 3\sigma'_h - \sigma'_H + T \qquad \theta = 0 \\ \sigma'_r(h) &> 3\sigma'_H - \sigma'_h + T \qquad \theta = \pi/2 \end{aligned} \tag{4.4}$$

Tension hazards are posed at the entire wellbore annulus, and the tendency for tensile failure depends not only on the magnitude of effective radial stress but also on the threshold of shearing at a specific azimuth. From the last chapter, it was shown that the borehole might be severely damaged at the orientation of σ_h

under high anisotropic stresses. The prediction of the stress states as well as the resultant deformation becomes extremely difficult. Poorly consolidated materials may have a hardening potential within the zones at the right side of yield ellipse (Figure 4-2, right ($\mathbf{a_h}$)) and the circumferential stress keeps decreasing even after yielding, so the tensile failure is likely to happen near the azimuth of σ_h (Figure 4-2, left). Considering those uncertainties mentioned above, only the expansion in an elastically deformed borehole (in the initial condition of $\sigma'_{\vartheta,h}= 3\sigma'_h-\sigma'_H$ and $\sigma'_{\vartheta,H}= 3\sigma'_H-\sigma'_h$) will be included in the following discussion.

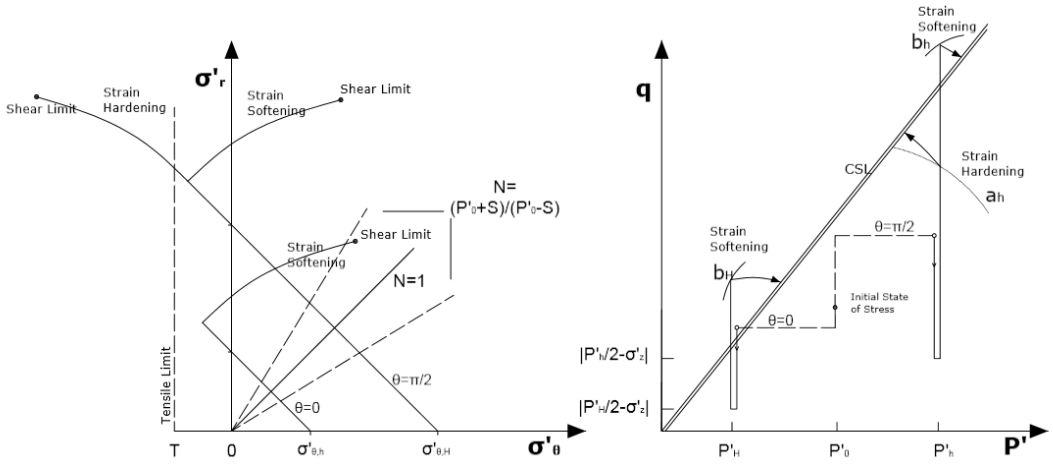

Figure 4-2. Effective stress paths for the undrained cavity expansion on the boreholes which have been elastically unloaded. The Poisson's ratio is assumed zero.

At the azimuths of $\sigma_{H,}$ yielding is also likely to occur but at a moderate degree. Also, the stress trajectory tends to move towards the dry side of yield surface as drilling-induced pore pressure dissipates. This indicates that an undrained expansion will only lead to the strain softening after material yields. Passive shear failure may take place before σ'_ϑ reduces to zero.

4.1.1 Mobilized Shear Modulus

It is commonly assumed that the modulus of the materials is a constant for most borehole stability or cavity expansion problems (Detournay and Cheng, 1988;

Randolph et al., 1979; Zhou et al., 2014). However, the stress redistribution under non-uniform loadings will significantly rearrange the solid particles and thus change material stiffness. By assuming constant volume compressibility κ, the shear modulus can be calculated as a function of void ratio e and mean effective stress p' and updated at each step of iteration during the numerical computation, according to Eqn(1.12). However, it is important to realize that this function is limited to the lightly or moderately consolidated samples (Zytynski and Randolph, 1978); a high value of overconsolidation ratio may lead to the overestimation of elastic strain and underestimation of shear modulus.

The stress redistribution after the borehole drilling and relaxation induces the variation of shear moduli in the vicinity of cavity. Figure 4-3 shows the profile of shear moduli as a result of drilling in different type of soils (stiff sandstone, dense sand and soft clay, respectively). In all the cases, the shear moduli at the top of the annulus (direction of the maximum horizontal stress, ϑ=0) are significantly reduced while those at the side (direction of the minimum horizontal stress, ϑ=90°) are increased. The effect of the mobilized modulus has been illustrated by comparing the expansion curves computed under the assumptions of constant G (Figure 4-4).

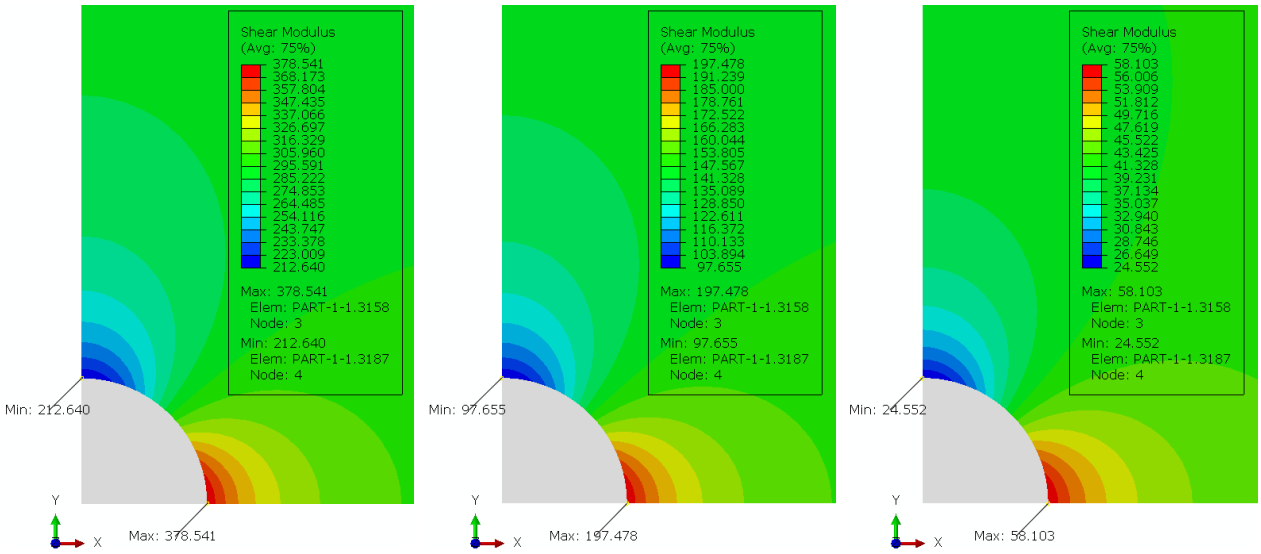

(a) v=0 (G_0=293MPa) (b) v=0.2 (G_0=147MPa) (c) v=0.4 (G_0=42MPa)

Figure 4-3. The contour of shear modulus for the deformed boreholes under stress anisotropy of N=1.5

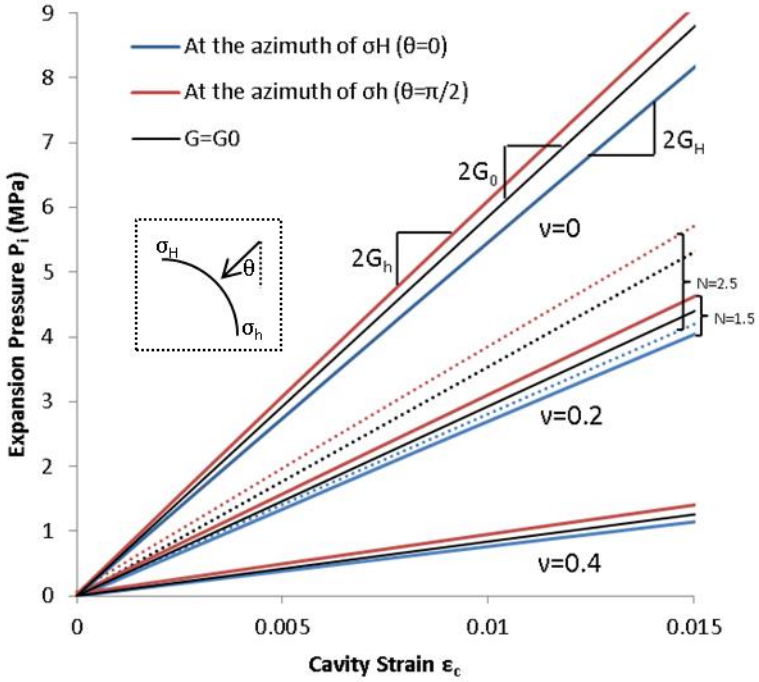

Figure 4-4. The Expansion curves in the elastic region for the varying Poisson's ratios. 1) ν=0, G_h=302MPa *and* G_H=272MPa; 2) ν=0.2, G_h=153MPa and G_H=140MPa 3) ν=0.2, G_h=45MPa and G_H=37MPa

Indeed, whether the shear modulus is assumed constant or varying as a function, it remains unchanged during the undrained expansion. It is worth noting that the G_h and G_H obtained from expansion curves are not equal to the values right at the cavity surface as shown in Figure 4-3. The interpreted shear modulus for a certain orientation appears to be the average value over some distance in its radius. It does not deviate significantly from the virgin shear modulus G_0 (Figure 4-4). Under such a circumstance, by averaging the moduli from the expansion measurements on separate strain arms we can still have a good estimate of G_0.

A series of SBPT (self-bored pressuremeter testing) have been carried out in the horizontal boreholes into the tunnel liner at underground research lab in the Mol, Belgium (Liu et al., n.d.). The pressuremeter was inflated against the non-hydrostatic boundary stresses in the deep Boom Clay formations. As a result, the

non-uniform expansion curves measured by independent strain sensors at different axes were presented in Figure 4-5. The shear modulus represented by the initial linear section of each curve demonstrates its anisotropy around the cavity – the closer to the orientation of the maximum initial stress, the lower stiffness the soil would be.

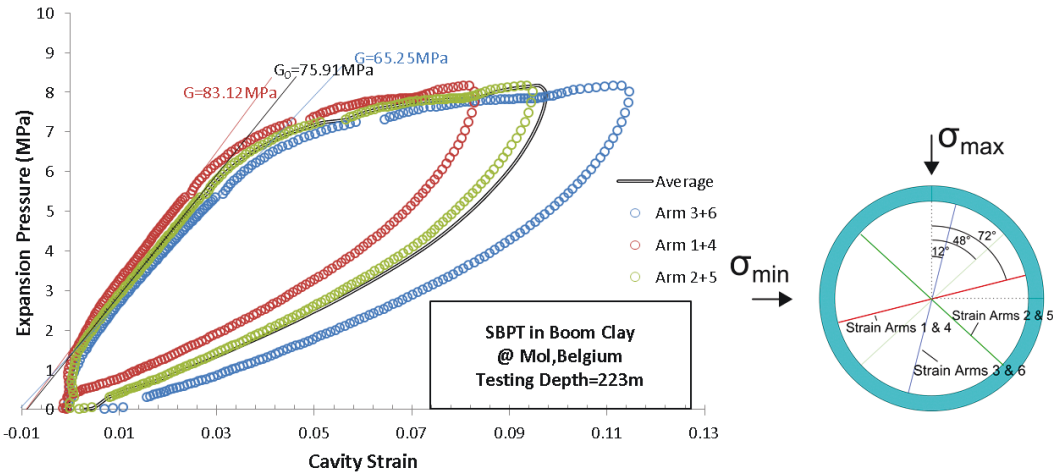

Figure 4-5. Shear moduli measured at different axes of strain arms in the expansion plane of SBPT in Boom Clay. σ_{max}=4.02MPa ; σ_{min}=3.13MPa.

4.1.2 Elastic Expansion

Figure 4-6 shows the undrained response of the cavity wall to expansion. The dimensionless form of expansion pressure is defined in the same way as for Δu_{pore} in Chapter 3:

$$\hat{p}_i = \frac{p_i}{\bar{K}\sigma'_V} = \frac{2p_i}{\sigma'_H + \sigma'_h} \tag{4.5}$$

The initial ambient pore pressure is not involved in the calculation of total stress hereinafter, because its effect on the soil deformation is offset by the in-balanced mud pressure which has been discussed in the last chapter. However, the loading in the zones of mobilized shear modului would generate a considerable amount of excess pore pressure at the cavity boundary (Figure 4-6). This is distinctly different from the calculation under the assumption of constant

shear modulus where pore pressure hasn't changed after expansion. Interestingly, elastic cavity expansion in the distressed borehole leads to the pore pressure change opposite to what was derived for quick insertion problems, such as pile driving and self-bored pressuremeter testing, where no stress-relief and thus no mobilization of shear modulus happens initially (Zhou et al., 2014). Excess pore pressure is generated at the azimuths of ϑ=0 while a less amount of negative excess pore pressure is at ϑ=π/2. Also, the total radial stress changes more rapidly at ϑ=0. Thus, the surface tension fractures, if any, would be initiated first at the azimuth parallel to the maximum horizontal stress.

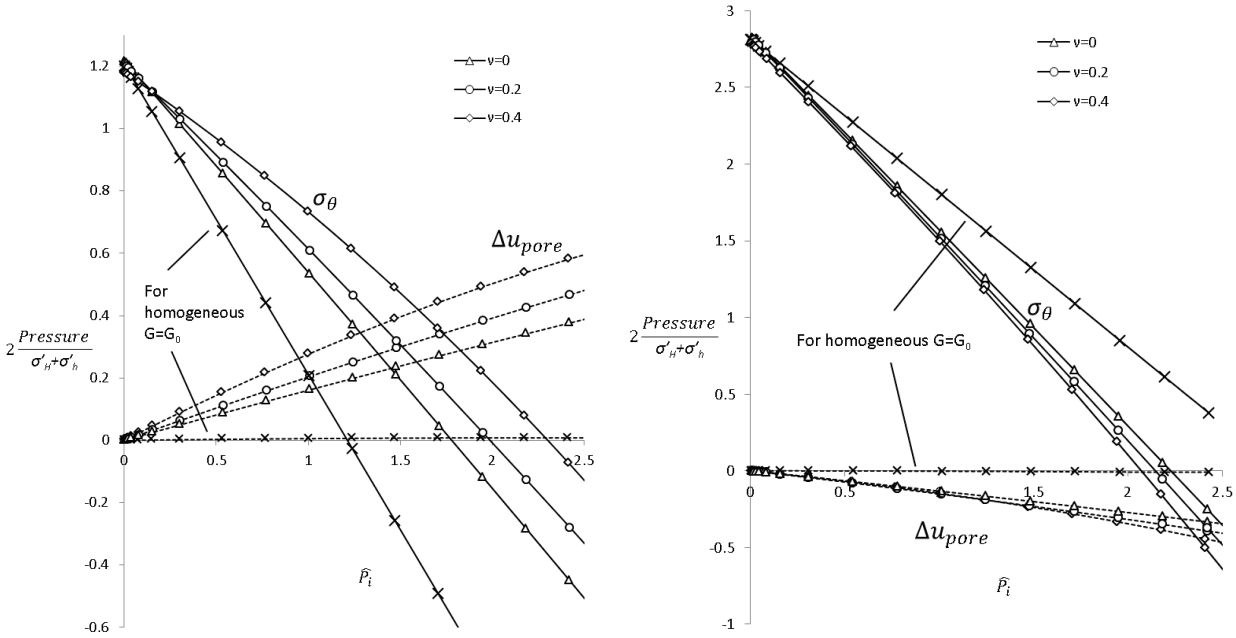

(a)θ=0 (b)θ=π/2

Figure 4-6. The variation of total stresses and excess pore pressure at two azimuths on the cavity wall as the expansion pressure increases.

The pressure variations are plotted against the radial distance normalized by the wall displacement r_a at azimuths of σ_H (ϑ=0) (Figure 4-7) and σ_h (ϑ= π/2) (Figure 4-8). The stress profile is independent of the magnitude of shear modulus if it is homogenous all over the medium, while the response could be different if the

heterogeneity is present. For materials with higher Poisson's ratio *v* (or higher gradient of shear modulus *G*), a more marginal change of total radial stress as well as pore pressure is observed. This is dominant in the near-cavity zones ($r/r_0<2$), while pore pressure changes slightly and inversely in the formation further from the borehole. It is also interesting to notice that, in the medium where large stress anisotropy is present, an internal shearing is likely to take place near the axis of σ_H (Figure 4-7). The comparison of effective stress profiles at two horizontal stresses also indicates both tensile and shear failure would be more likely happen in the radius of maximum in-situ stress.

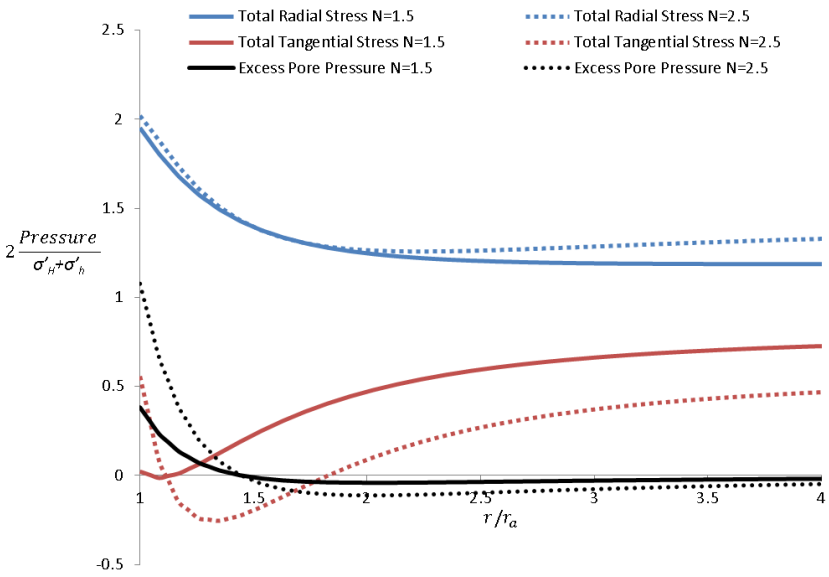

Figure 4-7. The variation of total stress and excess pore pressure with the normalized radius in the direction of σ_H for the initial stress anisotropies of *N=1.5* and *N=2.5* when expansion pressure $P_i=\sigma'_h+\sigma'_H$.

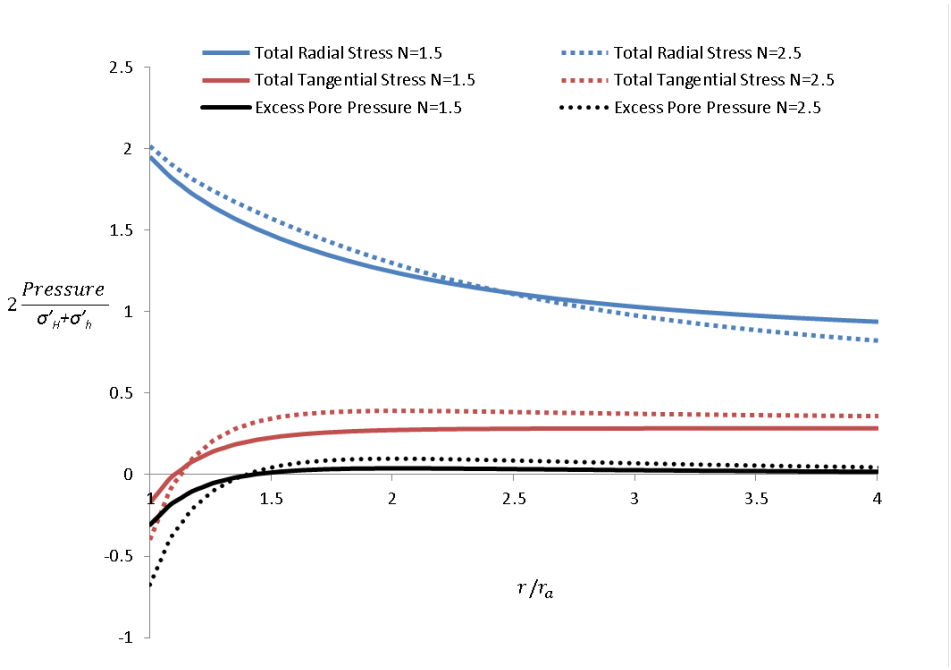

Figure 4-8. The variation of normalized total stress and excess pore pressure with the normalized radius in the direction of σ_h for the initial stress anisotropy of *N=1.5* and *N=2.5* when expansion pressure $P_i=\sigma'_h+\sigma'_H$.

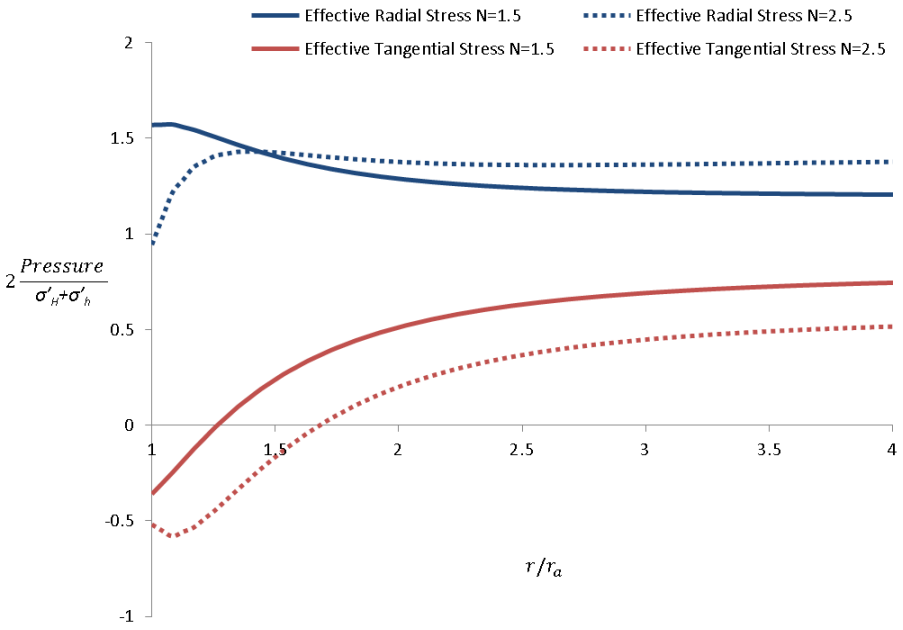

Figure 4-9. The variation of effective stress and excess pore pressure with the normalized radius in the direction of σ_H for the initial stress anisotropy of *N=1.5* and *N=2.5* when expansion pressure $P_i=\sigma'_h+\sigma'_H$.

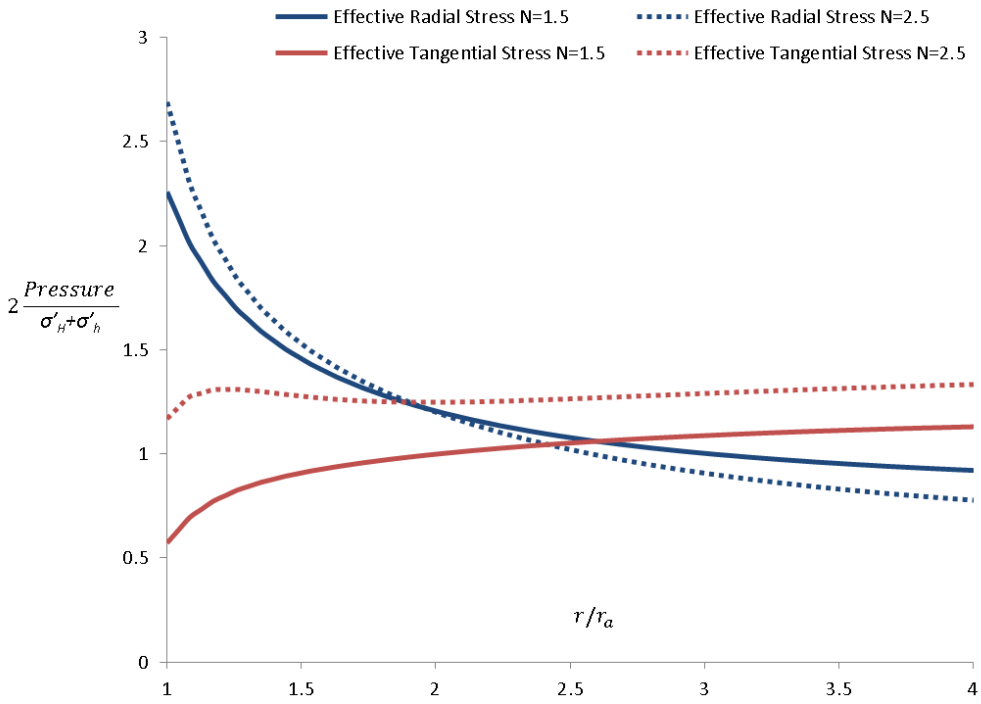

Figure 4-10. The variation of effective stress and excess pore pressure with the normalized radius in the direction of σ_h for the initial stress anisotropy of *N=1.5* and *N=2.5* when expansion pressure $P_i=\sigma'_h+\sigma'_H$.

4.1.3 Plastic Expansion

From the last chapter, it was shown that for the azimuth of σ_h, plastic expansion is extremely sensitive to the initial stress anisotropy as shearing may take place when the strength of soil is not able to sustain the high deviatoric stress. In this section, the plastic behavior of the formation under the uniform internal loading is evaluated.

Figure 4-11 is the close view of the near-borehole region in the expansion model. Two elements at the cavity boundary and another two elements 1.5 borehole radii away from the wall are investigated. Their stress paths are given in Figure 4-12 and Figure 4-13. Unlike the expansion under the isotropic boundary loading, the stress paths for elements in the same radius are not replicable. Most of the stress loci in the direction of maximum horizontal stress lie in the dry side of the

yield surface where strain softening is expected. By contrast, elements located on the radius normal to the maximum horizontal stress have different responses after yielding. Those close to the borehole surface exhibit the behavior of softening while further away their strengths harden.

Figure 4-14 and Figure 4-15 are the radial profiles of the effective stress and excess pore pressure. The shaded areas in both graphs refer to the critical states that the elements on the radius have reached. As the state of shearing for each element are not uniform, the stresses have a big variation for elements in the radius of σ_h (Figure 4-15) – the entire principal stresses rise up in the hardening zone while they drop down in the softening zone. The excess pore pressure in the critical state zones, whether the materials being softened or hardened, is positive, which is similar to the pore pressure response of cavity expansion under hydrostatic boundary loadings (Randolph et al., 1979).

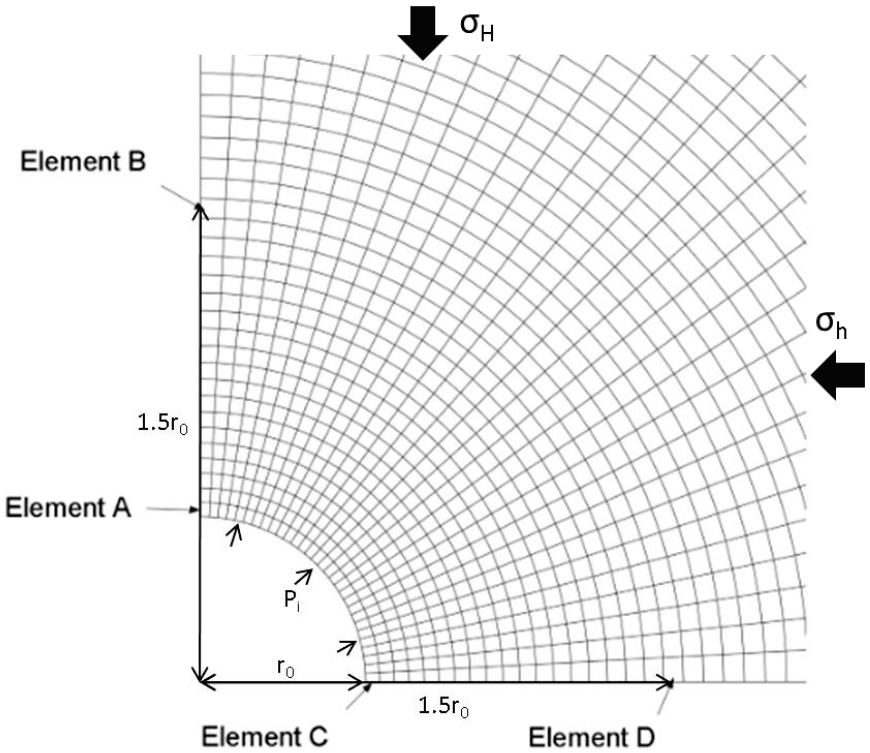

Figure 4-11. The cavity expansion model with the illustration of the elements being investigated (N=1.5)

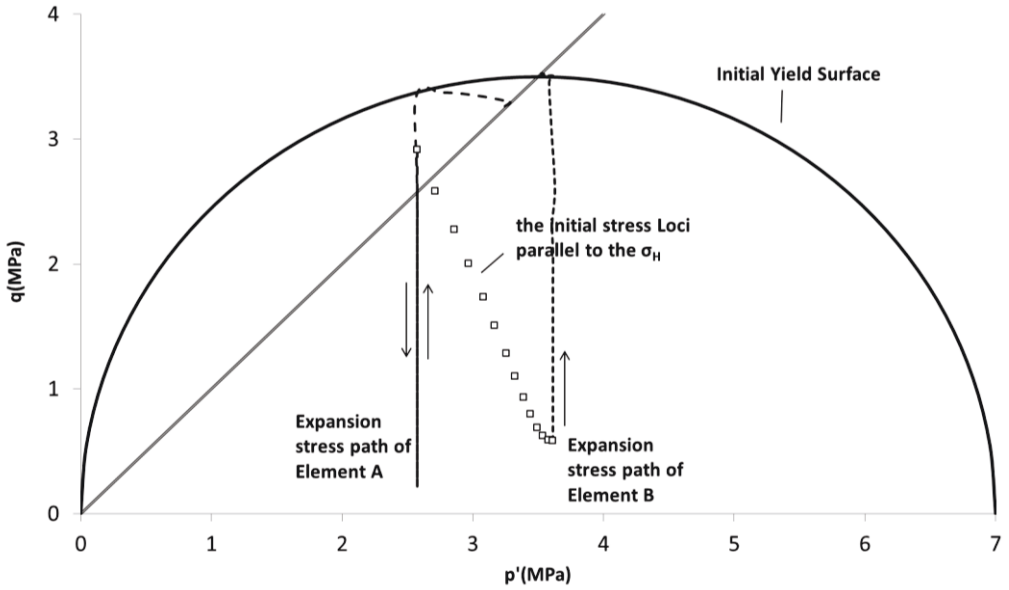

Figure 4-12. The effective stress paths of two elements aligned radially in the direction of $\sigma_{H.}$

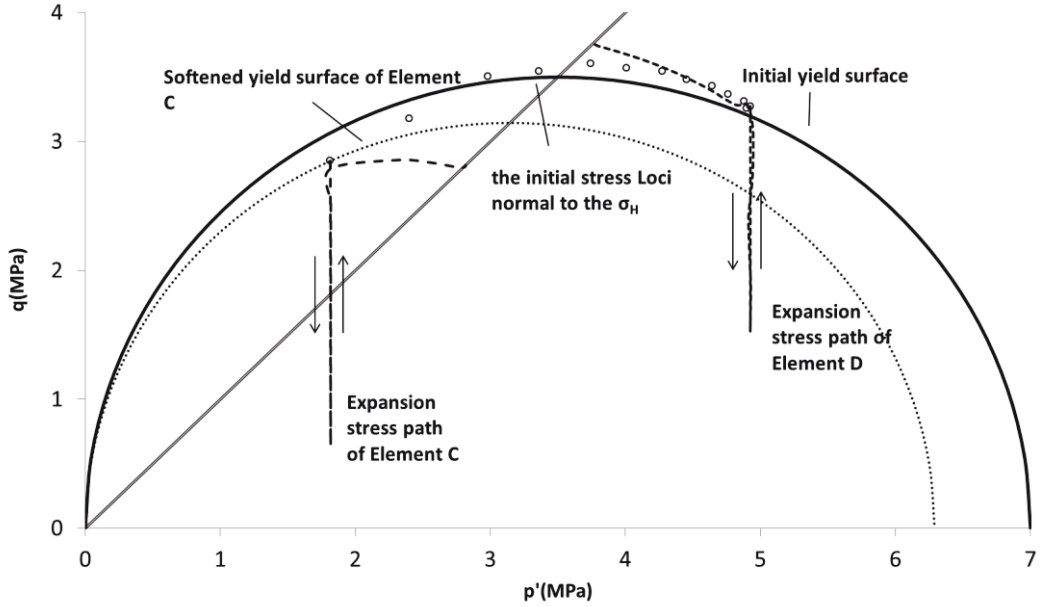

Figure 4-13. The effective stress paths of two elements aligned radially in the direction of σ_h.

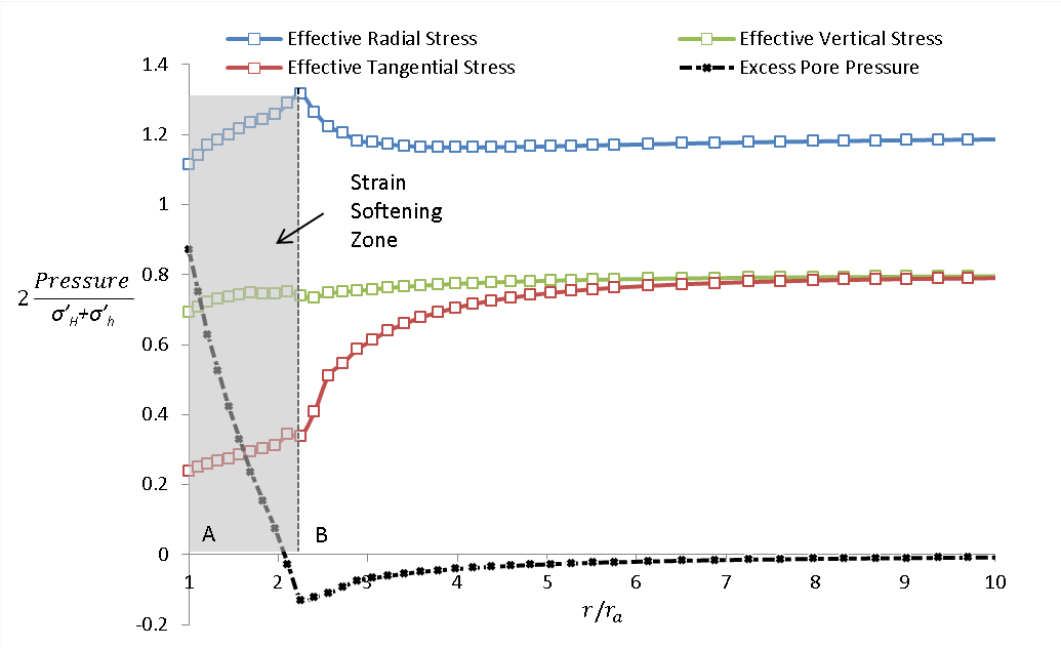

Figure 4-14. The distribution of effective stresses and the pore pressure in the direction of $\sigma_{H.}$ (P_i=5S_u)

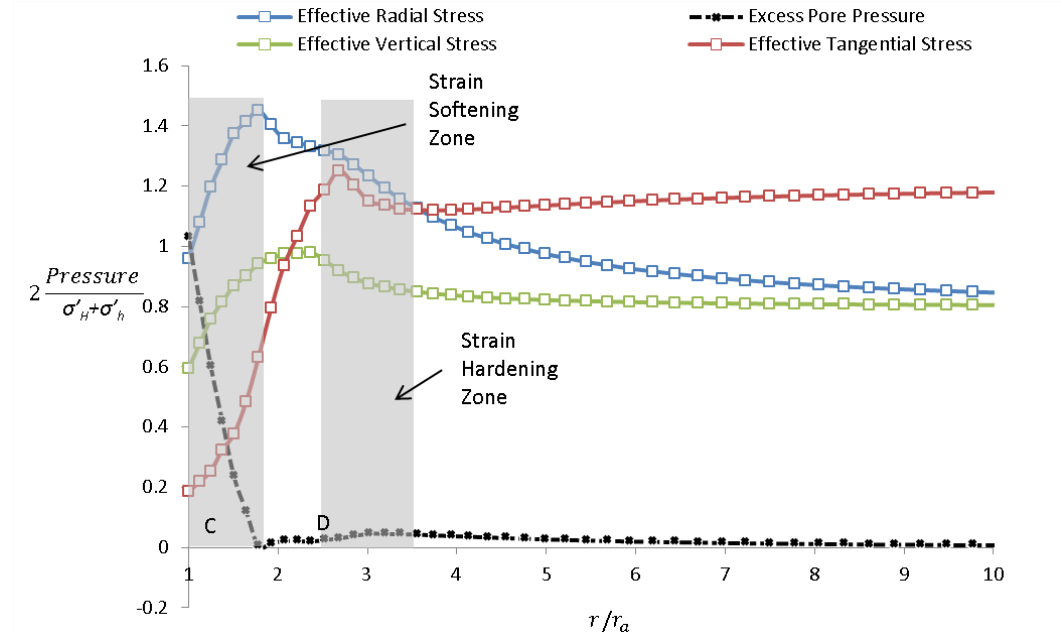

Figure 4-15. The distribution of effective stresses and the pore pressure along the grids in the direction of $\sigma_{h.}$ (P_i=5S_u)

4.1.4 Expansion Induced Damaged Zones

As shown in Chapter 3 and the previous findings from Detournay and St. John (1988), materials placed in the highly anisotropic stress field would undergo the

tremendous shearing in the zones between the radius of maximum and minimum in-plane stress. The cylindrical expansion on the pre-bored cavity also induces uneven increases of deviatoric stresses at the different locations on the borehole periphery. The resultant plastic zone in such a condition is unlikely in the circular shape as it was observed for the expansion under uniform loading.

In the following study, two groups of initial conditions (Table 4-1) are selected for the simulation of cavity expansion by the internal pressure increasing up to fourfold of undrained shear strength s_u[3] . In group A, the mean effective stress is assumed to be constant for each stress anisotropy *N*; in group B, the minimum effective horizontal stress is assumed to be equal to the effective vertical stress. All the samples to be evaluated are considered having the same consolidation history, i.e, *OCR* is constant.

In an isotropic stress field, the material response is identical in the annulus centered at the borehole axis. The potential damage zones also obey this circularity (Figure 4-16). The tangential stress is likely to become tensile stress in the increase of the expansion pressure, and the risk of tensile failure is highest near the place where the yielding is initiated.

Figure 4-17 shows the areas where the shearing and tension possibly occurs under non-uniform loadings. Zhou et al. (2014) has hypothesized the ellipse failure zones for the quick insertion problems. In the case of pre-bored cavity expansion, an ellipse region is developed for the class of low stress anisotropy (N<1.5), but as N goes higher the plastic zones may deform irregularly.

The expansion curve is plotted for all stress conditions in Group A (Figure 4-18). It should be noted that the shear moduli *G* is a constant parameter in Group A since the mean stress is equal according to Eqn(1.12). The borehole would fail

[3] s_u is determined by the initial condition: $s_u = \frac{1}{\sqrt{3}} M e^{(\Gamma - v_0)/\lambda}$

earlier at the direction of σ_H and the higher the insitu stress anisotropy is the sooner it fails. The expansion curve measured at the direction of σ_h, however, is much less sensitive to the insitu stress anisotropy *N*. The evaluation of the stress anisotropy based on the deformation in the direction of σ_H is favored.

Table 4-1. The parameters of selected initial conditions for the materials, Clearwater Clayshale

A	**$\gamma'_{average}$ (kN/m^3)**	**Z(m)**	**σ'_v (kPa)**	**σ'_H (kPa)**	**N**	**$\bar{\bar{K}}$**	**P'_0**	**OCR**	**n_p**	**e_0**
$\sigma'_h + \sigma'_H = 2\sigma'_v$	17	200	3400	3400	1	1	3400	5.88	5.88	53.1%
				2720	1.5	1	3400	5.88	5.25	53.1%
				6800	2	1	3400	5.88	4.41	53.1%
				5100	3	1	3400	5.88	3.36	53.1%
B	**$\gamma'_{average}$ (kN/m^3)**	**Z(m)**	**σ'_v (kPa)**	**σ'_H (kPa)**	**N**	**$\bar{\bar{K}}$**	**P'_0**	**OCR**	**n_p**	**e_0**
$\sigma'_v = \sigma'_h$	17	200	3400	3400	1	1	3400	5.88	5.88	53.1%
				5100	1.5	1.25	3966.7	5.88	4.26	52.6%
				6800	2	1.5	4533.3	5.88	2.82	52.2%
				10200	3	2	5666.7	5.88	1.45	51.5%

*The constants for the material are: ν=0.2; κ=0.03; λ=0.075; Γ=2.19 and M=1. The expansion Pressure $p_i=4s_u$

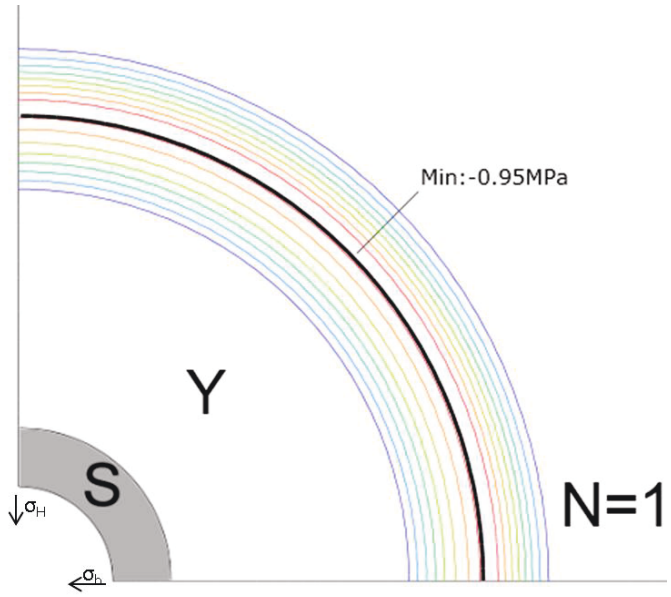

Figure 4-16. Possible failure zones induced by the expansion under isotropic initial stress. **S** represents the sheared zones or critical state zone; **Y** represents the yielding zone; the contours indicate the minimum tangential stress.

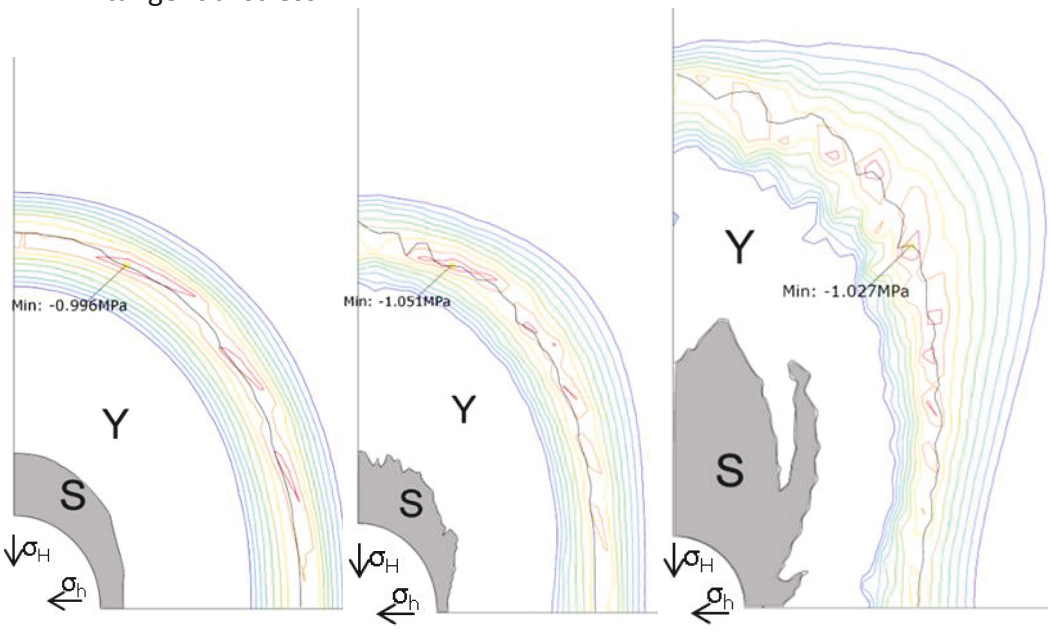

A **N=1.5** **N=2** **N=3**

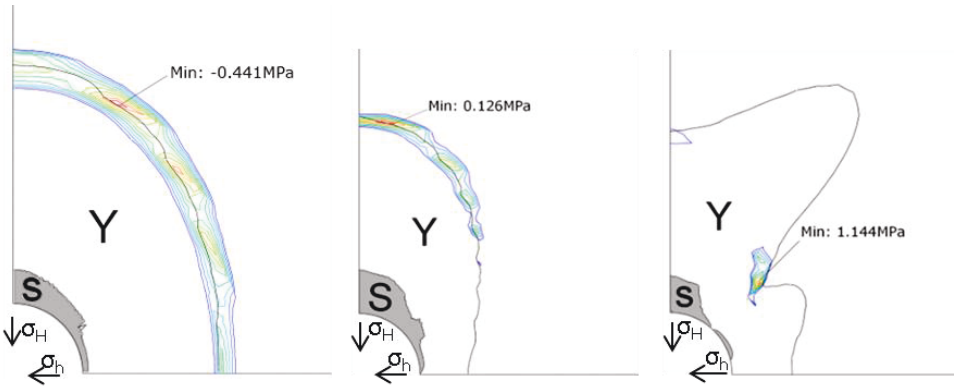

B **N=1.5** **N=2** **N=3**

Figure 4-17. Possible failure zones induced by the expansion under anisotropic initial stresses. **S** represents the sheared zones or critical state zone; **Y** represents the yielding zone; the contours indicate the minimum tangential stress.

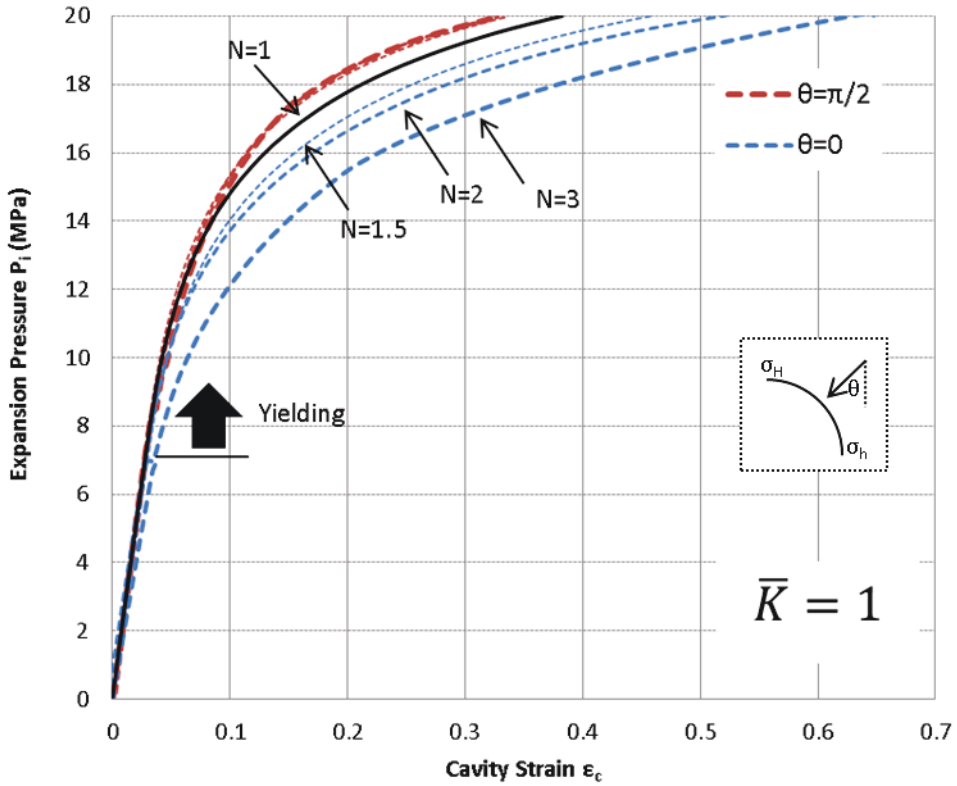

Figure 4-18. The expansion curves computed for different in-situ stress conditions in group A.

4.2 Partially Drained Expansion

As discussed in Chapter 2, the excess pore water can't be retained in the permeable medium at a normal rate of expansion. Partial drainage to the outside boundary may be present for most clayey materials.

4.2.1 Effect of Permeability

In this section, the response of pore medium in different permeable conditions is investigated. Since the permeability is not significantly changed by stress relief of borehole drilling, the permeability is assumed constant through the simulation. Figure 4-19 and Figure 4-20 are the excess pore pressure generated by the expansions in the permeable medium parallel and perpendicular to the maximum horizontal stress, respectively. The loading rate for this study is assumed 100kPa/s and one can find the corresponding drainage zones in Figure 2-8 to different medium permeabilities. The medium having the initial permeability of 10^{-11}mm/s is considered as "impermeable" zone, where no excess pore water would dissipate during cavity expansion. It is found that the drainage condition varies significantly from 10^{-9} mm/s to 10^{-6-} which is in accordance with the partially drained zones defined in Figure 2-8. Also, the fact that the drop of excess pore pressure is more distinguishable in the late stage of expansion than the beginning indicates that the drainage rate grows faster in the increase of expansion pressure. Thus, the excess pore pressure generation rate is maximum when the expansion starts, and this maximum rate is identical for each value of N regardless of the medium permeability.

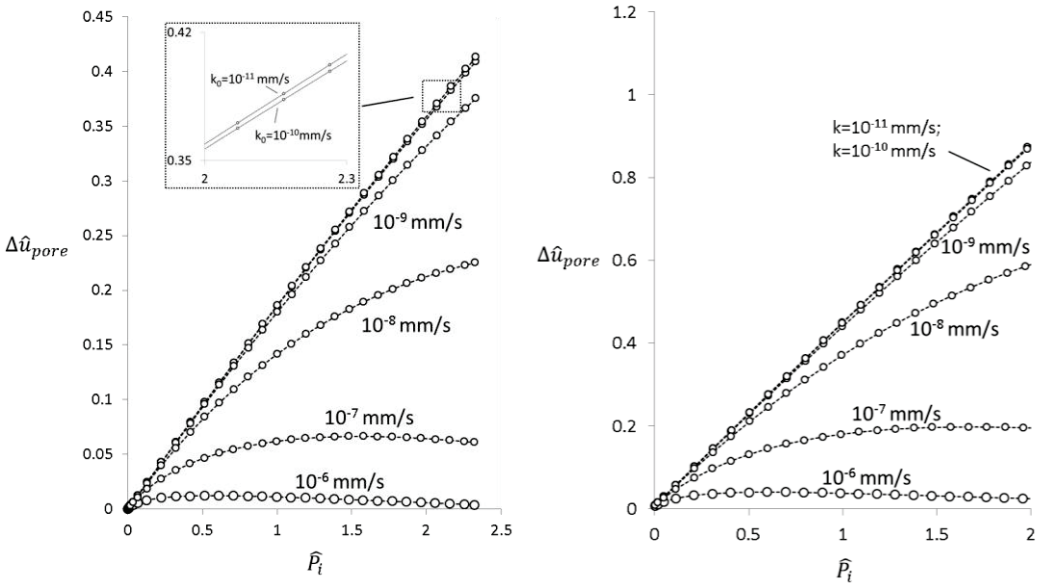

N=1.5 **N=2.5**

Figure 4-19. The excess pore pressure variation during the elastic expansion in the medium of different permeabilities (ϑ=0)

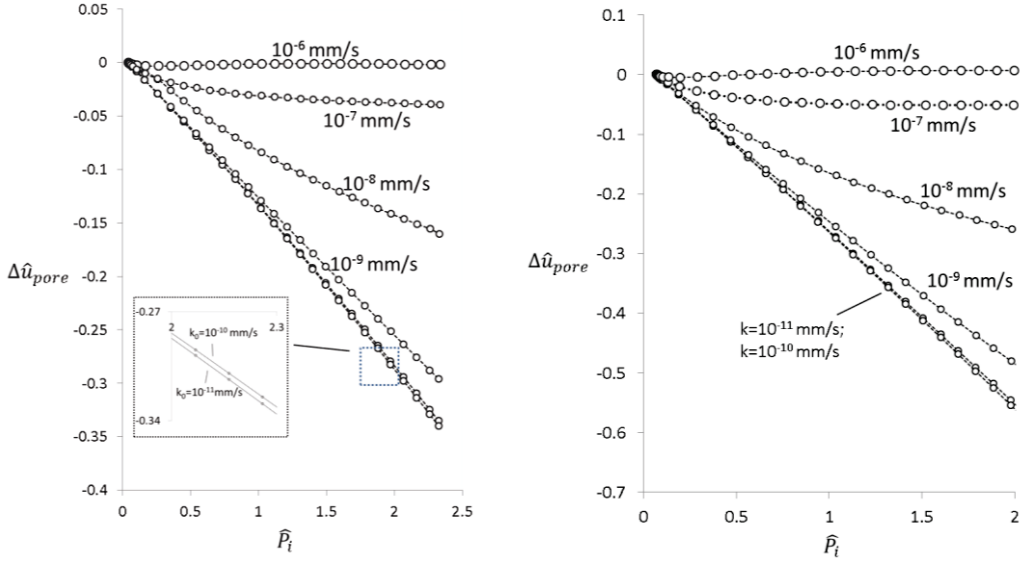

N=1.5 **N=2.5**

Figure 4-20. The excess pore pressure variation during the elastic expansion in the medium of different permeabilities (ϑ=π/2)

Figure 4-21 shows the relationship between the maximum excess pore pressure generation rate and stress anisotropy *N*. As we discussed above, another important factor affecting the excess pore pressure generation is Poisson's ratio *v*, which is responsible for the heterogeneous field of shear modulus. Herein, the plot is presented with the probabilistic calculation based on the reasonable range of Poisson's ratio from 0.1 to 0.3. Alternatively, if the Poisson's ratio is unknown, the value of *N* could still be estimated by the best fit curve of the data set.

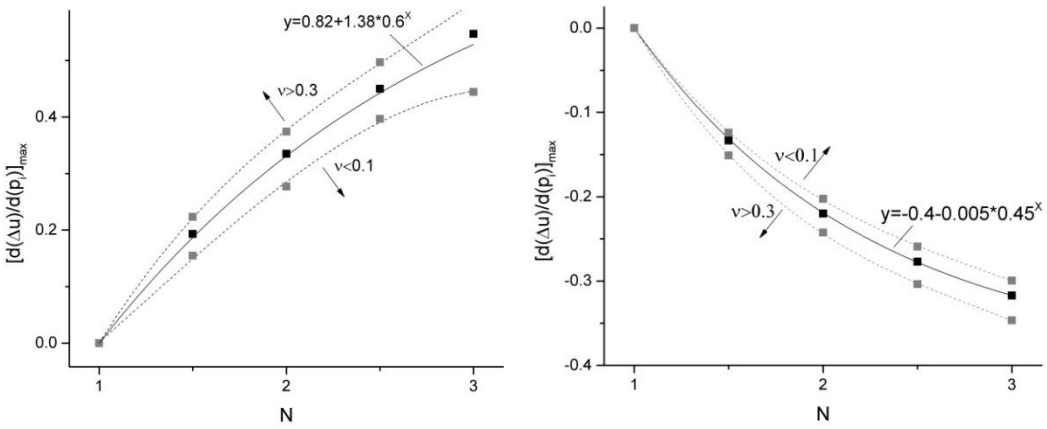

Figure 4-21. The maximum excess pore pressure generation rates at two azimuths in different anisotropic stress fields.

4.2.2 Maximum Expansion-Induced Excess Pore Pressure

The decreasing trend of excess pore pressure in the partially drained expansion infers that the peak must be reached when the expansion pressure increases to a certain level. The more permeable the medium is, the faster that the peak will be reached. The findings show that the permeability is negatively correlated to the value of p_i at the maximum excess pore pressure, and their relationship could be quantified by best fitting the data concatenated from each curve for stress anisotropy varying from 1 to 3 (Figure 4-22). In the low-permeability formation,

the drainage occurs slowly, and the excess pore pressure is unlikely to decline at a normal loading level. Therefore, an extrapolation should be performed on the limited data to obtain the critical value of $\hat{p}_i$(e.g., $\hat{p}_{i,1}$and $\hat{p}_{i,2}$ in the Figure 4-22). The estimation of permeability can therefore be narrowed down into the shaded area by mapping $\hat{p}_{i,1}$ and $\hat{p}_{i,2}$.

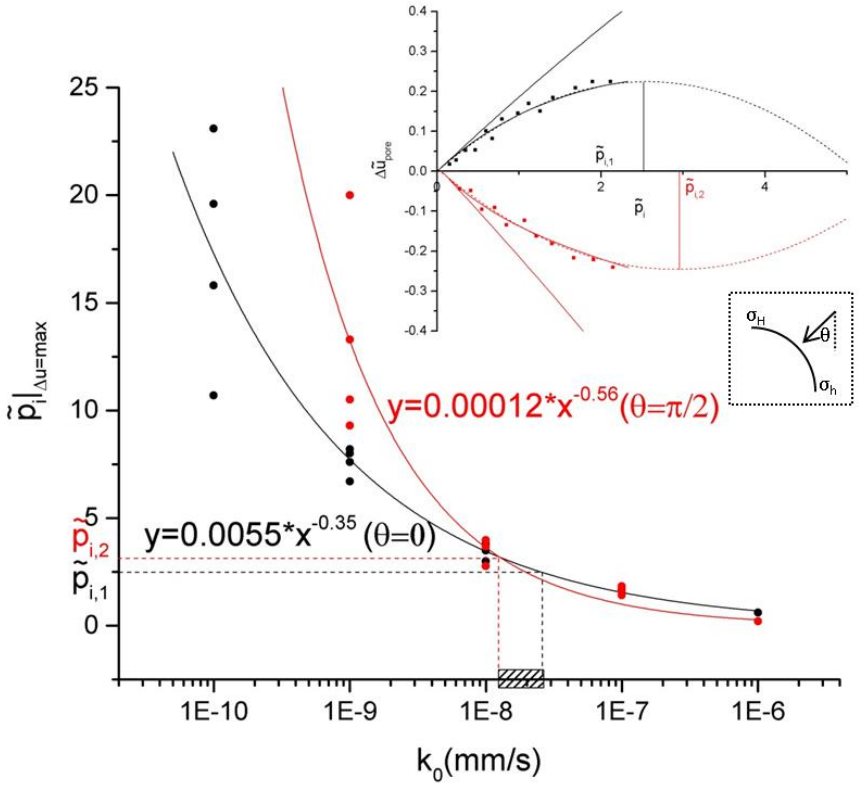

Figure 4-22. The Relationship between the expansion pressure at the maximum excess pore pressure and the in-situ permeability. The random scatters in the upper right plot mimic the data obtained from a field test.

It is important to note that the approach introduced above is based on the results of simulation on unyielded element. Severe shearing by borehole drilling that happened before the expansion may significantly affect the initial field and the pore pressure response will be different. However, the damage at the well azimuth parallel to the maximum in-situ stress is always minimum. Thus, it is

suggested that the pore pressure response at θ=0 should be primarily interpreted if the yielding condition is uncertain.

Conventionally, permeability can be determined by both laboratory testing (oedometer test and permeameter test) and field testing (SBP holding test, slug test, packer test). For the laboratory measurement, the permeability of a sample is usually reduced by smearing process during the sample recovery and the scale effect also leads to the underestimation of the in-situ permeability which is highly sensitive to the degree of heterogeneity in the ground (Schulze-Makuch et al., 1999). In-situ testing can be more reliable but the test needs to be carefully managed in order to minimally damage the target section. Particularly, the pumping rate should be under rigorously controlled. Otherwise, the pocket would sustain an irreversible deformation and the observed response would not only be a result of permeability but also the consolidation (Hawkins and Whittle, 1999). The proposed method could avoid direct contact of pumping fluid to the formation, which creates a safe and reusable testing environment.

4.2.3 Effective Stress Path

The pore water drainage also affects the effective stress paths in the cavity periphery. A highly permeable medium allows all the excess pore pressure to dissipate. An effective wellbore filter will also create such a condition. In the drained vicinity, the circumferential stresses all around the annulus tend to become equal with membrane expansion (Figure 4-23). The increase of mean effective stress under the drained expansion in all axes makes the soil more compacted and resisted to shearing.

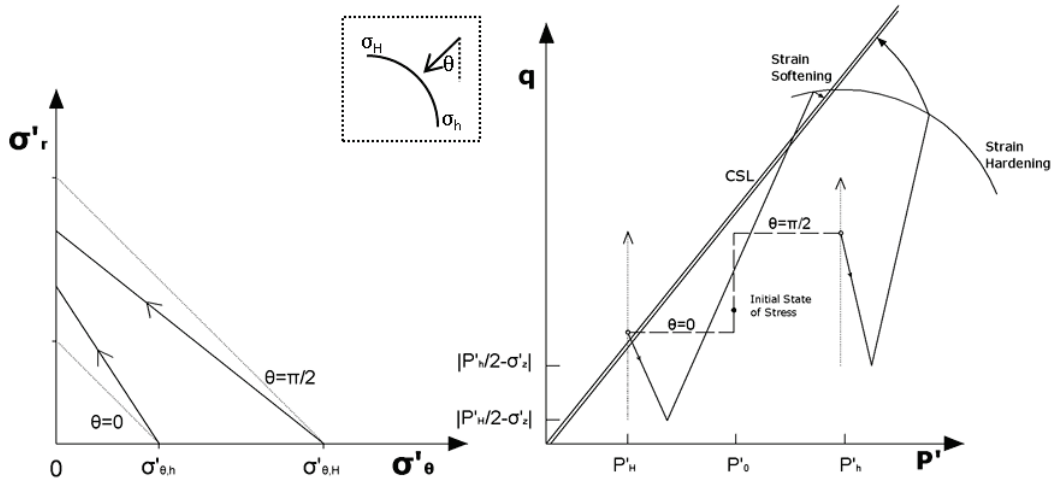

Figure 4-23. The stress paths for the cavity expansion in the drained condition (solid lines). The stress paths in the undrained condition are shown as the dotted lines.

5 Simulation of Pressuremeter Testing in the Anisotropic Stress Field

5.1 Mechanical Property of Packer Membrane

The expandable section of the pressuremeter is a layer of tough rubber membrane with internal multiple caliper fingers used to measure the expansion of the membrane. The membrane is evenly distributed on the instrument and is trapped by the steel clamp rings on its ends. The weakest part of membrane is where it has been locked by clamping rings. In order to prevent it from bursting by the tension induced from the expansion, a short cone of steel fingers are placed 10 cm up to the junction point. The expanding length is covered with a sheath of steel strips which protects the membrane from contacting the borehole surface. The steel sheath is axially stiff but radially flexible and detached from the membrane when the tool is at rest.

Unlike the hydraulic fracturing, the pressuremeter does not allow the injecting fluid to directly interact with the ground. The expansion is constrained by the stiffness and compressibility of membrane. Thus, if the injection pressure is used to make an interpretation, it would lead to the inaccuracy, which may be more severe in the case of non-uniform expansion such as testing in the anisotropic initial stress field.

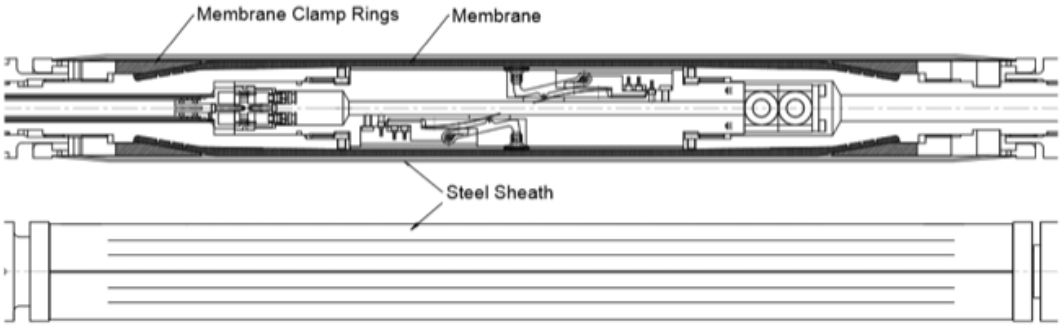

Figure 5-1. The inner mechanical design (upper) and outside view (lower) of the central part of the pressuremeter

5.1.1 Traditional Membrane Calibration

The calibration of the membrane for the pressuremeter expansion consists of two components – membrane stiffness and membrane thinning. The stiffness of membrane results in the difference between the readings from the pressure cells and the net stress being applied to the borehole wall. Its effect becomes dominant when the testing is performed in soft materials in which the pressure induced by the membrane is comparable to the injection gas/fluid pressure. Conversely, the membrane thinning is the main source of discrepancy found in the readings of radial displacement, especially for the test in the stiff materials where the expansion is relatively small.

For the convenience of engineering practice, the correction regarding two factors mentioned above are respectively achieved by doing laboratory calibration – pressurise the instrument in air at the normal expansion rate and by doing simple mathematical manipulation. Though the rubber membrane has a nonlinear expansion (Figure 5-2), usually a linear relation between pressure and radial displacement is assumed so that it can be applied to quick calculations.

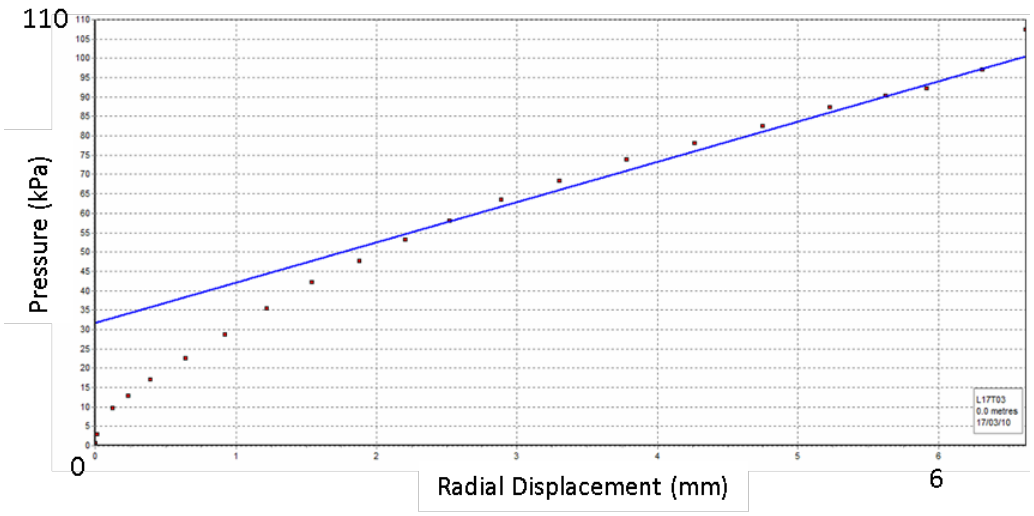

Figure 5-2. The expansion curve for the calibration of membrane stiffness

The net expansion pressure on the borehole wall could be corrected by subtracting the membrane restraint at a particular strain. However, the membrane may expand unevenly in the non-uniform boundary loadings which is different from the way it has been calibrated. The membrane restraint is not azimuthally equal. Thus, the linear relation for membrane stiffness is not applicable for this class of problems.

In this section, the mechanical property of the membrane is evaluated from the constitutive perspective, and the simulation is performed to investigate the non-uniform expansion of membrane interacting with the borehole surface under the condition of initial stress anisotropy.

5.1.2 The Constitutive Description of Membrane in Expansion

Since the thickness of the membrane is less than the inside radius of the instrument, the thin walled cylinder theory could be employed to find the stresses in the membrane (Figure 5-3). Inflating the instrument tends to stretch the membrane by a small amount if there are not constraints at the ends of the vessel. However, in the membrane calibration, the tool is gripped by vice grips at one of the ends with the other freely held but axially restrained by the rigid

instrument body. Thus, under low loading condition, it is assumed that the axial strain is zero.

The circumferential and radial stresses are expressed as

$$\sigma_\theta = \frac{p_i r}{t_r}$$
$$\sigma_r = p_i \tag{5.1}$$

It's worth noting that although the membrane is sufficiently thin, the thickness t_r is still comparable to the dimension of cylinder (d/t_r<10), so σ_r should not be ignored. The axial stress could be calculated under the assumption of $\varepsilon_a=0$,

$$\sigma_a = p_i \nu (\frac{r}{t_r} + 1) \tag{5.2}$$

Thus, the elastic strain rate can be determined by Hoek's theory,

$$\dot{\varepsilon}_\theta = \frac{\dot{p}_i}{E t_r}(1+\nu)\left[r(1-\nu) - \nu t_r\right]$$
$$\dot{\varepsilon}_r = \frac{\dot{p}_i}{E t_r}(1+\nu)\left[t_r(1-\nu) - \nu r\right] \tag{5.3}$$

Rewriting the Eqn(5.3), the Young's modulus E and Poisson's ratio ν at a particular expansion pressure p_i could be expressed as a function of strain rate,

$$E = \frac{\dot{p}_i (r - t_r)\left[r(\dot{\varepsilon}_\theta - 2\dot{\varepsilon}_r) + t_r(2\dot{\varepsilon}_\theta - \dot{\varepsilon}_r)\right]}{t_r (r + t_r)(\dot{\varepsilon}_\theta - \dot{\varepsilon}_r)^2}$$
$$\nu = \frac{\dot{\varepsilon}_\theta t_r - \dot{\varepsilon}_r r}{(r + t_r)(\dot{\varepsilon}_\theta - \dot{\varepsilon}_r)} \tag{5.4}$$

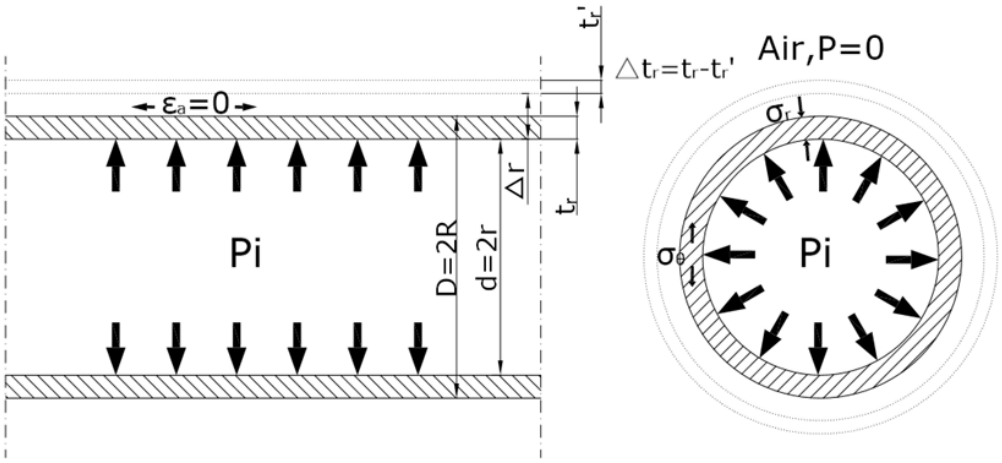

Figure 5-3. The infinite-length thick-walled cylinder theory for membrane expansion

For the hyperelastic material, *E* and *v* are both strain dependent. In order to better describe this nonlinear behavior mathematically, the Neo-Hookean model is applied (Yeoh, 1993). The strain energy density function is introduced as

$$U = C_{10}(I_1 - 3) + D_1(J-1)^2 \tag{5.5}$$

where C_{10} and D_1 are the material parameter for a particular kind of rubber; C_{10} is equal to half of the initial shear modulus, which is also a function of initial Young's modulus: $C_{10}=E_{ini}/(1-2v)$. For an incompressible material, these two parameters can be simply calculated as $C_{10}= E_{ini}/6$ and $D_1=0$. In a short period of expansion at beginning, $\dot{\varepsilon}_\theta \approx (\Delta r - 0)/r$, $\dot{\varepsilon}_r \approx -(\Delta t_r - 0)/t_r$ and $\dot{p}_i \approx p_i - 0$. The initial modulus E_{ini} can be calculated by Eqn(5.4) .

In the formulas above, p_i and Δr are monitored during calibration; r and t_r are the instrument constants; $\Delta t_r = \Delta r + R - \sqrt{R^2 + \Delta r(2r + \Delta r)}$ by assuming to a first approximation that the cross-section area of the membrane remains constant.

5.1.3 Calibration for Hyperelastic Constants

In order to enhance the accuracy of the constitutive parameters determined by the membrane calibration, an aluminum sleeve (Figure 5-4) with larger diameter

than usual is used which allows membrane to expand to the maximum range (an individual strain finger can measure up to 16mm). The calibration of strain finger and pressure cell should be done prior to inflating up the membrane. However, error is still unavoidable due to other factors, e.g., the instrument will move about inside the cylinder - its center will not be in the same axis of the cylinder.

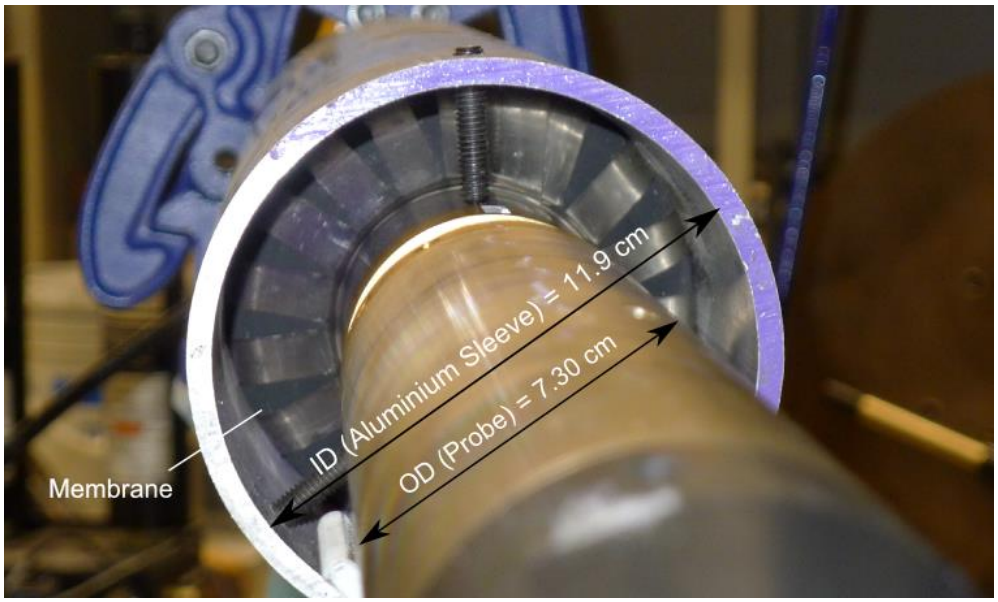

Figure 5-4. The dimension of the protective sleeve for the calibration of mechanical properties of membrane.

The typical curve for the whole process of expansion and contraction of membrane is shown in the Figure 5-5. It is interesting to notice that the contraction doesn't get back in the same way as it expands. The "Mullins effect" provides a rational explanation – a cyclic softening has taken place due to the microstructural change at a large expansion. This phenomenon is common to all rubbers and it shows the viscoelastic nature of polymer materials. This behavior could be mathematically described by the damage functions established by Ogden and Roxburgh (1999), but this will not be within the scope of our study.

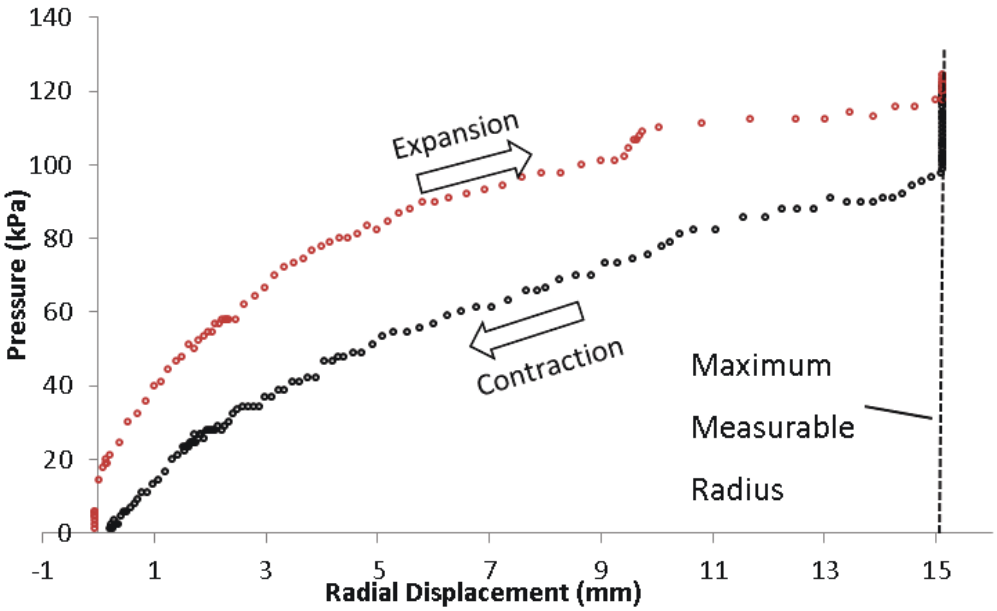

Figure 5-5. The expansion and contraction curve of the membrane calibration

The strain-dependent membrane modulus is calculated based on the test results from several runs of the calibrations (Figure 5-6). Only the initial variation is valid to estimate the true modulus of the membrane. The calculated Poisson's ratios are also varying but in a small range close to 0.5 which verifies the assumption of the incompressibility of the material. Accordingly, we can have rough estimates of the constitutive parameters of the membrane, say, $C_{10}\approx 5/6=0.83$ and $D_1\approx 0$.

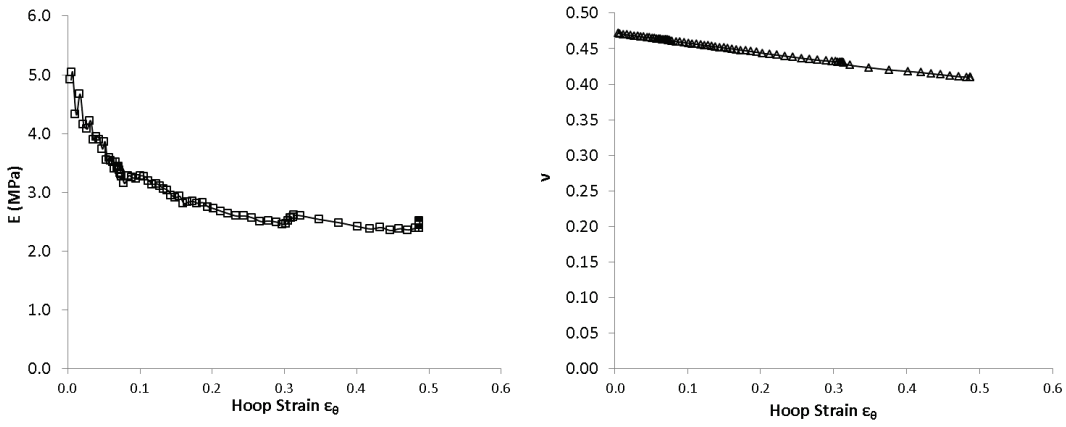

Figure 5-6. The variation of Young's modulus and Poisson's ratio (calculated by Eqn (5.4)) as membrane expands against air.

5.1.4 The FEM validations

Different loading rates were chosen with the intent of discovering the impact of strain rate dependency, but only a minor difference was observed (Figure 5-7). An FEM model was also established in the same dimension of the calibration. By adjusting the estimated value of the C_{10} slightly, we found the best fitting expansion curve for the test data. It is validated that the C_{10}=0.75 can be used to simulate the membrane expansion against the non-circular opening of borehole.

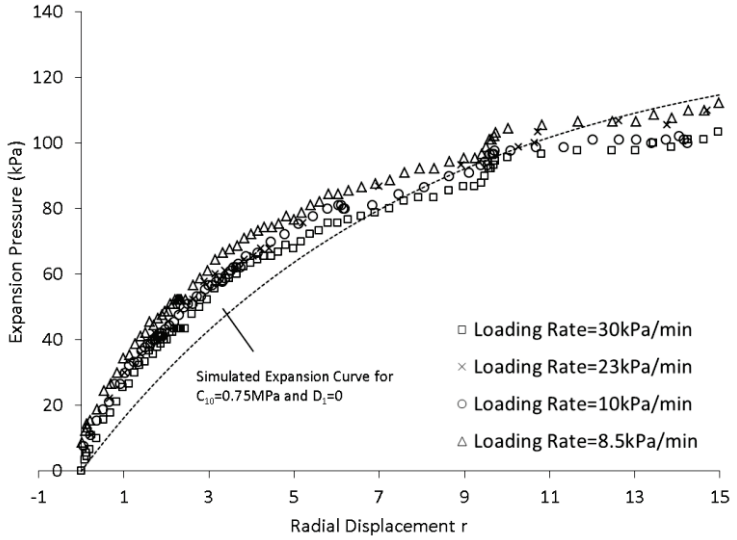

Figure 5-7. The comparison between the expansion curves of the test data at varying loading rates and the one computed by FEM simulation.

5.2 Interaction between Membrane and Soil

5.2.1 Contact Formulation

In Abaqus, there are various contact enforcement methods to establish the contact constraints between multiple independent simulation bodies. In our case, the outer surface of membrane tends to contact the cavity surface under a certain amount of expansion pressure and the virtual work contribution associated with the interaction are included in the system of equations in these two FEM domains.

There are two key characteristics in the contact formulation – normal contact constraint and frictional contact constraint.

5.2.1.1 Hard Contact

The hard contact is defined for the interaction between two objects where there are no penetration between their contact surfaces (Figure 5-8). It enforces a rigorous constraint while numerical convergence might be difficult sometimes because the contact stiffness is switched in two extremes – zero when objects are separate and infinite when objects are connected. Usually, Lagrange multiplier **λ** is introduced in the energy equilibrium equation as another degree of freedom to enforce the constraint:

$$\begin{bmatrix} \mathbf{K} & \mathbf{C}^{\mathrm{T}} \\ \mathbf{C} & 0 \end{bmatrix} \begin{Bmatrix} \mathbf{u} \\ \boldsymbol{\lambda} \end{Bmatrix} = \begin{Bmatrix} \mathbf{f} \\ 0 \end{Bmatrix} \tag{5.6}$$

where **K** is the stiff matrix for the unconstrained system, **C** is the constrained matrix in the mixed formulation, **u** is the displacement tensor and **f** is the external force .

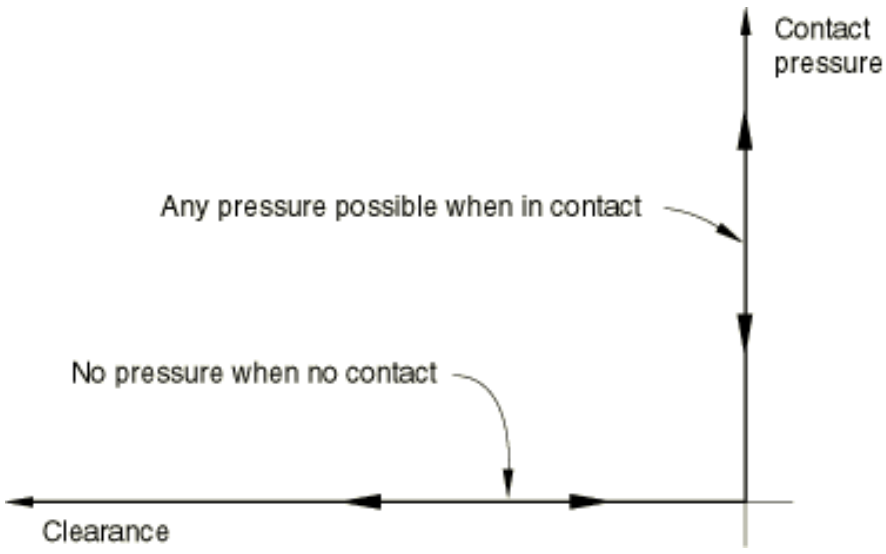

Figure 5-8. The schematics of hard contact for the contact enforcement

5.2.1.2 Coulomb Friction

Interfacial shear stresses may develop between two objects when they have rough surfaces, and if the shear stress exceeds the friction limit then two surfaces will have tangential movement or slip. To simulate the frictional slip in the case of membrane-soil interaction, Coulomb friction model is formulated to predict whether the contact node is sticking or slipping (Figure 5-9). The friction limit is:

$$\begin{aligned} \tau_{\max} &= \mu p, \tau_{\max} < \overline{\tau}_{\max} \\ \tau_{\max} &= \overline{\tau}_{\max} \end{aligned} \tag{5.7}$$

where μ the friction coefficient can be the function of slip rate, normal stress, and other field variable, such as temperature, but here it is assumed as a constant in the calculation; $\overline{\tau}_{\max}$ is often taken as the yield stress of materials by shearing and it is assigned an extremely high value in this study.

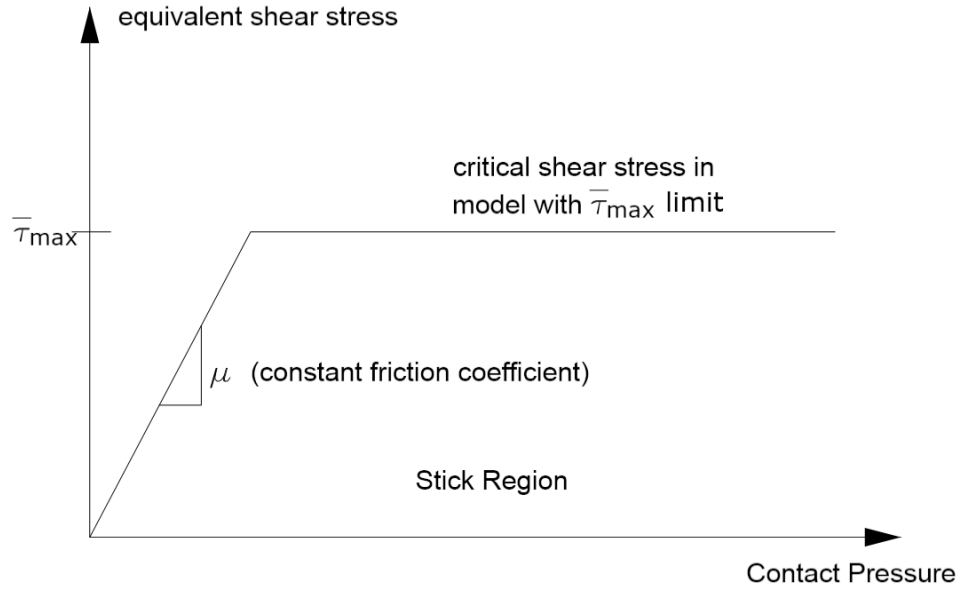

Figure 5-9. The schematics of Coulomb friction model

The Lagrange multiplier method, which rigorously prohibits the slip in the stick region is enforced to solve the shear stress and frictional slip between the contact surfaces in this study.

5.2.1.3 Solving Algorithm

Solving the problem with the contact constraints starts with the initial conditions of each individual contact components, and the stiffness of contact is calculated accordingly. The constraint system of equation is then established and solved iteratively. If the solution has converged then update the new contact configuration and proceed for the next increment of loading/displacement. Otherwise, the increment size needs to be reduced for another trial. The entire workflow for the computation of contact simulation is illustrated in Figure 5-10.

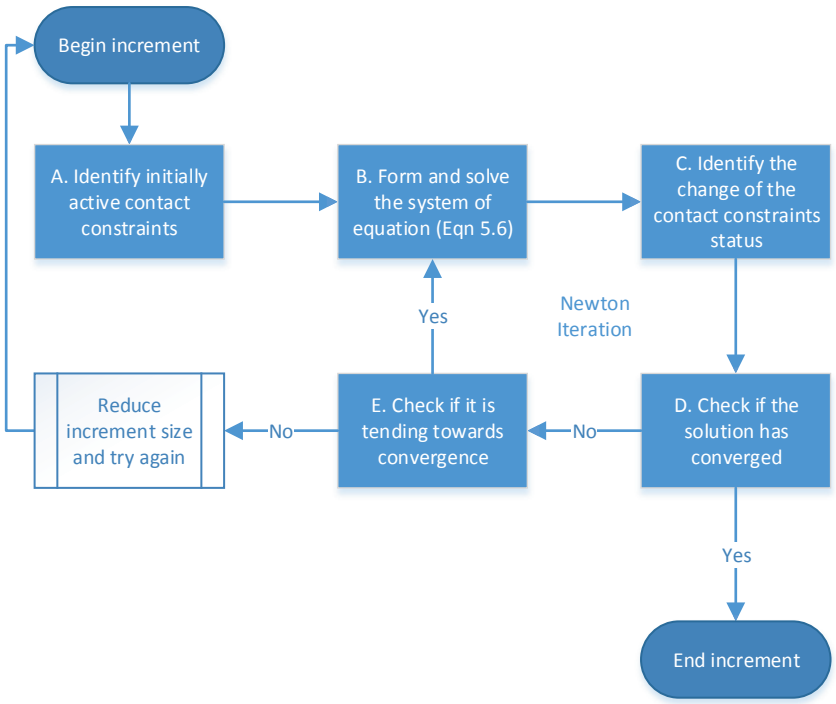

Figure 5-10. Workflow of solving the contact problem

5.2.2 The Initial Contact

Since the shape of borehole induced by drilling is not circular, a uniformly expanded membrane will touch the cavity surface at different time. Depending on the stiffness of the soils, there are two types of initial contact between membrane and borehole wall (Figure 5-11). As indicated in Chapter 3, for the relative stiff material, soil would converge most at the azimuth of σ_H where the expanding membrane will reach the cavity surface first (Figure 5-11, A). By contrast, if shearing is triggered at the side by drilling, the convergence would be more evident at the azimuth of σ_h due to the post-peak dilation, in which case, the initial contact happens at two horizontal axes almost at the same time (Figure 5-11, B). The drilling-induced wall displacement in the yielding borehole is orders of magnitude higher than that in an unyielding borehole, so less initial expansion is required for the membrane to fully contact cavity surface in the same size of borehole. Generally, the borehole expands more in the azimuth of σ_H as soil has more plastic deformation in such direction. It was also shown in the poorly consolidated case, that it is impossible to make a borehole recover to the virgin shape after membrane contracts to the initial status.

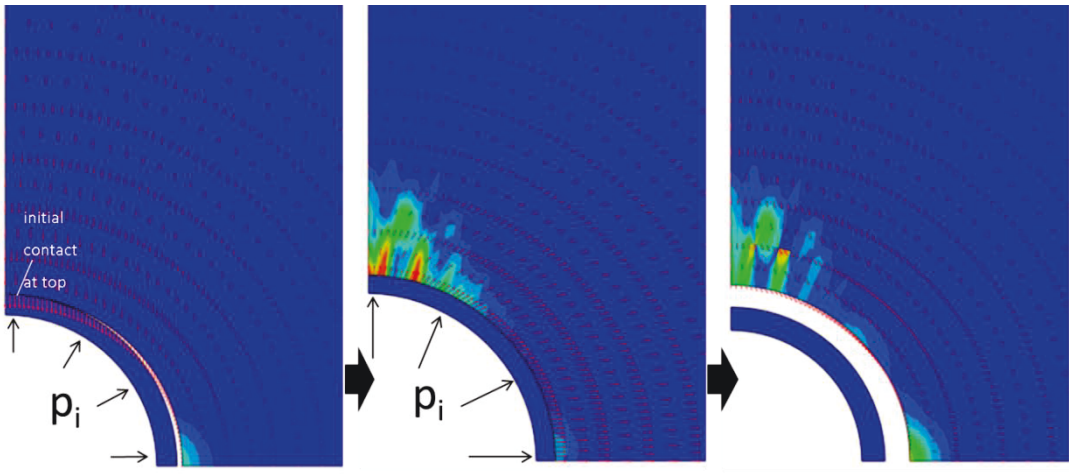

A. Moderately to heavily consolidated Formations (n_p=4)

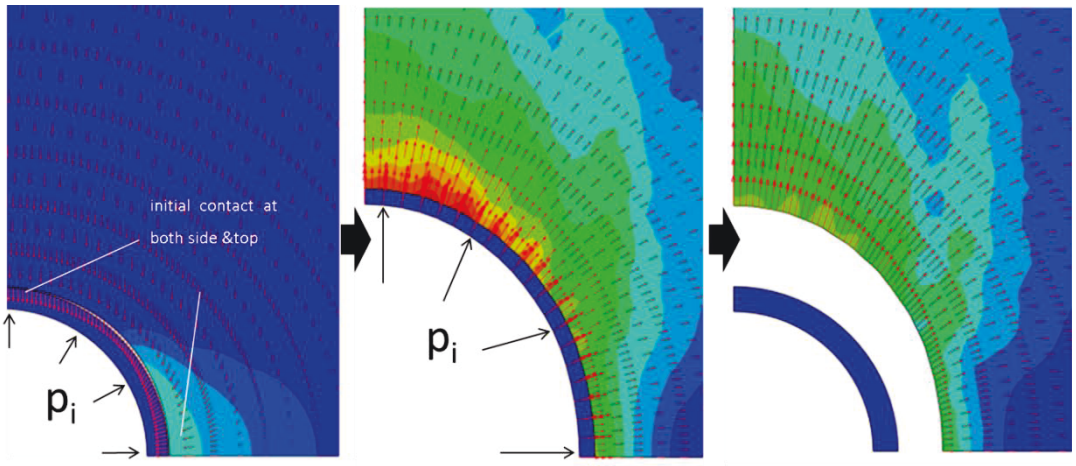

B. Poorly consolidated Formations (n_p=1)

Figure 5-11. The profile of plastic zones at stages of initial contact, maximum expansion and complete contraction (N=2.5)

5.2.3 The Effect of Membrane-Soil Friction

For non-uniform expansion, an important factor governing the interaction of the membrane with the borehole surface is friction. If the surface shear stress exceeds the slip threshold, relative sliding will take place between the membrane and borehole wall. In Abaqus, the Contact module allows the settings of finite sliding and small sliding. The latter is selected as the contacting surfaces only have moderate movement to each other. The slip tolerance is assigned 0.005 indicating that the ratio of maximum elastic slip to characteristic contact surface dimension will be no higher than 0.005.

The friction coefficient μ between the ordinary rubber and concrete varies from 0.45 to 0.85 for the clean surface contact. The rough shale surface is more frictional while the steel sheath cover is less. Figure 5-12 shows the pore pressure variation right after the contact is made for case (a) of Figure 5-11. The top part of the borehole is initially expanded resulting in an instantaneous rise of pore pressure; at the same time, the pore pressure at the side tends to change as well because the partial expansion produces the tension in the non-contact zones. The expansion between the initial contact and full contact has temporary

effect on the pore pressure variation. Under different surface shear stress, the pore pressure change has different responses in the transition. For low or no friction limit ($\mu<0.05$), a plateau was approached after the rapid increase of pore pressure; if the slip is constrained by higher friction limit, pore pressure will have a sharp turn from the increasing trend. The high shear stress accelerates the decrease of tangential stress at the top, by which the mean stress is reduced. The pore pressure thus decreases in the trend of dilation.

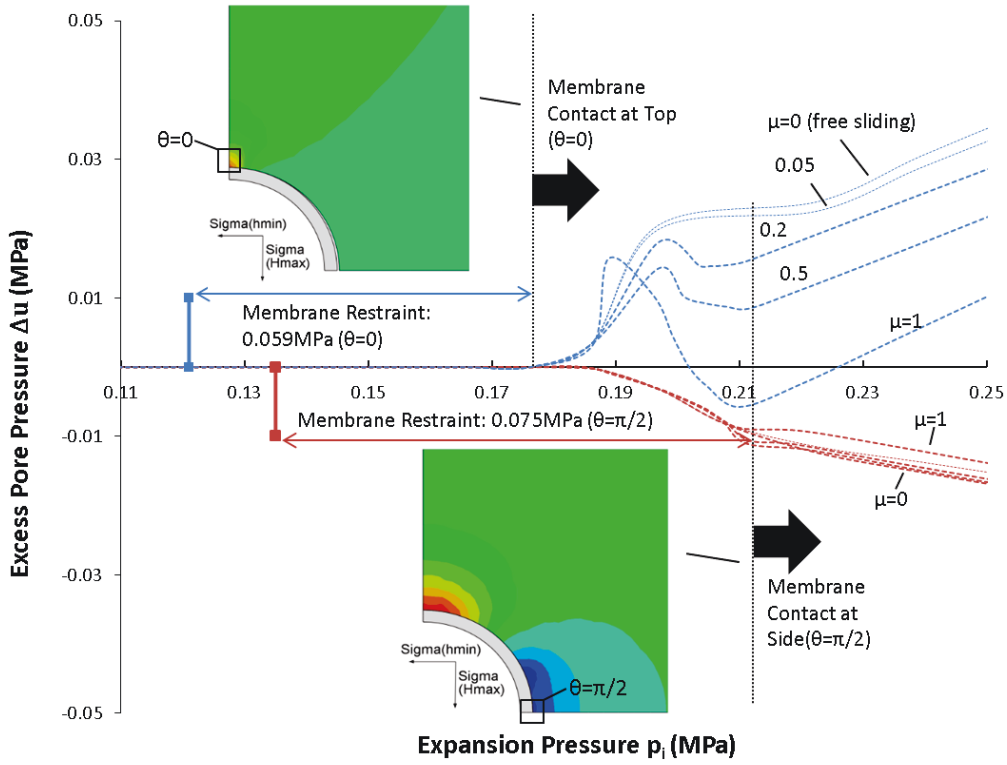

Figure 5-12. The relationship between pore pressure variations and friction coefficient at the beginning stage of expansion

However, the violent fluctuation of pore pressure is not observed in the later stage when the full contact is made (Figure 5-13). The interfacial slip is unlikely to occur under increasing friction. The pore pressure variation as well as the

expansion curves becomes stable and consistent regardless of friction coefficient being defined.

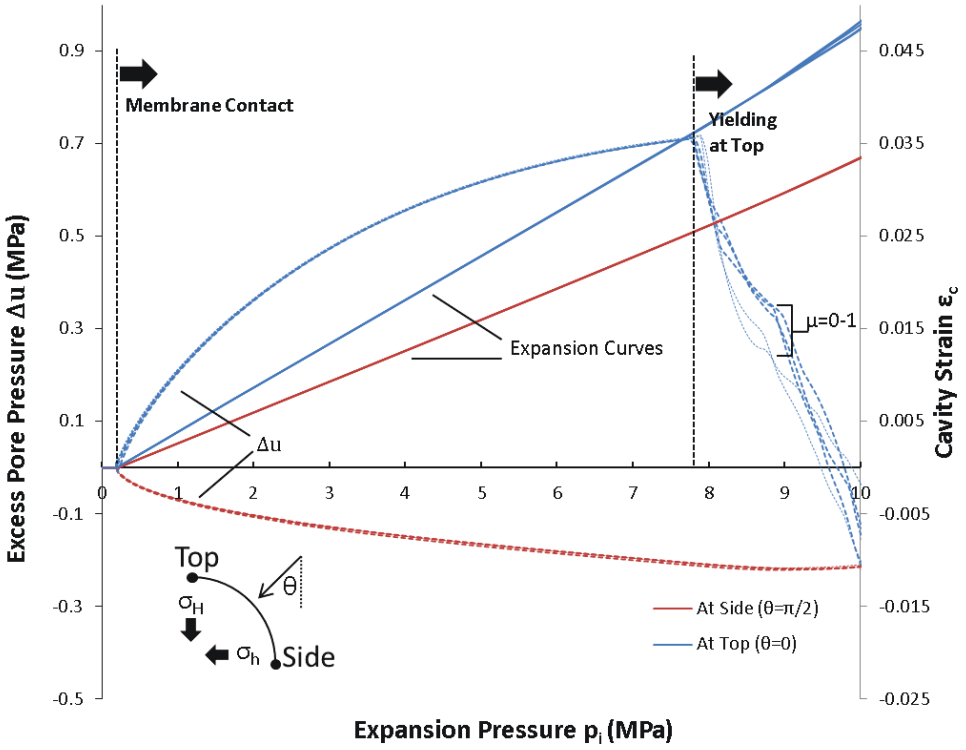

Figure 5-13. The variations of excess pore water pressure and cavity strains responding to different friction coefficients in large scale

5.2.4 The Effect of Membrane Restraint

The inflation is restrained by the membrane at different angles. The expansion at the elastic stage is uniform and firmly resisted by the ground. However, as the material is softened after yielding, the ground is no long capable to sustain the internal loading. Pressure, required to overcome the membrane restraint, increases as membrane further expands (Figure 5-14). The nonlinear and non-uniform stiffness of membrane can't be simplified as a linear function of the average radial displacement.

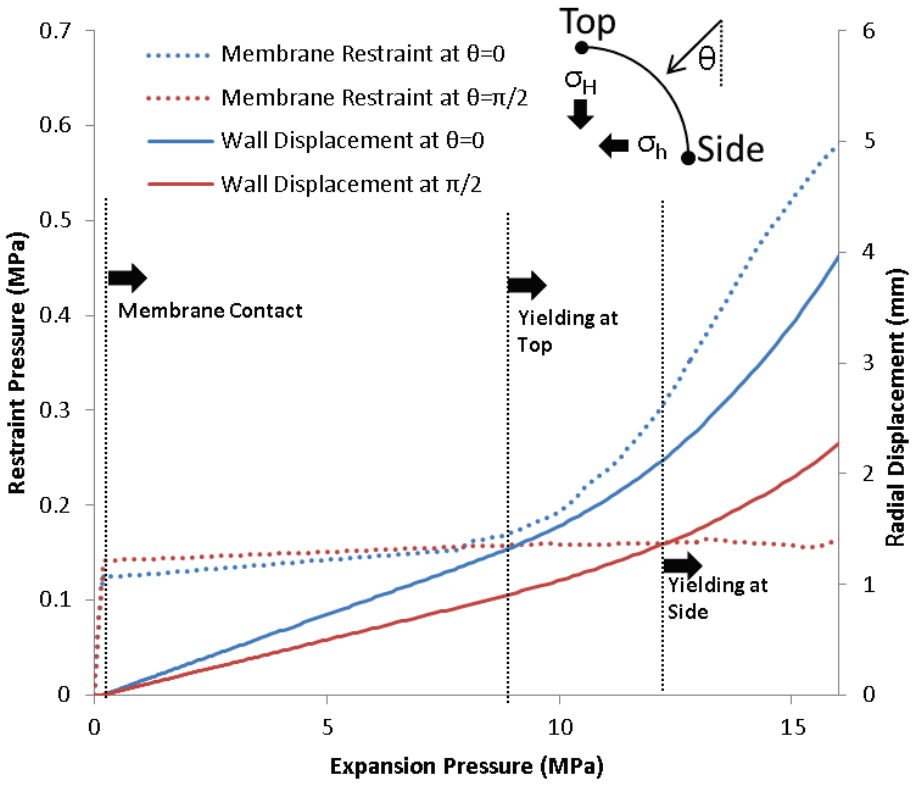

Figure 5-14. The effect of membrane restraint to the expansion pressure and wall displacement

5.3 Simulation of a Cycle of Pressuremeter Testing

Characterised by three parameters, the mechanical properties of the membrane are given in Table 5-1 as inputs in the simulation of pressuremeter testing. The Cam Clay constants for clayshale are calibrated with the triaxial test results. They are listed in Table 5-2 together with a range of values for parameter p_c, N and $\overline{K}$. It is assumed that the vertical stress is 3.4 MPa at the bottom of 170m deep borehole with an average unit weight 20kN/m^3 for the overburden.

Table 5-1. The mechanical properties of inflating packer

Neo-Hookean Hyperelastic Constant		Friction Coefficient
C_{10}	D_1	μ
0.75	0	0.2

Table 5-2. Data for the basic parameters of Clearwater clayshale

ν	κ	λ	Γ	M	k (mm/s)	p'_c (MPa)	N	$\overline{K}$
0.2	0.03	0.075	2.19	1	1e-8	10-30	1-3	0.5-2

5.3.1 Correction to the Instrument Reading

An entire cycle of expansion and contraction is modelled by Abaqus/Standard. An example of simulation is shown in the Figure 5-15. For the purpose of mimicking the actual test log from the field, a free expansion of membrane is also included in the simulation curve. Likewise, the reading from the pressure cell only reflects the fluid pressure being injected into the instrument, which should be distinguished with the net expansion pressure acting on the borehole surface. If the stiffness is calculated directly by the data from the instrument readings, error would be introduced as the thinning of membrane leads to the overestimation of radial displacement. This discrepancy is also seen in the initial section of unloading where elastic contraction takes place.

For a single cycle of testing, the shear modulus obtained from loading and unloading curves are different. The mean effective stress increased after yielding which makes materials rather stiffer than before expansion.

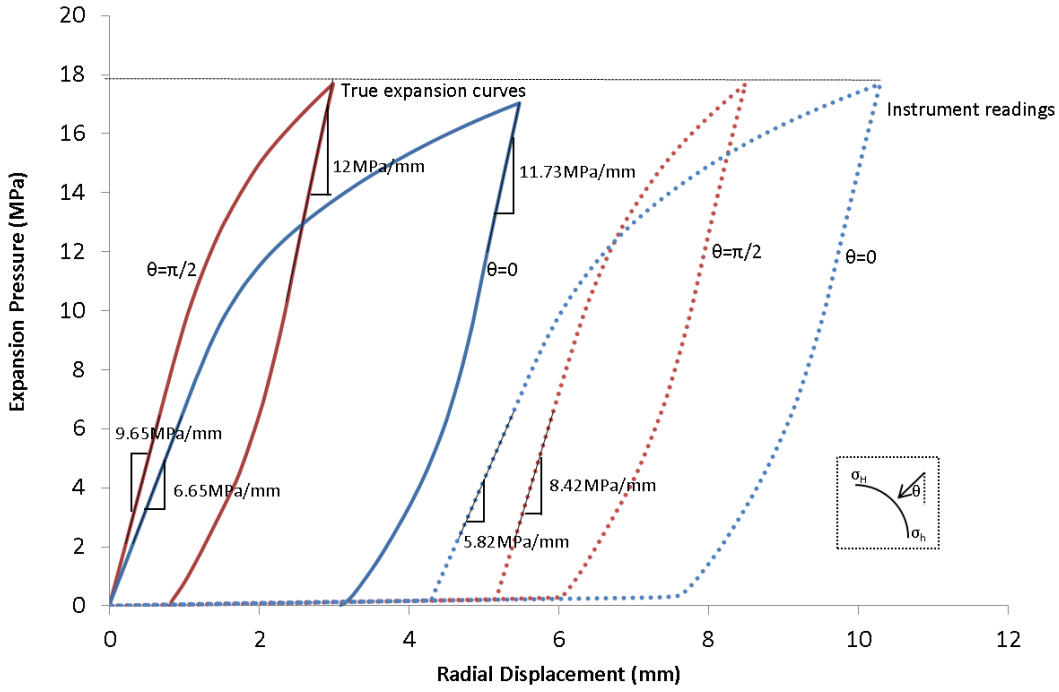

Figure 5-15. The simulated expansion and contraction for a relatively stiff medium under horizontal stress anisotropy of 1.5 (σ'_h=3.4MPa)

5.3.2 The Pore Pressure Variation at Borehole Wall

Understanding the prior stress states for the pressuremeter expansion is essential. Drilling and the consequent relaxation induces a significant stress mobilization at the azimuth of σ_h in poorly consolidated formation. In this class of formation, the internal radial loading may result in similar stress paths at the top and side of boreholes. Also, shearing reduces the moduli by a large amount so the pore pressure responses in these two regions will be in the increasing trend at beginning of loading (Figure 5-16, A; Figure 5-17). Pore pressure will rise dramatically once the yielding initiates. The pore pressure at the cavity surface tends to be uniform at different axes when the maximum expansion is reached. Releasing inflation pressure causes the recovering of material deformation back into elastic phase, and a stable decrease of pore pressure is observed at the initial stage of unloading. It should be noted that tangential effective stress is

increasing as the expansion pressure reduces; active yielding will take place if the deviatoric stress exceeds the shear strength again. As a result, pore pressure drops rapidly. The packer will detach the borehole wall at some point, where the pore pressure is likely to rebound a bit afterwards because of the loss of friction.

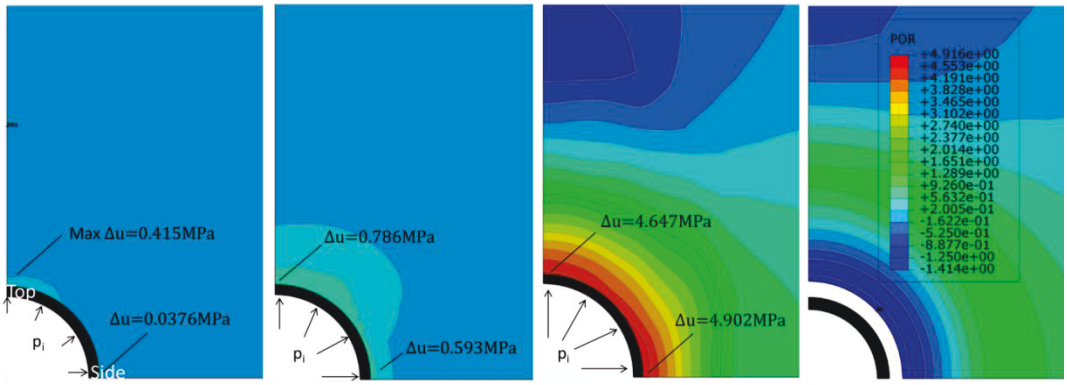

(a) (b) (c) (d)

A. Poorly consolidated formation (n_p=2.2)

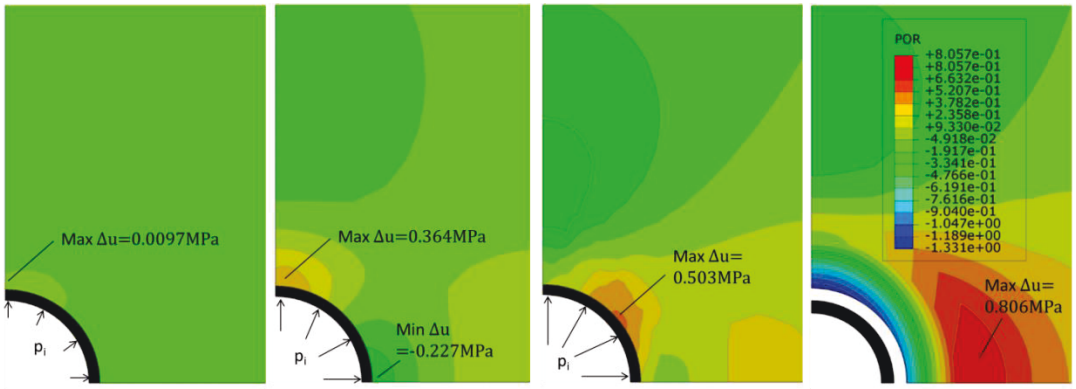

(a) (b) (c) (d)

B. Moderately or heavily consolidated formations (n_p=4.4)

Figure 5-16. The two types of excess pore pressure variation for the pressuremeter testing in the medium in the field of anisotropic in-plane stresses at stages of a) right after the packer contact; b) passive yielding at the top; c) maximum packer expansion; d) the complete release of pressure.

In the more consolidated formations, materials tend to be much stiffer and stable, so borehole is less likely to be disturbed by drilling. Instead, the elements

at the side of the borehole are hardened due to the increase of mean effective stress. Under the hardening effect, pore pressure tends to decrease until material yields by passive loading (Figure 5-18). Thus, the responses of pore pressure at two principal azimuths needs to be distinguished in this case.

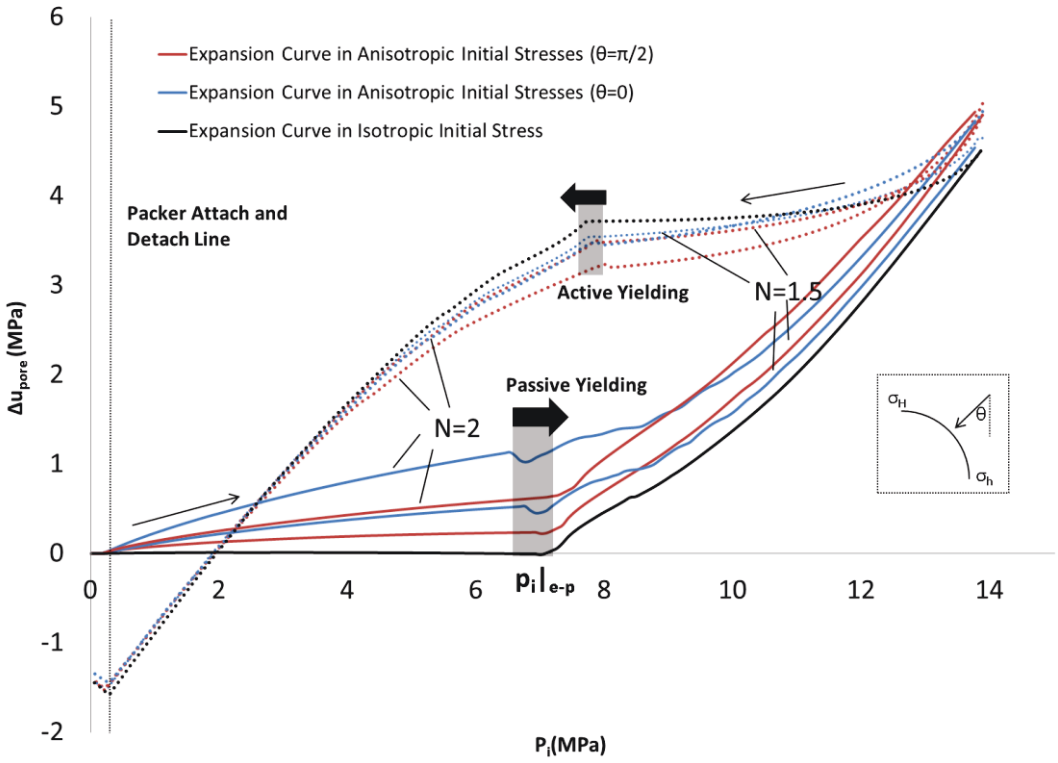

Figure 5-17. The pore pressure variation for the different initial stress anisotropies in the poorly consolidated formations (Type A). (σ'_h=3.4MPa)

While less excess pore pressure is generated by the same magnitude of loading in the highly consolidated formation, the trend of pore pressure increasing inside the medium won't stop even as the probe depressurizes. After an entire cycle of loading and unloading, the maximum excess pore pressure will be reached $2r_0$ away from the center. This is extremely important to realize since the pore water may migrate inward and the inner well structure will sustain the progressive seepage force after the testing.

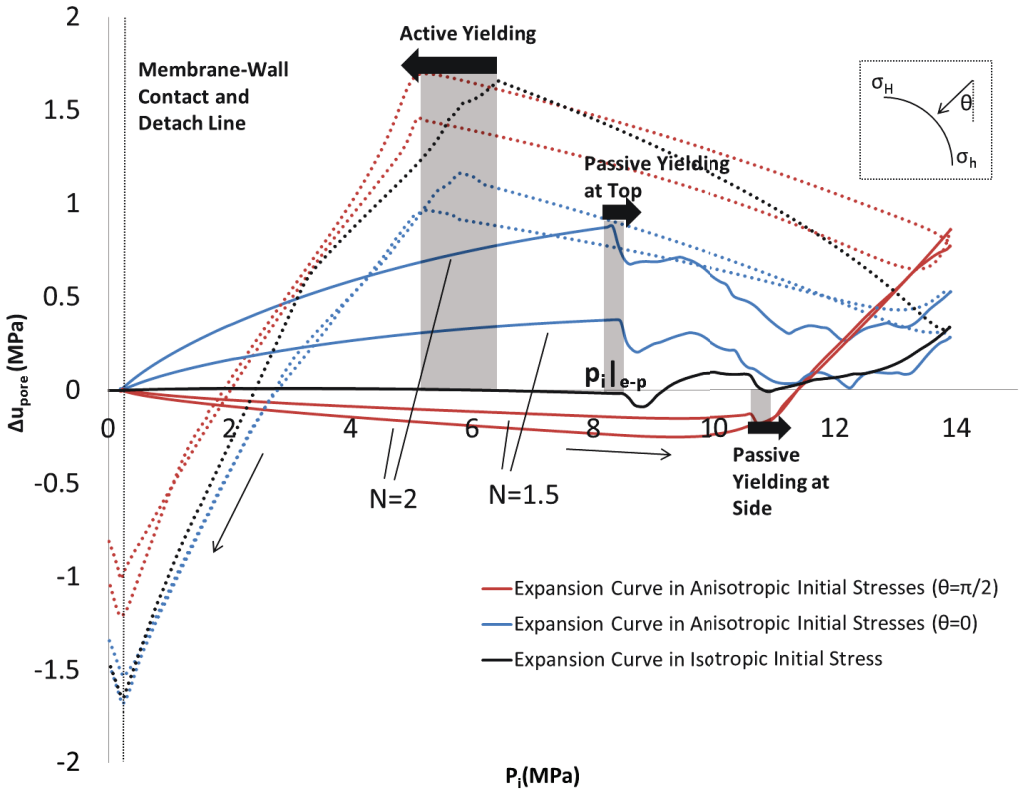

Figure 5-18. The pore pressure variation for the pressuremeter testing in the different initial stress anisotropies in the moderately or heavily consolidated formations (Type B). (σ'_h=3.4MPa)

5.3.3 Pore Pressure Response at Yielding

From Figure 5-17 and Figure 5-18, it is found that the pore pressure variation is relatively similar in the contraction stage regardless of the initial stress anisotropy. Thus, using the contraction curves to match the field data would provide little information on the stress anisotropy. Instead, it might be useful to interpret the soil strength thanks to its uniqueness for a specific value of preconsolidation pressure p'_c. This is promising since the unloading part of the pressuremeter testing is always insensitive to the initial disturbance. However, the approach will not be discussed here, because our primary focus is on the in-situ anisotropic stresses.

Another unique feature for the formation with a particular history of consolidation is the expansion pressure p_i at the inflexion where the material starts to yield at top. This critical pressure is specified as $p_i|_{e\text{-}p}$, corresponding to the critical excess pore pressure $\Delta u|_{e\text{-}p}$. The subscript indicates the transition from elastic deformation to plastic deformation. It is also labelled on the axes in the Figure 5-17 and Figure 5-18.

Figure 5-19 shows the simulated pore pressure responses in the formations which have been consolidated in different degrees. The strong dependences of $p_i|_{e\text{-}p}$ and $\Delta u|_{e\text{-}p}$ upon values of N and p'_c provides motivation for finding a relation for performing parameter inversions explicitly.

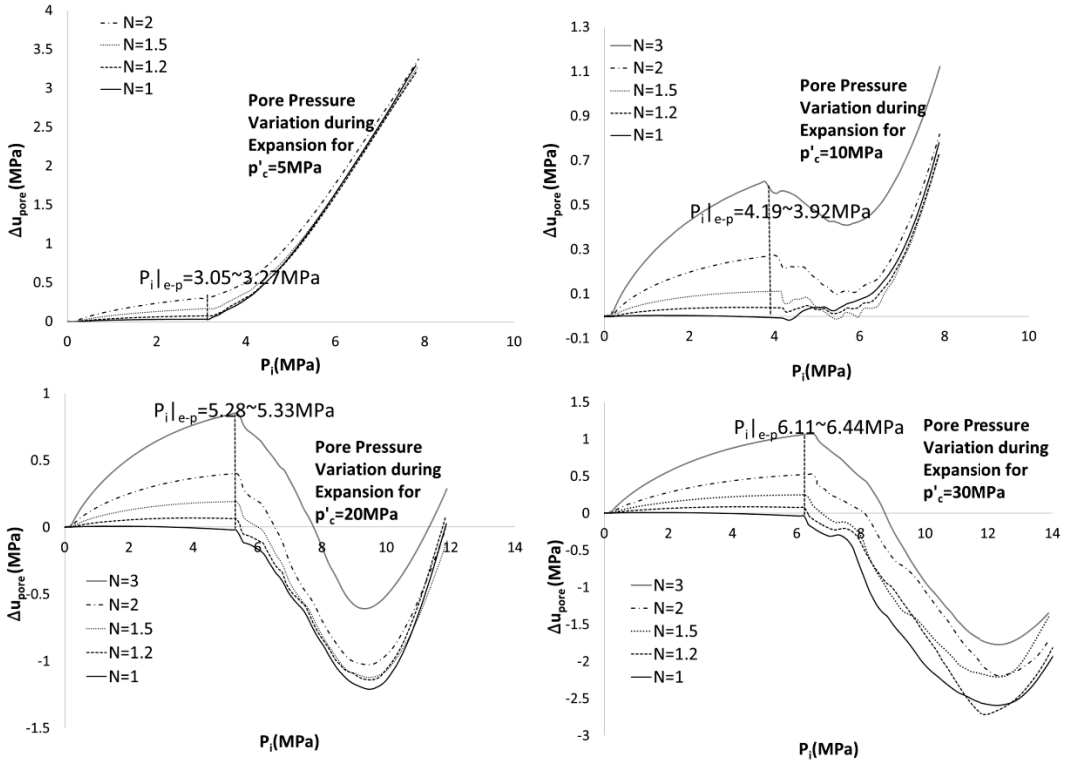

Figure 5-19. The pore pressure variation at the azimuth of maximum horizontal stress during cavity expansion responding to different pre-consolidation pressure p'_c (σ'_h=1.7MPa).

A further parametric study is performed on a range of in-situ minimum horizontal stresses σ'_h from 0.85MPa to 3.4 MPa, and the results are illustrated together in Figure 5-20. Interestingly, the plot of $\Delta u|_{e\text{-}p}$ versus $P_i|_{e\text{-}p}$ are scaled by

the magnitude of σ'_h but geometrically similar to each other. A more general plot is thus introduced by converting the parameters $\Delta u|_{e\text{-}p}$ and $P_i|_{e\text{-}p}$ into two indices - I_{Pi} and $I_{\Delta u}$ for the conformity in scale (Figure 5-21) where,

$$I_{\Delta u} = \frac{3.64 * \Delta u|_{e-p}}{1.03 * \Delta \sigma'_h + 0.05}$$
$$I_{p_i} = \frac{8.05 * (\Delta P_i - 1.62 * \Delta \sigma'_h + 0.03)}{2.25 * \Delta \sigma'_h + 0.28} + 5.44 \quad (5.8)$$

Also, p'_c could be expressed in the dimensionless form of $\frac{p'_c}{\sigma'_h}$, which also reflects the relative strengths of the soils.

For materials of high relative strength, the borehole is unlikely to be sheared at end of drilling. A linear relationship between *N* and $\Delta u|_{e\text{-}p}$ should exist to explain the pore pressure response for the pressuremeter expansion in the unyielded materials. If the borehole vicinity has been disturbed by drilling, pore pressure will also have a great change as a result of expansion especially in the unconsolidated or poorly consolidated formations. This has been already discussed in Chapter 2. Thus, the observed response of pore pressure can provide us more information on whether the borehole has been previously sheared or not.

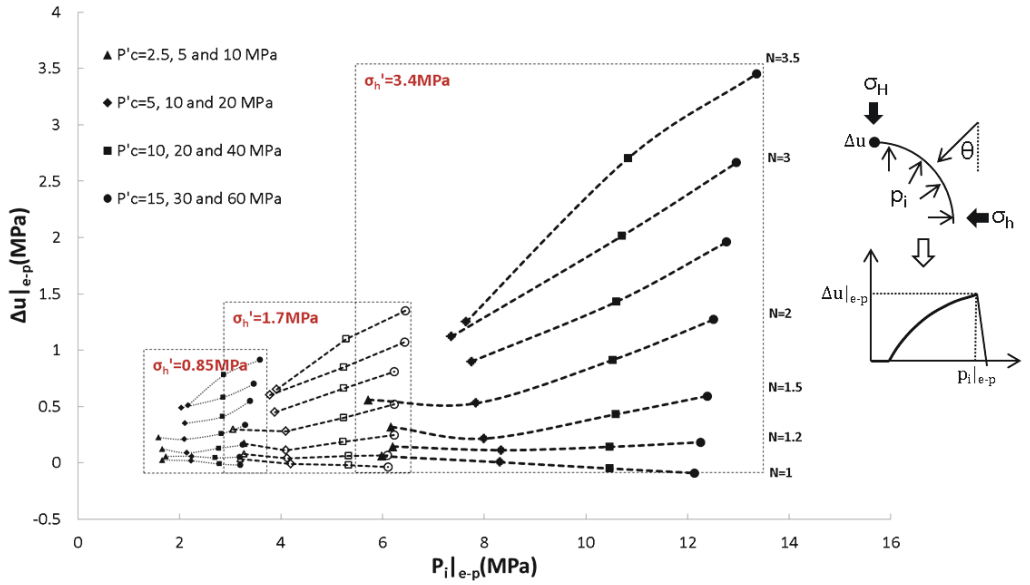

Figure 5-20. The graphical categorization of σ'_h, p'_c and N by plotting excess pore pressure Δu_{pore} against the expansion pressure $p_i|_{e\text{-}p}$ that initiates the plastic deformation.

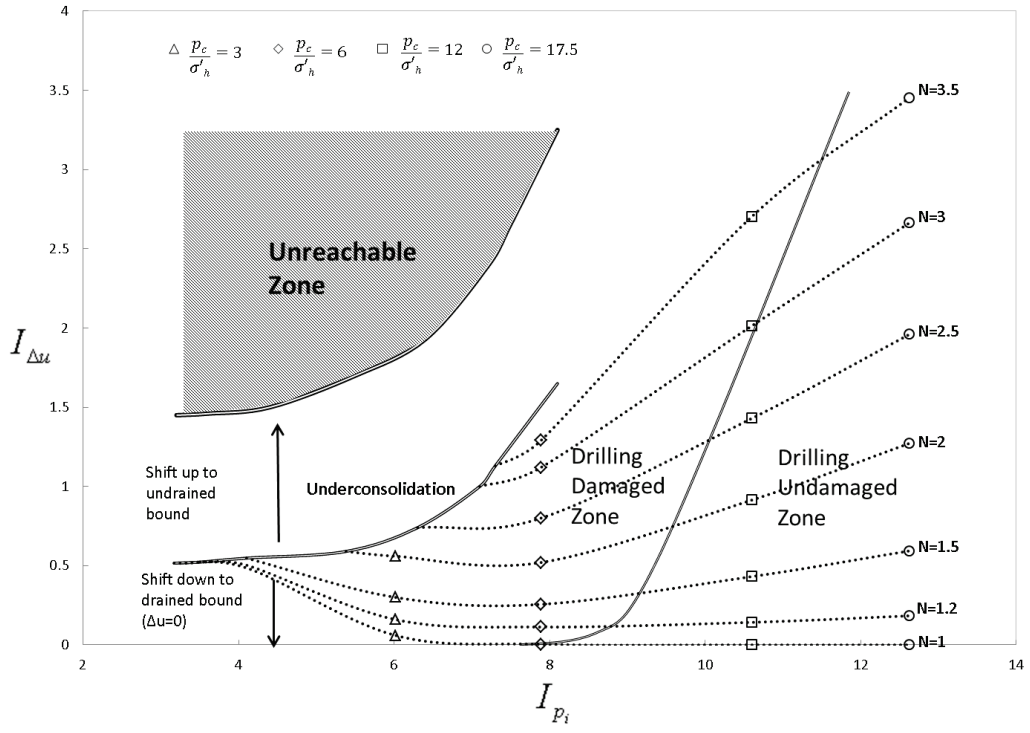

Figure 5-21. The reference chart where $I_{\Delta u}$ and I_{pi} are mapped in response to initial stress anisotropies and relative strengths of formations.

5.3.4 Sensitivity to Other Parameters

It should be noted that the reference chart given in Figure 5-21 is only applicable to the formation whose permeability is around 10^{-8} mm/s. Changing drainage conditions may shift the chart upward or downward. More computations should be repeated to generate the chart for different permeabilities. Not only that, adjusting other modelling parameters such as Poisson's ratio ν and in-situ vertical stress σ'_v will also change the mappings but in a small degrees. In order to find the possible variance caused by these factors, a stochastic simulation with random inputs including M, ν, κ, λ, Γ and σ'_v is scripted and executed in Python 3.3. The script is given in Appendix I.

The instrument readings may vary based on the in-situ material properties as well as the vertical effective stress σ'_v. An example of the variance for the case of ($\frac{\mathbf{p'_c}}{\sigma'_h}$=8.8, *N*=1.5) is shown in the Figure 5-22.

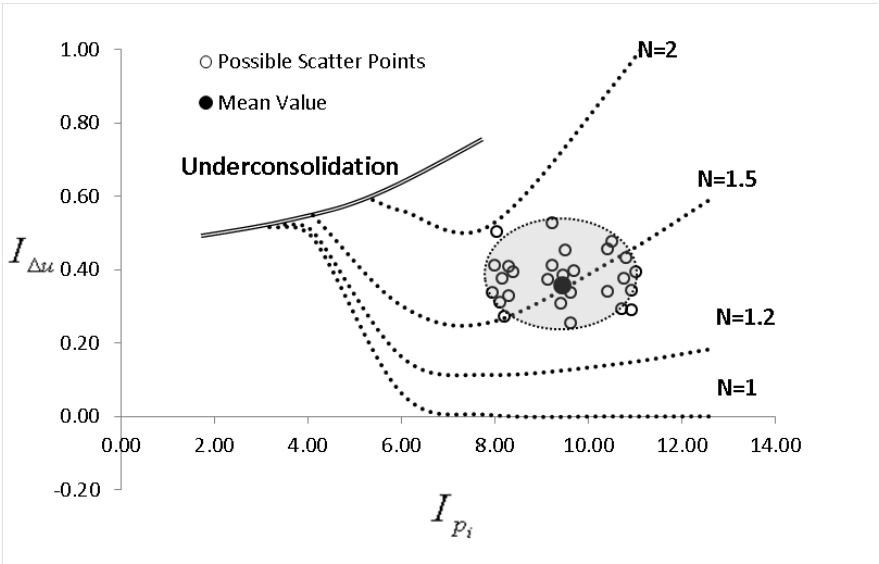

Figure 5-22. The variance of the possible readings dependent of the type of materials and the initial vertical stress. ($p_c^{'}/\sigma_h^{'}=8$, N=1.5)

The variances of the calculated I_{Pi} and $I_{\Delta u}$ in this example are 1.12 and 0.005. It's worth noting that the variance grows wider as the stress anisotropy increases. Herein, a reasonable deviation factor is added to the Eqn(5.8), as

$$I_{\Delta u} = \frac{3.64 * \Delta u|_{e-p}}{1.03 * \Delta \sigma'_h + 0.05} \pm 0.05N$$
$$I_{p_i} = \frac{8.05 * (\Delta P_i - 1.62 * \Delta \sigma'_h + 0.03)}{2.25 * \Delta \sigma'_h + 0.28} + 5.44 \pm 0.7N \quad (5.9)$$

6 Interpretation Methodologies

6.1 Interpretation by Conventional Methods

Sands and clay are the most common materials that have been tested by the pressuremeter in the field. As the drainage conditions are different in these two materials, different methods are applied to interpret their pressure-expansion curves. Usually, Gibson and Anderson method (Gibson and Anderson, 1961) is employed for testing in the clayey materials as undrained expansion would be expected and Hughes' method (Hughes et al., 1977) is preferred for granular materials under drained condition.

However, those methods are both developed under the assumption of isotropic in-situ stress and their applicability and accuracy for the tests in the nonuniform boundary stress conditions are under question. In this chapter, these two methods are examined with the synthetic data from the numerical model developed in this thesis.

6.1.1 Gibson and Anderson Method (Undrained)

The undrained cavity expansion could be written in an equation with initial horizontal stress σ_h and undrained shear strength S_u,

$$p = \sigma_{h0} + s_u\left[1 + \ln\left(G / s_u\right)\right] + s_u\left[\ln\left(\Delta V / V\right)\right] \tag{6.1}$$

where S_u is estimated by the plot of P_I against ln($\Delta V/V$) and σ_h is optimized by performing graphical iteration.

It is suggested that the maximum slope in the P_i : ln($\Delta V/V$) curve be considered as the undrained shear strength. However, the methodology is based on the assumption of expansion in the elastic-perfectly plastic materials. For soils being hardened or softened after the apparent peak, the undrained yield strength and shear strength should be evaluated separately. Usually, several sections of slope

are concatenated in the *Pi* : ln(*ΔV/V*) plot, for example in the case of an isotropic expansion in the heavily consolidated formation (Figure 6-1, Left). The initial inflexion in the stress-strain curve is taken to calculate the yield strength, such as Point I in the Figure 6-1, while the ending section of the slope is most likely the shear strength where the critical state has been reached, such as Point IV, which is also lower than the peak strength.

Knowing the yield strength from the plot of *Pi* : ln(*ΔV/V*), the in-situ horizontal stress could be estimated in the expansion curve (Figure 6-2).

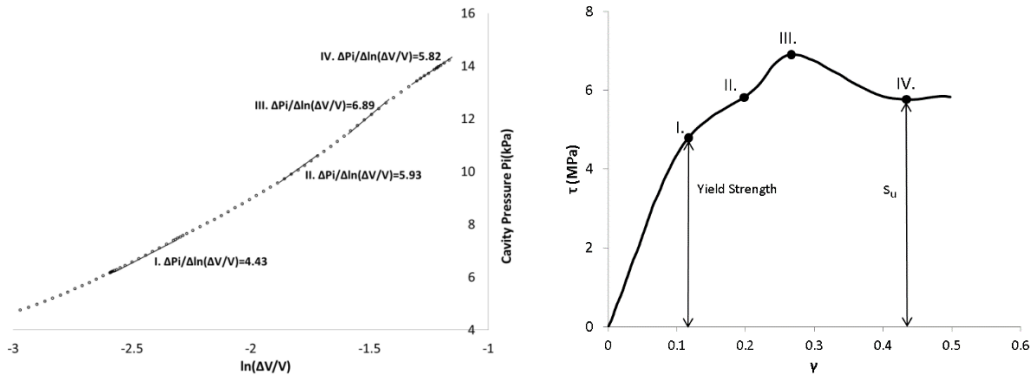

Figure 6-1. The calculated strengths from the Pi : ln(ΔV/V) curve (Left) and the corresponding loci in the stress strain curve (Right).

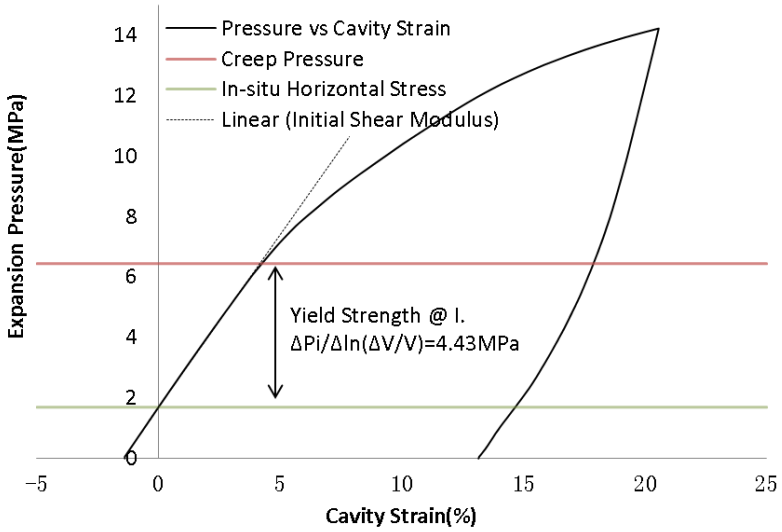

Figure 6-2. The Gibson and Anderson's interpretation on the typical expansion curve for only one cycle of loading and unloading

It is concluded from Chapter 3 that the borehole is unlikely to form in the circular or even elliptical shape (if post-peak dilation occurs) when subject to the non-hydrostatic boundary loadings. The radial displacement should thus be separately evaluated to distinguish the deformation at different axes. However, within the theory of uniform expansion, an automatic averaging is usually performed before the interpretation and only a single expansion curve is used and analyzed.

Figure 6-3 and Figure 6-4 show the results interpreted using the averaged expansion curve obtained under the given stress anisotropies. The interpretation is carried out in the standard procedure of Gibson and Anderson's method which has been described above.

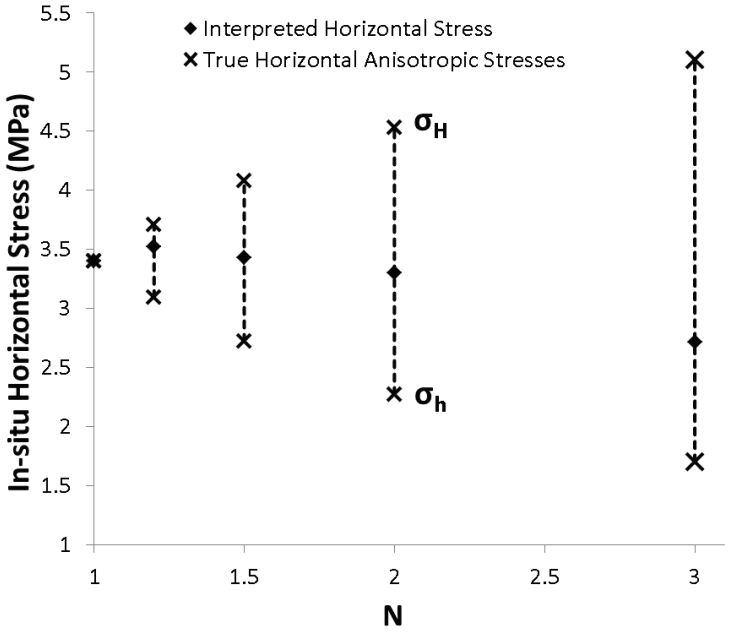

Figure 6-3. The error caused by using conventional method (Gibson & Anderson method) to interpret initial horizontal stress

The interpreted horizontal stress only slightly deviates from the mean value of σ_H and σ_h at low anisotropy level, while the in-situ stress might be underestimated in the presence of high stress anisotropy. The undrained shear strength would

be overestimated if the conventional method is applied with the maximum error of 10.5%.

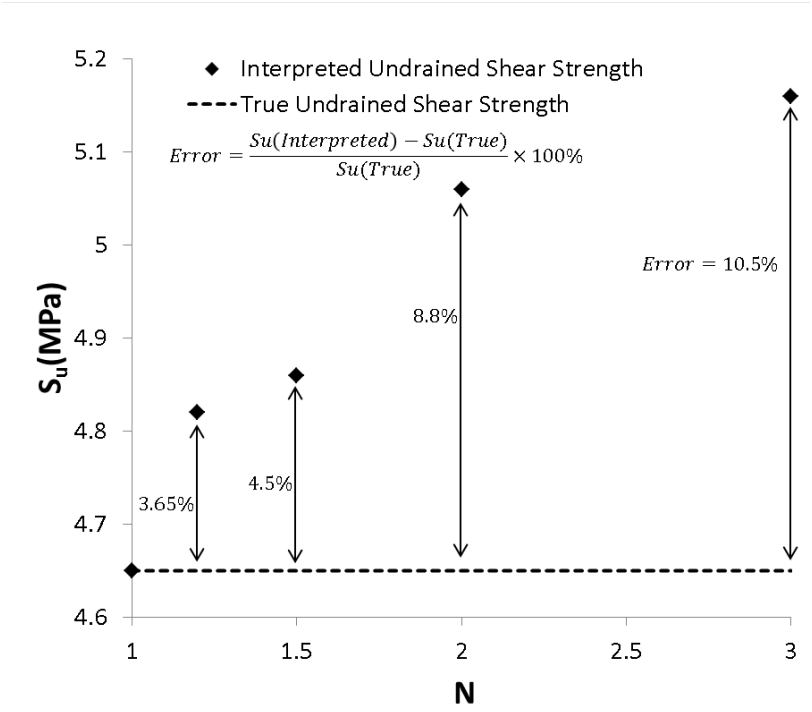

Figure 6-4. The error caused by using conventional method (Gibson & Anderson method) to interpret undrained shear strength (right)

6.1.2 Hughes' Method (Drained)

Hughes's method is applicable to the fully drained expansion. The post-peak dilation is taken into account by establishing the relationship between volumetric and shear strains based on Rowe's dilatancy law. The parameters including critical state angles φ_{cv}, the effective in-situ horizontal stress σ'_{h0} and shear modulus G are required to generate the theoretical expansion curves by equation given by Withers et al (1990),

$$p'_i = \left[2\sigma'_{h0}/(1+N)\right]\left[(\mathrm{G}/\sigma'_{h0})(1+n)\frac{(1+N)}{(1-N)}\varepsilon_c + \frac{(1-n)}{2}\right]^{(1-N)/(1+n)} \quad (6.2)$$

where *N* is the effective stress ratio at the failure, $(1-\sin\varphi')/(1+\sin\varphi')$; *n* is the strain ratio after the peak, $(1-\sin\psi)/(1+\sin\psi)$.

φ' and ψ are friction angle and dilation angle respectively and they can be determined by the equations of

$$\begin{aligned}\sin\varphi' &= s/[1+(s-1)\sin\varphi'_{cv}] \\ \sin\psi &= s+(s-1)\sin\varphi'_{cv}\end{aligned} \tag{6.3}$$

s is the gradient of effective expansion pressure plotted against cavity strain on log scales, for example in Figure 6-5. Once obtained, the best fitting curve can be constructed by choosing appropriate values for φ_{cv}, σ'_{h0} and *G*. Despite the absence of the apparent cohesion terms in Eqn(6.2), the curvature of curve fit plot indicates the behavior of strain softening which has been taken into account in the analytical solution. Thus, the property of cohesive frictional materials can be reliably interpreted by Hughes' method.

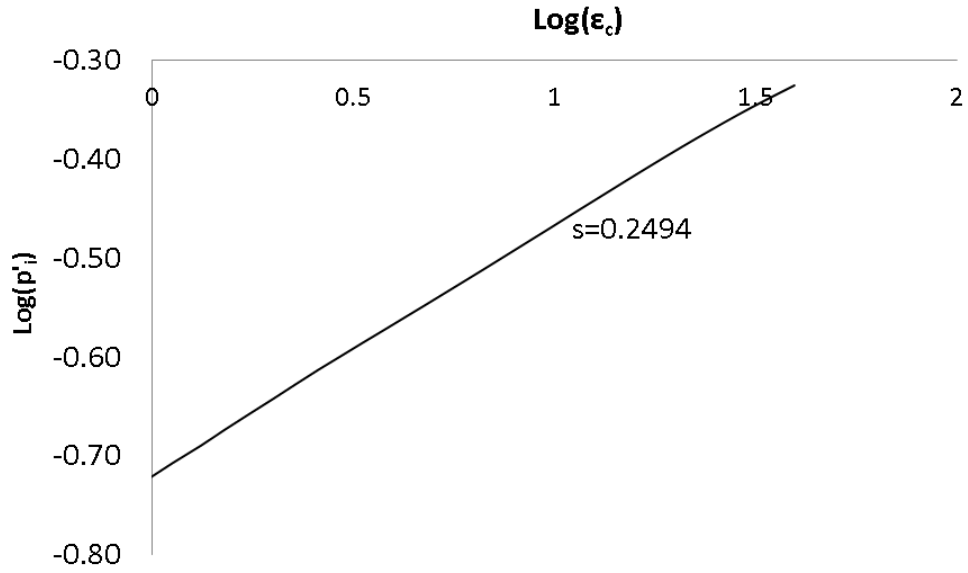

Figure 6-5. The example plot of expansion curve in log scales

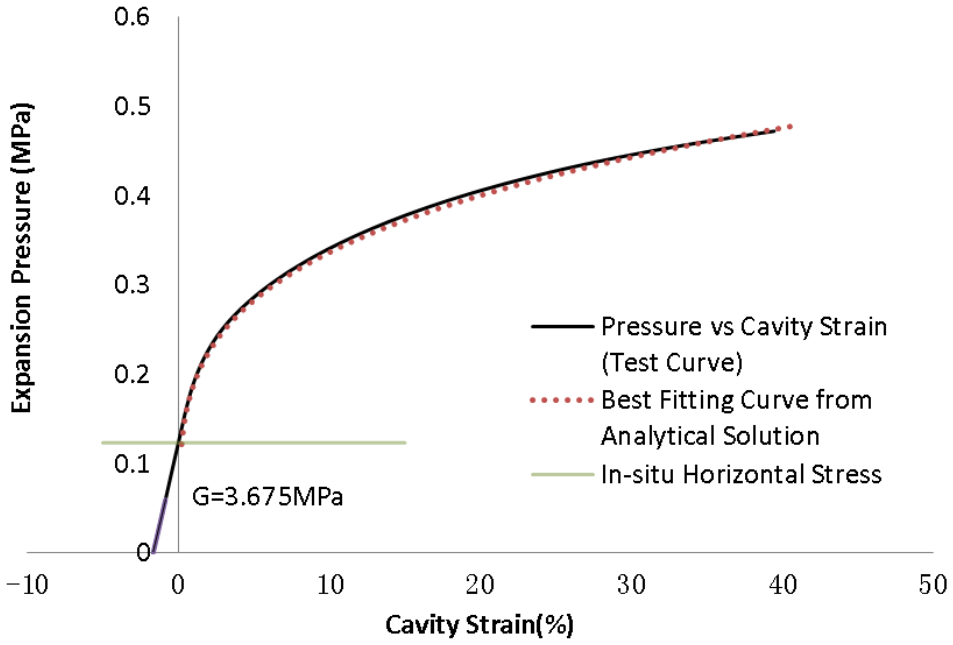

Figure 6-6. The best fitting curve plotted based on the Eqn(6.2) for an example drained expansion. φ_{cv} = 25.3° and σ'_{h0}=0.12MPa

It should be noted that the interpretation performed above is for the case of uniform expansion. Hughes' method was also applied to the averaged drained expansion curves obtained from the modelled tests under anisotropic horizontal stresses. Keeping φ_{cv} and G constant, we adjusted the values of σ'_{h0} until the best fitting curve matches the target expansion curve. It is found that the interpreted σ'_{h0} significantly deviates from the true horizontal stresses, even at low horizontal anisotropy (Figure 6-7). Eqn (6.2) also shows the high sensitivity of σ'_{h0} over the expansion curves. Thus if in-situ horizontal stress is wrongly estimated, Hughes' method will also lead to the unrealistic interpretation of other parameters.

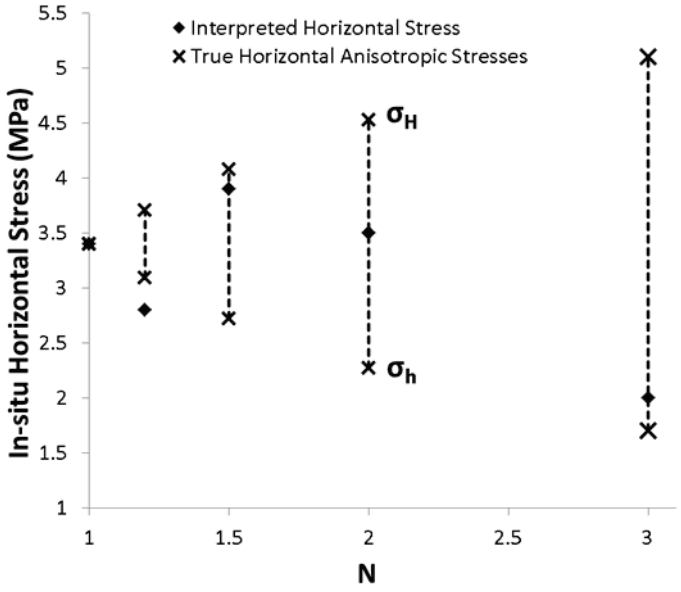

Figure 6-7. The error caused by using Hughes' method for drained case to interpret initial horizontal stress. Assume that the other parameters (φ_{cv} and G) are correctly estimated.

The study above discusses the sensitivity of the in-situ stress anisotropy to the interpretation based on the methods developed for both sand and clay under given testing condition. For the case of undrained expansion, Gibson & Anderson method gave a reasonable interpretation of in-situ stress and undrained shear strength of soil while Hughes' method may lead to the erroneous estimation of the in-situ properties and conditions of soils when the anisotropic stresses are present. In practice, the accuracy of the interpretation might be also affected by the actual pore water drainage, inherent fabric anisotropy and heterogeneity, reliability of testing facility and proficiency of interpreter. A comprehensive framework should be established to assess the results with rational explanations.

6.2 Advanced Interpretation Method for Reservoir Geomechanical Pressuremeter Testing

6.2.1 Reservoir Geomechanical Pressuremeter

Reservoir geomechanical pressuremeter is a pre-bored pressuremeter which is designed to pressurize the borehole at a considerable depth. It is still under the

development by reservoir geomechanics research group of University of Alberta. It is conceived as an upgrade of the old model of HPD (high pressure dilatometer) assembled with more detecting elements such as pore pressure gauges, multiple caliper arms both located at inside and outside of probe and a wireline locking and pumping compartment (Figure 6-8).

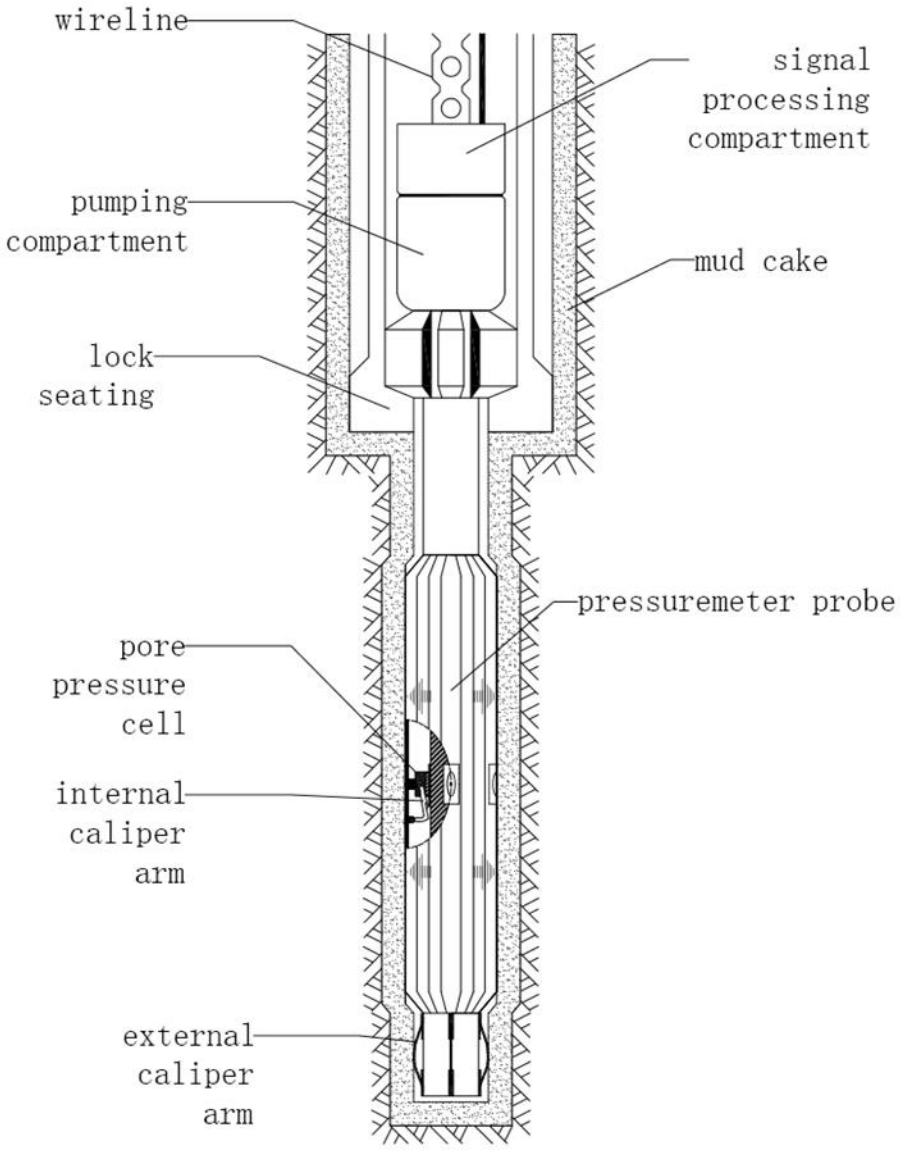

Figure 6-8. The tentative design of reservoir geomechanical pressuremeter

The pocket drilling should be carefully done to ensure that the cavity is in the correct size and shape. A fat pocket may not enable the lock seating to be placed at a stable and even position, while a slim pocket may need a hard insertion of probe which leads to the disturbance to the cavity periphery. An assessment of pocket condition is necessary before the tool installation. The effective drilling mud should be able to resist the infiltration of the formation fluid into the borehole without augmenting the cavity radius. The quality of testing will be significantly affected if the internal boundary seepage is allowed.

6.2.2 Operation and Interpretation

The instrumentation of reservoir geomechanical pressuremeter follows a similar concept of the traditional pre-bored pressuremeter except the pore pressure is specially monitored. Figure 6-9 demonstrates how the pressuremeter works in a particular kind of formation associated with the predicted ground pore pressure profile responding to the expansion of cavity.

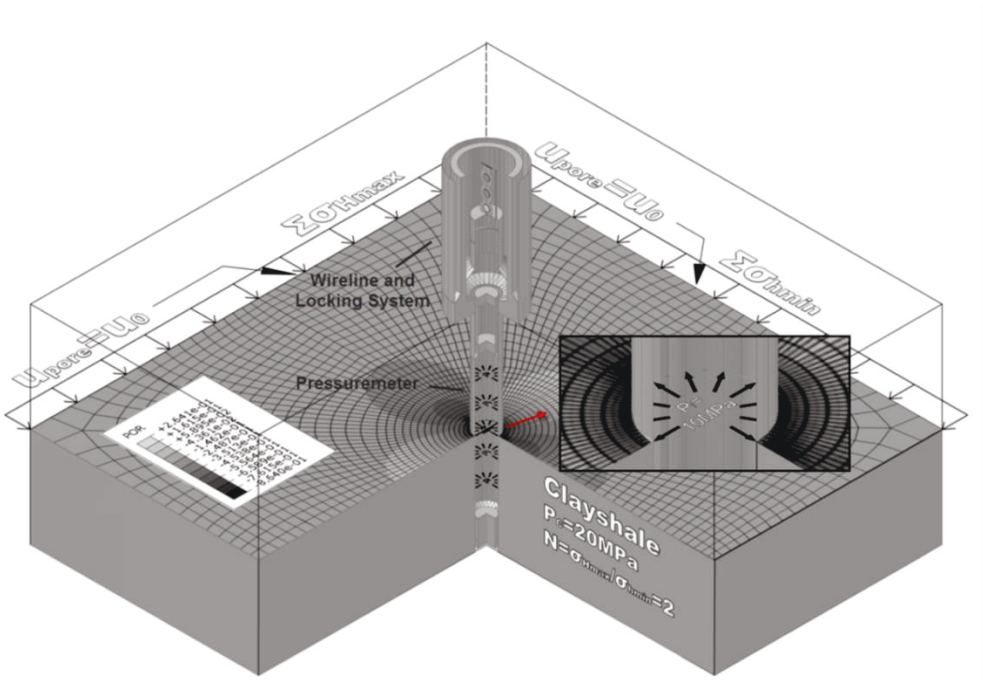

Figure 6-9. The illustration of reservoir geomechanical pressuremeter testing and the corresponding ground responses

A straightforward way to execute the interpretation is to do data matching using optimization techniques. Specifically, if a set of initial *P* is given, the response *R* can be computed by one cycle of simulation,

$$R = F(\mathrm{P}) \tag{6.4}$$

where F is the unknown relationship between *P* and *R*. After a number of computations with the improving input of *P* are iterated, the minimal difference between the measured values and the predicted values can be achieved at the end of step *n,* which are mathematically expressed as,

$$D_n(\mathrm{P}) = \frac{1}{S_x}\sum_{i}^{S_x}\left[\left(R^m - R_n^p\right)^T W_x \left(R^m - R_n^p\right)\right] \tag{6.5}$$

where S_X is the number of steps when the measurement is conducted, e.g., S_X=3 if data matching is performed in three separate steps of borehole relaxation, packer expansion and packer contraction; W_X is a weighting matrix; R^m is the measured response and R^p is the predicted response.

The convergence of the approximation does not only require an adequate adaptive algorithm but, most importantly, a good initialization of input values. There are three suggested approaches mentioned in the previous chapters that can do an effective estimation of parameters including *N, k,* $p'_{C,}$ and σ'_h. The procedure is elaborated in steps shown in Figure 6-10. Since the basis of interpretation is a pool of numerical results from stages of simulation, the accuracy of the computation is extremely important. This thesis provides the validation of the numerical accuracy against the analytical solution in Chapter 2 and the predicted cavity responses under varying conditions have been reasonably explained in the following chapters. Thus, the established method is able to make an acceptable estimation over the field data.

The interpretation in each step is mutually dependent of the results from other steps. For example, in order to estimate *N* value by convergence rate from Figure

3-21, G_0 and k are required to calculate the coefficient D. Likewise, the dimensionless parameter $\widehat{p_i}|_{\Delta u=max}$ can only be determined when the magnitudes of σ'_h and σ'_H are given. However, we are not completely blind to the underground condition. If the prior information of geomechanical properties exists or any additional string tools can provide independent measurement of one of the properties, the interpretation will become much easier and less ambiguous. It should be also noticed that the stress anisotropy N can be estimated by two different approaches. The interpretation can be still reliable if one of the approaches fails.

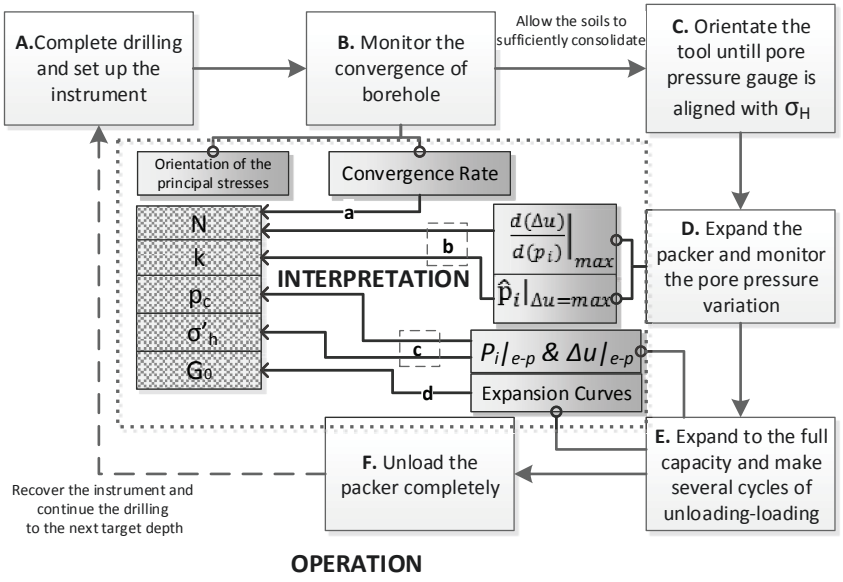

Figure 6-10. The flow diagram of the in-situ testing and interpretation of reservoir geomechanical pressuremeter

7 Conclusions and Recommendations

7.1 Summary

This research had two primary objectives – (1) to investigate the borehole response during the cavity expansion in the poorly or moderately consolidated formation under different horizontal stress anisotropies and (2) to develop the interpretation methodology to invert this anisotropy and other in-situ parameters from the downhole pressuremeter testing in soft rock.

The drainage condition was classified over the factors of loading rate and medium permeability by evaluating both the excess pore pressure generation and void ratio variation. The response to the expansion in the porous mediums which have been disturbed by pocket boring was distinguished from that in the intact or unyielded materials in Chapter 2.

In Chapter 3, the possible stress regimes for the deep bedding formations were concluded based on the yielding criterion of Cam Clay model. The short term and long term borehole deformation and damages induced by drilling were both investigated. The time-dependent convergences were correlated with the initial horizontal stress anisotropies, which makes the inversion possible by matching the convergence rate in the chart of characteristic curve.

In Chapter 4, the converged borehole geometry was treated as initial internal boundary for the cavity expansion. The influences of initial stress anisotropy and drilling-induced modulus heterogeneity on the resultant stress profile after expansion were discussed. The possible shear failure regions under different loading regimes were compared. It is necessary to extend the study into the relatively high permeability formation which exhibits the behavior of partial drainage to the outer boundary. The variation trend of excess pore pressure under such an environment was analyzed.

An overall simulation incorporating the real properties of instrument and in-situ materials were conducted in Chapter 5. The packer membrane was calibrated first and its constitutive parameters were obtained as the input for the FEM model. An entire cycle of loading and unloading was tracked under varying stress anisotropies. Chapter 5 also provides an insight into the pore pressure response at borehole surface which differs over the in-situ stresses and stiffness of the mediums. Two indices - critical expansion pressure and critical excess pore pressure were introduced to interpret the preconsolidation pressure and in-situ horizontal stress anisotropy.

Two traditional interpretation methods are performed on the synthetic data obtained from the modelled pressuremeter testing under non-hydrostatic boundary loadings. The interpreted error was found in comparison with the true values. A new interpretation method was suggested for the RGP testing.

7.2 Conclusions

A reliable assessment of values from pressuremeter test in stiff clays or weak rock is always challenging. The perplexing response captured by the strain arms are mainly attributed to three reasons: (1) the soil sensitivity to the drilling disturbance; (2) the uncertainty of drainage conditions; (3) the horizontal stress anisotropy. A systematic evaluation of these three factors was carried out based on a stress-fluid coupled FEM model in this work.

The finding from Chapter 2 shows that the cavity expansion in most soft sedimentary formations is partially drained and the in-situ permeability is minimally affected. Plastic deformation initiated by drilling and further developed in the relaxation stage can soften the materials and thus lead to a remarkable rise for both pore pressure and radial displacement if the borehole is subsequently expanded.

Geostatic stress in the sedimentary bedding is constrained by Cam Clay yield surface. Accordingly, the reasonable range of stress anisotropies including parameters $\overline{K}$ and *N* could be narrowed down for a given depth. The time dependent convergence takes place until all the excess pore pressure dissipates. The amount of convergence as a result of the consolidation depends on the ratio of maximum in-plane stress to the minimal in-plane stress, i.e., the value of *N*. Reversely, *N* can be reflected by the radial displacement monitored by the strain arms at different angles. To avoid the error from the estimation of the reference borehole radius, the convergence rate rather than the absolute value of convergence was suggested for the interpretation purpose.

Since drilling in the anisotropic stress field leads to the stress redistribution in the borehole annulus, the expansion behavior should be independently examined at each azimuth. It was found that the shear modulus was significantly mobilized in the near borehole regions, resulting in different pore pressure response from that in the intact medium. The mobilized shear moduli also caused much more expansion at orientation of maximum horizontal stress than that of minimum horizontal stress, which is more evident in the high stress anisotropy. The plastic zone tends to develop parallel to the major horizontal stress while in the trend of forming a butterfly shape when the *N* goes higher than 3.

While the stress anisotropy *N* governs the maximum excess pore pressure generation rate, permeability *k* determines the maximum excess pore pressure that the expansion will generate. It is thus useful to estimate the in-situ horizontal permeability by reading the maximum absolute value in the recorded pore pressure curves. Even though the interpretation is guided by the numerical results that might be dependent of the constitutive model being used, it provides an efficient and economical way to evaluate the permeability without additional independent pore pressure measurement.

A simple approach to calibrate the mechanical properties of membrane was introduced and the results were proven by the numerical validation. The simulation of full expansion-contraction cycle showed that the interpretation based on the instrument readings would underestimate the shear modulus. The critical excess pore pressure at the azimuth of σ_H is highly dependent of the initial stress anisotropy while the corresponding critical expansion pressure is determined by the isotropic preconsolidation pressure p'_c.

The traditional techniques (Gibson & Anderson Method and Hughes' method) to interpret the pre-bored pressuremeter test appeared to be valid and efficient in the isotropic stress condition. However, they failed to provide an acceptable interpretation for non-uniform expansion, even under low stress anisotropy. The proposed downhole testing aims at inverting the in-situ properties, including maximum and minimal horizontal stresses σ_H and σ_h, isotropic preconsolidation pressure p'_c, horizontal permeability k, and shear modulus G_0, from the observed ground response to the instrumenting at three independent stages. The entire measurement consists of borehole convergence after the instance of drilling, the pore pressure variation during the packer expansion and the full expansion to the tool capacity. The entire testing procedure that incorporates the techniques demonstrated in the separate chapters was given in Figure 6-10.

7.3 Recommendations for Future Studies

7.3.1 Physical Model of Reservoir Geomechanical Pressuremeter

Figure 6-8 presents the preliminary design of reservoir geomechanical pressuremeter. However, the practical issue that a design engineer needs to face is how to place the pore pressure gauges into the formations.

The pore pressure measurement has already been provided with lots of in-situ testing tools including piezometer and cone penetrometer. The piezo-element can efficiently reflect the pore water response in a dynamic testing environment.

Wroth (1980) introduced the pore pressure monitoring techniques accompanied with the self-boring pressuremeter testing by a specially developed instrument (Cambridge Pressuremeter Probe). It simply works with a miniature pore pressure diaphragm fixed to the membrane. The ambient pore pressure is obtained when the tool is at rest and the excess pore pressure can be captured when the probe inflates to a certain level (Figure 7-1).

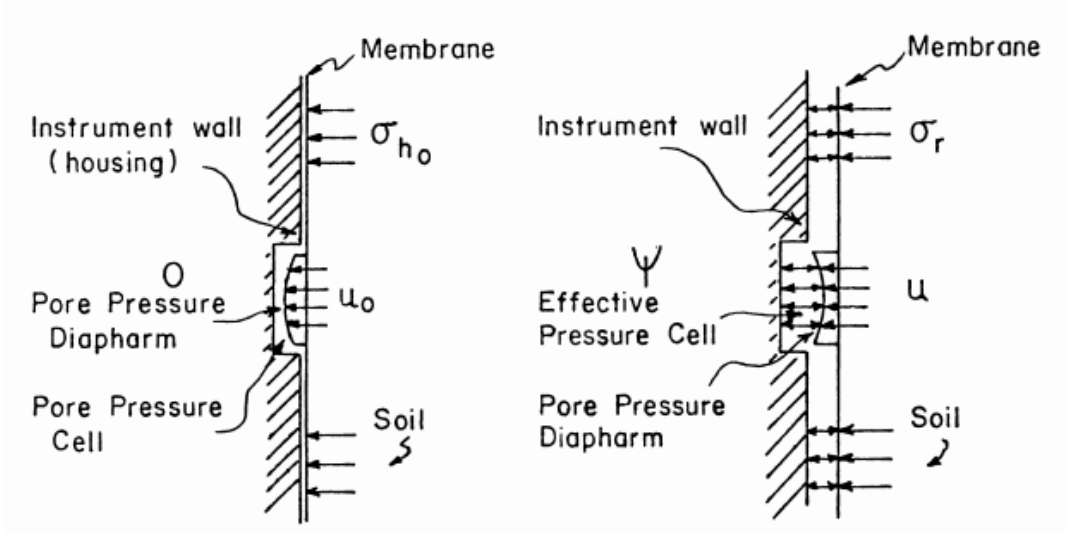

Before start of expansion test During test

Figure 7-1. The schematic diagram of cambrdige pressuremeter probe (Wroth, 1984)

However, in the deep borehole application, the true response of pore pressure at borehole surface is masked by the mud cake thickness. A pore pressure sensor that can penetrate into the mud layer is expected to be developed.

7.3.2 Laboratorial Validation of Numerical Results

Although the FEM model has been benchmarked with the analytical solutions at the beginning of this thesis, it still requires the experiment to validate the numerical results for a this type of materials. The verification could be done by carrying out the laboratorial test both directly and indirectly.

The direct way to simulate the downhole test is to establish a physical model at the laboratorial scale. A downsized pressuremeter (Pressio-Triax) were developed and used to investigate cavity expansion in a soil specimen under isotropic stress (Rangeard et al., 2003). The same setup could be configured in the true triaxial loading frames for expansion test under non-uniform boundary pressure.

Alternatively, the stress/strain path observed in the real pressuremeter test could be reproduced on a small soil specimen by manipulating the boundary loadings. True triaxial test has been applied to simulate the loading conditions of borehole elements under uniform expansion (Wood and Wroth, 1977). However, the major difference between the expansions under hydrostatic loading and non-hydrostatic loadings is the repeatability of stress path, such that, in the latter case, the stress path differs at every single location around the borehole. Thus, the response of each element needs to be individually evaluated. Furthermore, the fact that total radial and tangential stresses are not changing at equal rate also makes it extremely hard to accurately control the tests. Thus, by few means, the conventional geotechnical laboratorial setup is able to simulate the expansion in the anisotropic stress field.

7.3.3 Field Validation of Proposed Method with a Range of Relevant Materials

In the absence of the physical model of reservoir geomechanical pressuremeter, the existing tool, such as high pressure dilatometer, can be initially employed for the deep borehole test and its multi-axis measurements of borehole deformation could be used for stress anisotropy evaluation.

It should be noted that the vertical stress anisotropy or earth pressure coefficient K_0 is also high at shallow ground. Thus, the test environment may not necessary be the deep downhole. Either a perpendicular borehole into the vertical cut or a parallel borehole to the bedding plane from inside of tunnel can

provide realistic response of interest. One should be careful of the drainage boundary in such environments since the pore water pressure may be hydrostatically profiled in the test plane and no mudcake is built to impede the water influx. In this case, the model needs to be reestablished with appropriate boundary conditions.

In order to better evaluate the proposed method, the prior information of the test materials is desirable. Many highly developed downhole tools can provide useful assessment of formation properties without damaging the borehole. For example, in-situ permeability can be obtained by implementing packer test; sonic scanner is efficient to the capture anisotropic shear moduli and the in-situ stresses are also accessible if load cell pressuremeter is applicable to the given conditions (Carder and Bush, 2001). However, the testing time and expense should be considered.

One of the advantages of pre-boring is that the recovered core of soil/rock is available for the laboratory testing. This, on the one hand, provides the mechanical properties of material for the pressuremeter interpretation; on the other hand, the properties interpreted by the pressuremeter testing itself can be cross validated with the laboratorial test results.

Since this simulation work is based on a specific constitutive model, it might give an erroneous interpretation if the other classes of materials (brittle or pure frictional materials) are tested. However, core testing allows a complete characterization of the constitutive behaviors of materials of interest, by which an appropriate model to be employed in the numerical analysis can be found and calibrated. The procedure proposed for this thesis can be reproduced with the simulation using different constitutive models.

7.3.4 Further Consideration for the Modelling Work

To make a prediction in a more realistic sense, some assumptions given in this thesis needs to be removed in the future development of the numerical model. The further research is suggested to study the sensitivities of following factors.

1. Inner Boundary Drainage. Pore pressure variations are the main potential logging parameters considered in this research. In simplifying the modelling approach, an in-balanced mud cake and completely impermeable boundary were assumed. Practically, the mud pressure is unlikely to be perfectly controlled, and the pressure acting on the inner boundary is the net pressure subtracted from the expansion pressure by possible unbalanced pressure between mud cake and formations. Also, the loss of pore water is possible if filter exists. As a result, the pore pressure change would be less evident which leads to inaccurate prediction. A comprehensive evaluation model is thus recommended reduce such errors.

2. Finite Tool Length. The cylindrical cavity expansion theory has been widely applied to the analysis of pressuremeter testing. It neglects the tool geometry as characterized by the ratio of its length to diameter. The biased estimation of material properties has been examined by Houlsby and Carter (1993) and discussed by Jefferies (1995), both showing that the undrained shear strength would be overestimated if one fails to consider the finite length. The restraint imposed at the ends of the membrane leads to a curved expansion profile along the instrument axis. Thus, the actual response for a short pressuremeter expansion falls in between the rigorously derived solutions for cylindrical and spherical expansions. A three-dimension model is required to take into account the unbalanced deformation both horizontally and vertically.

3. Arbitrarily Oriented In-situ Stresses. The in-situ principal stresses direction may not be aligned with the cross-sectional plane of boreholes. This happens primarily because many wells being drilled are highly deviated or have

complicated trajectories. In this case the stress tensor needs to be defined in two coordinate systems: (1) the coordinate for the in-situ stresses (2) the coordinate in compliance with wellbore trajectory. Thus, three principal stresses actually acts in directions out of plane of local wellbore coordinate. By performing coordinate transformation on stress tensors and applying Airy stress functions, the drilling-induced stresses and deformation can be solved explicitly (ONG, 1994). The numerical capability to calculate the drilling-induced stresses in the transversely anisotropic mediums have also been proven valid for varying borehole inclinations (Karpfinger and Prioul, 2011). However, the relation between cavity expansion and the in-situ stresses becomes more sophisticated and unpredictable when two more geometrical variables (wellbore azimuth and inclination) are introduced into the computation.

4. Inherent Anisotropy and Heterogeneity

The inherent anisotropy can be expected from the structural arbitrary. Not only one type of materials will be encountered in the wellbore vicinity during cavity expansion. The bedding planes are usually dipping from the horizon due to mechanisms of folding and faulting in sedimentary strata. The general configuration of formations with respect to the location of the vertical wellbore is illustrated in Figure 7-2. The borehole response is related to the constitutive properties at both in-plane and out-of-plane orientations. The conventional method to identify the structural anisotropies is by applying sonic logging combined with geometrical manipulations on a three-dimensional model (Zoback, 2010).

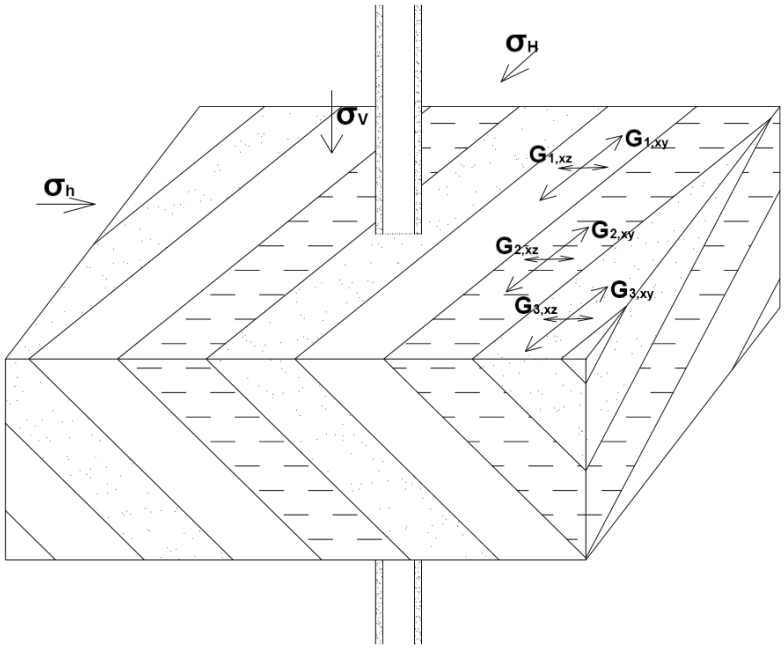

Figure 7-2. The example of vertical borehole oblique to the heterogeneous medium with traverse structural anisotropies. The subscripting for shear modulus *G* follows the rule that the *xy* is parallel to the bedding plane while *xz* is perpendicularto the bedding plane

It is not easy to single out the influence that each bedding plane has on the wellbore deformation induced by drilling and subsequent expansion, even if the local geology is well profiled. In order to history match the expansion and hence constrain the stress anisotropy in such cases, a probabilistic model incorporating the acquirable geological information at depth of interest is required.

5. Decementation of Shaly Materials

Different degrees of cementation have been found for various cohesive materials especially at great depth where the digenetic processes are significant (Bjørlykke and Høeg, 1997). Cementation affects the mechanical properties of soils including initial stiffness and shear strength. Under the theoretical frame of soil mechanics, the remarkable difference between the uncemented and cemented materials is revealed from the *e-p* plot where the apparent preconsolidation

pressure is higher than the maximum past effective vertical stress (Bjerrum and Wu, 1960). The contribution of cementation to the mechanical strength has been quantitatively tested and discussed (Lambe, 1960), but few models could accurately capture the behaviors of cemented materials under varying loading conditions.

The bonded Cam Clay Model was developed to describe the decementation behavior of structured soils by introducing two parameters of initial bonding and debonding rate (Yu, 1998). The theorem has been adopted by Gonzalez et al.(2009) who discovered the similar pattern of the resultant pressuremeter loading curves in the bonded soils as compared to the overconsolidated soils. Unloading and strain holding is capable of distinguishing their effects. Since the materials will undergo repeated cycle of loading and unloading in the operational steps proposed for a single test in this thesis, it is necessary to take into account the decementation effect in the modelling for the future work.

6. Fracturing

Tensile fracturing is likely to occur under high stress anisotropy. Cavity expansion is possible to initiate the fracture, particularly at the azimuth of maximum horizontal stress as concluded in Chapter 4. Haberfield and Johnston (1990) characterized the cracking mechanism of expanding cavity in soft rock by predefining the weak elements in FEM modelling . The finding showed that the radial displacement and expansion pressure at shearing failure would be underestimated if the tensile cracks are observed at borehole surface. In the case of the anisotropic boundary stress condition, there is no need to specify the weak zones, but in order to predict the possible fracturing path, discrete element modelling may be required.

References

Abousleiman, Y.N., Chen, S.L., 2012. Exact undrained elasto-plastic solution for cylindrical cavity expansion in modified Cam Clay soil. Géotechnique 62, 447–456.

Alberta Energy Regulator, 2014. AER Bulletin 2014-03.

Ask, D., 2006. New developments in the Integrated Stress Determination Method and their application to rock stress data at the Aspo HRL, Sweden. International Journal of Rock Mechanics and Mining Sciences 43, 107–126.

Bjerrum, L., Wu, T., 1960. Fundamental shear-strength properties of the Lilla Edet clay. Geotechnique 10, 101–109.

Bjørlykke, K., Høeg, K., 1997. Effects of burial diagenesis on stresses, compaction and fluid flow in sedimentary basins. Marine and Petroleum Geology 14, 267–276.

Bolton, M., Whittle, R., 1999. A non-linear elastic/perfectly plastic analysis for plane strain undrained expansion tests. Geotechnique 49, 133–141.

Brown, E., Hoek, E., 1978. Trends in relationships between measured in-situ stresses and depth. International Journal of Rock Mechanics and Mining Sciences 15, 211–215.

Brucy, F., Letirant, P., 1986. Use of PAM and pressuremeters in offshore foundation design, in: J-L, B., JME, A. (Eds.), The Pressuremeter and Its Marine Applications: Second International Symposium. ASTM 950, Paris.

Cade, C., Evans, I., Bryant, S., 1994. Analysis of permeability controls: a new approach. Clay Minerals 29, 491–501.

Cambridge Insitu Ltd, n.d. An introduction to pressuremeters [WWW Document]. URL: http://www.cambridge-insitu.com/products/pressuremeters/introduction-pressuremeters

Cao, L., Teh, C., Chang, M., 2001. Undrained cavity expansion in modified Cam clay I: Theoretical analysis. Geotechnique 51, 323–334.

Cao, S., Glezen, W., Lerche, I., 1986. Fluid Flow, Hydrocarbon Generation, And Migration: A Quantitative Model Of Dynamical Evolution In Sedimentary Basins, in: Offshore Technology Conference. Houston, TX, pp. 267–272.

Carder, D., Bush, D., 2001. Development and testing of load cell pressuremeter. Proceedings of the Institution of Civil Engineers 149, 141–142.

Carter, J., Booker, J., Yeung, S., 1986. Cavity expansion in cohesive frictional soils. Geotechnique 2, 349–358.

Carter, J., Randolph, M., Wroth, C., 1979. Stress and pore pressure changes in clay during and after the expansion of a cylindrical cavity. International Journal for … 3, 305–322.

Carter, J.P., 1982. Elastic consolidation around a deep circular tunnel. International Journal of Solids and Structures 18, 1059 – 1074.

Chang, M., Teh, C., Cao, L., 2001. Undrained cavity expansion in modified Cam clay II : Application to the interpretation of the piezocone test. Geotechnique 51, 335–350.

Collins, I., Stimpson, J., 1994. Similarity solutions for drained a undrained cavity expansions in soils. Geotechnique 44, 21–34.

Collins, I., Yu, H., 1996. Undrained cavity expansions in critical state soils. International Journal for Numerical and Analytical Methods in Geomechanics 20, 489–516.

Collins, P., 2007. Geomechanical effects on the SAGD process. SPE Reservoir Evaluation & Engineering 10, 1–3.

Detournay, E., Cheng, A., 1988. Poroelastic response of a borehole in a non-hydrostatic stress field. International Journal of Rock Mechanics and Mining Sciences 25, 171–182.

Detournay, E., St. John, C.M., 1988. Design charts for a deep circular tunnel

under non-uniform loading. Rock Mechanics and Rock Engineering 21, 119–137.

Dutta, N., 1987. Fluid flow in low permeable porous media: in Migration of hydrocarbons in sedimentary basins. Editions Technip, Paris.

ERCB, 2010. Total E&P Canada Ltd. - Surface Steam Release of May 18, 2006 Joslyn Creek SAGD Thermal Operation.

Failmezger, R.A., Zdinak, A.L., Darden, N., J., Fahs, R., 2005. Use of Rock Pressuremeter for Deep Foundation Design. insitusoil.com 1–10.

Ferreira, R., 1993. Interpretation of pressuremeter tests using a curve fitting technique. University of Alberta.

Fragaszy, R., Cheney, J., 1977. Influence of Borehole Imperfections on Pressuremeter. Journal of the Geotechnical Engineering Division 103, 1009–1013.

Gibson, R.., Anderson, W.F., 1961. In situ measurement of soil properties with the pressuremeter. Civil Engineering Public Works Review 56, 615–618.

Gonzalez, N.A., Arroyo, M., Gens, A., 2009. Identification of bonded clay parameters in SBPM tests: A numerical study. Soils and foundations 49, 329–340.

Goodman, R.E., 1989. Introduction to rock mechanics, Second. ed. Wiley, New York.

Gutierrez, M., Nygård, R., Høeg, K., Berre, T., 2008. Normalized undrained shear strength of clay shales. Engineering Geology 99, 31–39.

Haberfield, C., Johnson, I., 1990. A numerical model for pressuremeter testing in soft rock. Geotechnique 40, 569–580.

Hamilton, W., Babet, P., 1975. Alberta Clays and Shales: Summary of Ceramic Properties. Edmonton, Canada.

Haug, K., Greene, P., Schneider, C., Mei, S., 2013. Geological and Geomechanical

Characterization of In situ Oil Sands Caprock in the Athabasca Oil Sands Area Alberta Canada. 47th US Rock Mechanics/Geomechanics Symposium.

Hawkins, P., Whittle, R., 1999. Using a self boring expansion pressuremeter to measure the permeability of soils. Little Eversden, Cambridge, UK.

Hill, R., Peterson, R., 1994. Techniques for determining subsurface stress direction and assessing hydraulic fracture azimuth, in: SPE Eastern Regional Meeting. Charleston, WV, pp. 305–320.

Houlsby, G., Carter, J., 1993. The effects of pressuremeter geometry on the results of tests in clay. Geotechnique 29, 845–859.

Houlsby, G., Withers, N., 1988. Analysis of the cone pressuremeter test in clay. Geotechnique 38, 575–587.

Huang, A., Fang, C., Liao, J., Pan, Y., 2002. Development of a multiple-purpose Borehole Testing Device for soft rock. ASTM geotechnical testing journal 25, 1–7.

Huang, A., Pan, I., Liao, J., 1999. Pressuremeter tests in poorly cemented weak rocks, in: The 37th U.S. Symposium on Rock Mechanics. Vail, CO, pp. 247–252.

Hughes, J., Jefferies, M., Morris, D., 1984. Self-bored pressuremeter testing in the Arctic offshore, in: Offshore Technology Conference. Houston, Texas, pp. 255–261.

Hughes, J., Wroth, C., Windle, D., 1977. Pressuremeter tests in sands. Geotechnique 27, 455–477.

Jefferies, M., 1995. Discussion: The effects of pressuremeter geometry on the results of tests in clay. Geotechnique 45, 741–748.

Jefferies, M., 1988. Determination of horizontal geostatic stress in clay with self-bored pressuremeter. Canadian Geotechnical Journal 26, 760–763.

Karpfinger, F., Prioul, R., 2011. Revisiting borehole stresses in anisotropic elastic media: comparison of analytical versus numerical solutions, in: 45th U.S.

Rock Mechanics / Geomechanics Symposium. San Francisco, CA, pp. 273–282.

Kirsch, G., 1898. Die theorie der elastizitat und die bedurfnisse der festigkeitslehre. Zeitschrift der Vereins deutscher Ingenieure 42, 797–807.

Kwon, O., 2004. Permeability of illite-bearing shale: 1. Anisotropy and effects of clay content and loading. Journal of Geophysical Research 109, B10205.

Ladanyi, B., 1972. In-situ determination of undrained stress-strain behavior of sensitive clays with the pressuremeter. Canadian Geotechnical Journal 9, 313–319.

Lambe, T.W., 1960. A Mechanistic Picture of Shear Strength in Clay, in: Research Conference on Shear Strength of Cohesive Soils. New York, pp. 555–580.

Ledesma, A., Gens, A., Alonso, E.E., 1996. Parameter and variance estimation in geotechnical backanalysis using prior information. International Journal for Numerical and Analytical Methods in Geomechanics 20, 119–141.

Leeman, E., 1971. The CSIR “doorstopper” and triaxial rock stress measuring instruments. Rock Mechanics and Rock Engineering 50, 25–50.

Lin, W., Kwaśniewski, M., Imamura, T., Matsuki, K., 2006. Determination of three-dimensional in situ stresses from anelastic strain recovery measurement of cores at great depth. Tectonophysics 426, 221–238.

Liu, L., Chalaturnyk, R., Zambrano, G., n.d. Numerical Investigation and Identification of Geomechanical Parameters from Self - bored Pressuremeter Testing. In Preparation.

Ljunggren, C., Chang, Y., Janson, T., Christiansson, R., 2003. An overview of rock stress measurement methods. International Journal of Rock Mechanics and Mining Sciences 40, 975–989.

Mair, R.J., Wood, D.M., 1987. Pressuremeter testing, CIRIA Ground Engineering Report: In-situ testing. CIRIA and Butterworths, Sevenoaks, UK.

Martin, C., 1996. The role of convergence measurements in characterizing a rock

mass. Canadian geotechnical journal 33, 363–370.

Mckinnon, S.D., 2001. Analysis of stress measurements using a numerical model methodology. International Journal of Rock Mechanics & Mining Sciences 38, 699–709.

Moos, D., Zoback, M.D., 1990. Utilization of observations of well bore failure to constrain the orientation and magnitude of crustal stresses: Application to continental, Deep Sea Drilling Project, and Ocean Drilling Program boreholes. Journal of Geophysical Research 95, 9305.

Neuzil, C., 1994. How permeable are clays and shales? Water Resources Research 30, 145–150.

Ogden, R.W., Roxburgh, D.G., 1999. A pseudo-elastic model for the Mullins effect in filled rubber. Proceedings of the Royal Society A: Mathematical, Physical and Engineering Sciences 455, 2861–2877.

ONG, S.H., 1994. Borehole Stability. Univeristy of Oklahoma.

Palmer, A.C., 1972. Undrained plane-strain expansion of a cylindrical cavity in clay: a simple interpretation of the pressuremeter test. Géotechnique 22, 451–457.

Prevost, J.-H., Hoeg, K., 1975. Effective stress-strain-strength model for soil). Journal of Geotechnical and Geoenvironmental Engineering 101, 259–278.

Randolph, M., Carter, J., Wroth, C., 1979. Driven piles in clay—the effects of installation and subsequent consolidation. Geotechnique 29, 361–393.

Randolph, M.F., Wroth, C.P., 1979. An analytical solution for the consolidatin around a driven pile. International journal for numerical and analytical methods in geomechanics 3, 217–229.

Rangeard, D., Y. Hicher, P., Zentar, R., 2003. Determining soil permeability from pressuremeter tests. International Journal for Numerical and Analytical Methods in Geomechanics 27, 1–24.

Ratnam, S., Soga, K., Whittle, R., 2005. A field permeability measurement

technique using a conventional self-boring pressuremeter. Géotechnique 55, 527–537.

Reed, M.B., 1988. The influence o f out-of-plane stress on a plane strain problems in rock mechanics. International Journal for Numerical and Analytical Methods in Geomechanics 12, 173–181.

Rice, J., Cleary, M., 1976. Some basic stress diffusion solutions for fluid-saturated elastic porous media with compressible constituents. Reviews of Geophysics 14, 227–241.

Roscoe, K.H., Burland, J.B., 1968. On the generalised stress-strain behaviour of wet" clay, in: Engineering Pasticity. Cambridge University Press, Cambridge, UK, pp. 535–609.

Samarasinghe, A.M., Huang, Y.H., Drnevich, V.P., 1982. Permeability and consolidation of normally consolidated soils. Journal of the Geotechnical Engineering Division 108, 835–850.

Schmitt, D.R., Currie, C. a., Zhang, L., 2012. Crustal stress determination from boreholes and rock cores: Fundamental principles. Tectonophysics 580, 1–26.

Schulze-Makuch, D., Carlson, D.A., Cherkauer, D.S., Malik, P., 1999. Scale dependency of hydraulic conductivity in heterogeneous media. Groundwater 37, 904–919.

Schutjens, P., Hanssen, T., 2004. Compaction-induced porosity/permeability reduction in sandstone reservoirs: Data and model for elasticity-dominated deformation. SPE Reservoir Evaluation & Engineering 7, 202–216.

ShafieZadeh, N., Chalaturnyk, and R., 2014. Interpretation Challenges for In Situ Stress from Mini-Frac Tests in Soft Rocks/Hard Soils, in: Shale Energy Engineering. pp. 298–309.

Sheng, D., Sloan, S.W., Yu, H.S., 2000. Aspects of finite element implementation of critical state models. Computational Mechanics 26, 185–196.

Silvestri, V., 2004. Disturbance effects in pressuremeter tests in clay. Canadian

geotechnical journal 126, 738–759.

Skempton, a. W., 1954. The Pore-Pressure Coefficients A and B. Géotechnique 4, 143–147.

Steiger, R., Leung, P., 1991. Critical state shale mechanics, in: The 32nd US Symposium on Rock Mechanics. Norman, OK, pp. 293–302.

Sun, D., Lin, W., Cui, J., Wang, H., Chen, Q., Ma, Y., Wang, L., 2014. Three-dimensional in situ stress determination by anelastic strain recovery and its application at the Wenchuan Earthquake Fault Scientific Drilling Hole-1 (WFSD-1). Science China Earth Sciences 57, 1212–1220.

Terzaghi, K., 1943. Theoretical Soil Mechanics. John Wiley & Sons, Inc., Hoboken, NJ, USA.

Timothy, B., 1980. Post-test evaluation of nts multiple fracture/mineback experiments. Morgantown, WV.

Vesic, A.S., 1972. Expansion of cavities in infinite soil mass. Journal of Soil Mechanics and Foundations Division 98, 265–290.

Walters, D., Wang, J., Settari, a., 2012. A geomechanical methodology for determining maximum operating pressure in SAGD reservoirs. Society of Petroleum Engineers - SPE Heavy Oil Conference Canada 2012 2, 1065–1077.

Wang, Y., Dusseault, M., 1994. Stresses around a circular opening in an elastoplastic porous medium subjected to repeated hydraulic loading. International Journal of Rock Mechanics and Mining Sciences 31, 597–616.

Withers, N.J., Howie, J., Hughes, J.M.O., Robertson, P.K., 1989. Performance and analysis of cone pressuremeter tests in sands. Geotechnique 39, 433–454.

Wood, D., Wroth, C., 1977. Some laboratory experiments related to the results of pressuremeter tests. Geotechnique 27, 181–201.

Wood, D.M., 1990. Soil Behaviour and Critical State Soil Mechanics. Cambridge University Press, Cambridge, UK.

Wroth, C.P., 1984. The interpretation of in situ soil tests. Géotechnique 34, 449–489.

Wroth, P., 1980. Cambridge in-situ probe, in: Symposium on Site Exploration in Soft Ground Using In Situ Techniques. Alexandria, VA, pp. 97–135.

Yeoh, O., 1993. Some forms of the strain energy function for rubber. Rubber Chemistry and technology 66, 754–771.

Yu, H., 1998. CASM: A unified state parameter model for clay and sand. International Journal for Numerical and Analytical Methods in Geomechanics 22, 621–653.

Zhou, H., Liu, H., Kong, G., Huang, X., 2014. Analytical solution of undrained cylindrical cavity expansion in saturated soil under anisotropic initial stress. Computers and Geotechnics 55, 232–239.

Zoback, M., 2010. Reservoir geomechanics. Cambridge University Press, Cambridge, UK.

Zytynski, M., Randolph, M., 1978. On modelling the unloading-reloading behaviour of soils. International Journal for Numerical and Analytical Methods in Geomechanics 37, 87–93.

Appendix

The Python script for running parametric study and checking target results over FEM code Abaqus

```
import random

# Create the study
pars=('sigmaH','sigmah','sigmaZ','initialY','permeability','M','nu')
ce = ParStudy(par=pars,name='SensitiveStudy')

# Define the parameters
ce.define(DISCRETE, par=pars)

# Sample the parameters
# Randomly select the slope of Critical state line ranging from 0.8~1.2
ce.sample(VALUES, par='M', values=(random.sample([x*0.1 for x in range(8,12)],
3)))
# The horizontal stress anisotropy of interest is 1.5
ce.sample(VALUES, par='sigmaH', values=(5.1))
ce.sample(VALUES, par='sigmah', values=(3.4))
# Randomly select the initial vertical stress ranging from 1.7~5.1
ce.sample(VALUES, par='sigmaZ', values=(random.sample([x*0.1 for x in
range(17,51)], 3)))
ce.sample(VALUES, par='initialY', values=(15))
ce.sample(VALUES, par='permeability', values=(1e-8))
# Randomly select the Poisson's ratio ranging from 0.1~0.4
ce.sample(VALUES, par='nu', values=(random.sample([x*0.1 for x in range(1,4)],
3)))

# Combine the samples into design points
ce.combine(MESH, name='7Parameters')

# Generate analysis job data
ce.generate(template='Anisotropic_Cavity_Expansion')

# Execute all analysis jobs sequentially
ce.execute(ALL)

# Study output at end of step 1
ce.output(step=4,file=ODB)
```

```
# Gather the history results for the excess pore pressure and expansion pressure
ce.gather(results='pptop', variable='POR',
node=4,request=HISTORY,instance="Part-1-1")
ce.gather(results='s1minside', variable='S11', element=40,request=HISTORY,
instance="Part-2-1", node=63)

# Report the gathered results to an output file
ce.report(FILE, results=('pptop','s1minside'), file='ce_study_trial.ODB')

from odbAccess import *
# Access the Odb of the sampled studies in a group of 27 (each of 3 variables
have 3 d
for n in range(1,28):
        odb=openOdb(path='Anisotropic_Cavity_Expansion_SensitiveStudy_7Par
ameters_c'+str(n)+'.odb')
        # The expansion step in the simulation
        step1 = odb.steps['Loading']
        numFrames=len(step1.frames)
        # Defines nodes = node at top + node inside of membrane
        node1 = odb.rootAssembly.instances['PART-1-1'].nodeSets['Node at Top']
        node2 = odb.rootAssembly.instances['PART-2-1'].nodeSets['Node Inside']
        # Initialize a variable
        diff_por = 0.
        pre_por = 0.
        diff_expp = 0.
        pre_expp = 0.
        # Loop the frames since the expansion starts
        for i in range(40,numFrames):
        # Sets por = all pore pressure in model (POR) and expansion pressure =
(Stress)
                frame = step1.frames[i]
                por = frame.fieldOutputs['POR']
                expp = frame.fieldOutputs['S']
        # Sets por_at_nodes = por in nodes in set 'Node at Side' and
expp_at_nodes = 'MEMBRANE_SIDEX'
                por_at_nodes = por.getSubset(region=node1)
                expp_at_nodes = expp.getSubset(region=node2,
position=ELEMENT_NODAL)
                # Loops over all nodes in set, find the differentiation value of pore
pressure over expansion pressure
                for porVal in por_at_nodes.values:
                        diff_por = abs(porVal.data-pre_por)
                        crit_por=pre_por
                        pre_por = porVal.data
```

```
                    for stressVal in expp_at_nodes.values:
                        diff_expp = abs(stressVal.data[0]-pre_expp)
                        crit_expp=pre_expp
                        pre_expp=stressVal.data[0]
                    #print pre_por, pre_expp
        # Judge if the pore pressure generation rate exceeds the critical value, say
0.3
            if diff_por/diff_expp>0.3:
                    break
        # Creates a text file called 'outputs.dat' and writes responses of interest
        outputFile = open('outputs.dat','a')
        outputFile.write('The Excess Pore Pressure and Expansion Pressure when
Top Element Yields\n')
        outputFile.write(str(n)+'\t+''%10.4E\t'%(crit_por))
        outputFile.write('%10.4E\n'%(crit_expp))
        outputFile.close()
        odb.close()
```